Version May 8, 2014; substantially updated August 11, 2014
Preprint typeset using LaTeX style emulateapj v. 08/22/09

arXiv:1404.5968v6 [astro-ph.EP] 3 Jun 2015

DISINTEGRATION OF COMET C/2012 S1 (ISON) SHORTLY BEFORE PERIHELION: EVIDENCE FROM INDEPENDENT DATA SETS

Zdenek Sekanina[1] and Rainer Kracht[2]
[1]Jet Propulsion Laboratory, California Institute of Technology, 4800 Oak Grove Drive, Pasadena, CA 91109, U.S.A.
[2]Ostlandring 53, D-25335 Elmshorn, Schleswig-Holstein, Germany

Version May 8, 2014; substantially updated August 11, 2014

ABSTRACT

As an Oort Cloud object with a record small perihelion distance of 2.7 $R_\odot$ and discovered more than a year before its encounter with the Sun, comet C/2012 S1 is a subject of considerable scientific interest. Its activity along the orbit's inbound leg evolved through a series of cycles. Two remarkable events preserved in SOHO's and/or STEREO's near-perihelion images of its tail were an early massive production of gravel at heliocentric distances of up to ∼100 AU(!), evidently by the annealing of amorphous water ice on and near the nucleus' surface; and, about a week before perihelion, a rapid series of powerful explosions, from the comet's interior, of water vapor with dust at extremely high rates, causing precipitous fragmentation of the nucleus, shattering it into a vast number of sublimating boulders, and ending up, a few days later, with a major, sudden drop in gas emission. The disintegration of the comet was completed by about 3.5 hours before perihelion, at a heliocentric distance of 5.2 $R_\odot$, when C/2012 S1 ceased to exist. The orbital motion in this period of time was subjected to progressively increasing outgassing-driven perturbations. A comprehensive orbital analysis results in successfully fitting the comet's observed motion from 2011 to ∼7 hours before perihelion.

Subject headings: comets: general — comets: individual (C/1959 Y1, C/1962 C1, C/1999 S4, C/2003 A2, C/2011 W3, C/2012 S1) — methods: data analysis

1. INTRODUCTION

There are several reasons for an unusually intense scientific interest in comet C/2012 S1. Perhaps the most compelling one is its record small perihelion distance, merely 2.7 solar radii (1 solar radius = 1 $R_\odot$ = 0.0046548 AU), among known dynamically new comets, i.e., those arriving from the Oort Cloud. This perihelion distance beats the previous record, held by comet C/1962 C1 (Seki-Lines) by more than 4 $R_\odot$. Also beneficial are the early discovery of C/2012 S1 by Nevski & Novichonok (2012) and subsequent detections of pre-discovery images of the comet when it was as far as 9.4 AU from the Sun. The early discovery allowed a comprehensive monitoring of the comet's activity on its way to perihelion.

Anticipated with particular interest was the comet's behavior near perihelion and chances of its survival. An optimistic side of the controversy was argued e.g. by Knight & Welsh (2013), while the most skeptical view was Ferrín's (2013, 2014), who nearly two months before perihelion predicted the comet's impending demise. Much effort in the present investigation is expended to examine extensive evidence on the comet's physical state as a function of time, especially in the last weeks before perihelion when the brightness, the coma and tail morphology, and the orbital motion were subject to rapid and profound changes.

2. LIGHT CURVE, WATER PRODUCTION, AND MASS LOSS OF THE NUCLEUS

The first of the examined data sets are the comet's observed light curve and a representative H_2O production-rate curve. The light curve is defined as variations in the total brightness expressed in magnitudes, normalized to a distance Δ of 1 AU from the observer (the Earth for ground-based observations, a spacecraft for spaceborne observations) by employing the usual correction term $5 \log \Delta$ and to a zero phase angle (backscatter) by applying a standard correction based on a modified Henyey-Greenstein phase law introduced by Marcus (2007). Both the brightness and H_2O production rate variations, the latter measuring a fraction of the comet's total mass loss, are plotted against time and heliocentric distance.

2.1. *The Light Curve*

Two types of brightness observations are employed in the following: those made by ground-based observers, up to 2013 November 22; and those measured in the comet's images from space, between 2013 November 20 and 30. The employed magnitudes by selected ground-based observers are referred to the visual spectral region, even though some of them were obtained using CCD detectors.[1] Each observer measures the brightness of a comet in his own photometric system; the heterogeneity introduced by combining data from the various observers is minimized by implementing corrections to convert the data to a standard photometric system. The details related to C/2012 S1 have been described in Sekanina (2013a); an estimated uncertainty of the normalized magnitudes is about ±0.3 magnitude.

Most spaceborne normalized brightness data presented here were derived by us from two overlapping sets of preperihelion apparent magnitudes: one from measure-

Electronic address: Zdenek.Sekanina@jpl.nasa.gov, R.Kracht@t-online.de

[1] Three primary sources of the brightness data have been, respectively, the web site of the *International Comet Quarterly* (ICQ), `http://www.icq.eps.harvard.edu/CometMags.html`; the reports by observers, `http://groups.yahoo.com/neo/groups/CometObs/info`; and selected sets of *total* magnitudes (marked T) from a synopsis of astrometric observations in the database maintained by the *Minor Planet Center*, `http://www.minorplanetcenter.net/db_search`.

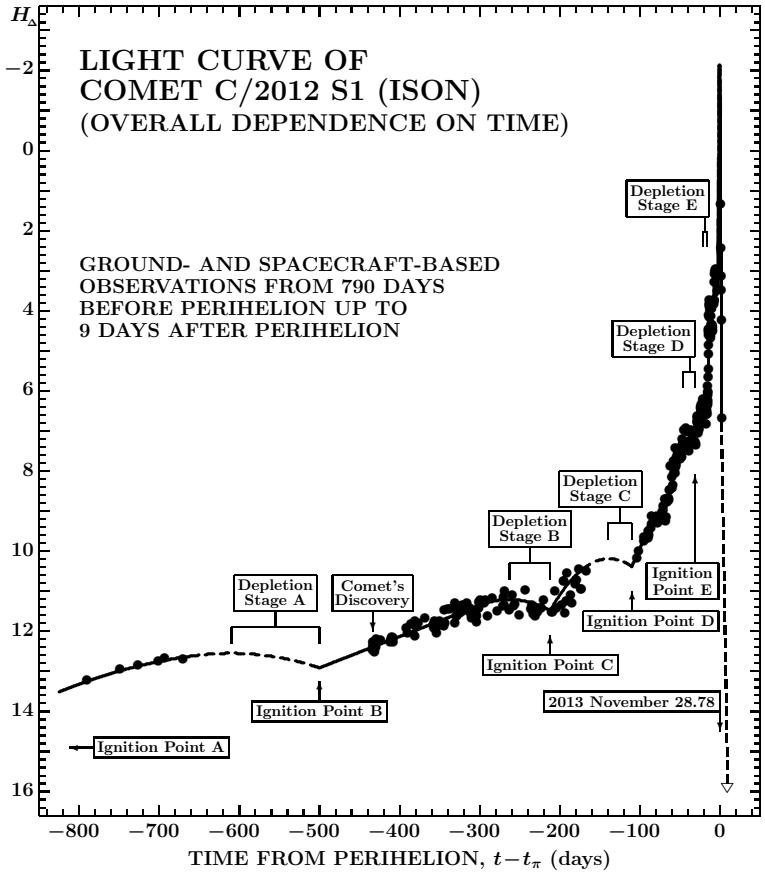

Figure 1. Overall light curve of comet C/2012 S1, based on about 300 selected ground-based observations (footnote 1) shown as solid circles and on spaceborne photometry: the HI1 imager on board STEREO A (Hui, footnote 2) and the C3 coronagraph on board SOHO (Knight & Battams 2014; Nakano 2013a; Ye, footnote 1). The results based on Hui's and Knight & Battams' preperihelion data are shown as thick lines near the peak, the results based on Nakano's and Ye's post-perihelion data as solid circles. A negative observation by Sako et al. (2013) from December 7 is depicted with a triangle. The magnitude H_Δ, plotted against time t reckoned from perihelion, t_π, is normalized to 1 AU from the observer and phase corrected using the Marcus (2007) law. The plotted data cover the period from 2011 September 30 (790 days before perihelion, the first pre-discovery observation) to 2013 December 7 (9 days after perihelion). Up to the time of the first major outburst, about two weeks before perihelion, the comet's light curve had been evolving in five cycles, A–E.

ments by M.-T. Hui in frames taken with the HI1 imager on board STEREO-A between Novemver 20.8 and 27.5 UT;[2] the other from measurements by Knight & Battams (2014) in clear-filter frames taken with the C3 coronagraph on board SOHO between November 27.1 and 28.6 UT. These sets were supplemented with several post-perihelion C3 apparent magnitudes from November 29.38–30.88 UT measured by Nakano (2013a) and from November 30.23 UT determined by Q. Ye, as listed on the ICQ web site (see footnote 1). We normalized all these apparent magnitudes to 1 AU from the spacecraft and phase corrected them using the Marcus (2007) law.[3]

The comet's overall light curve, which includes magnitudes from a number of pre-discovery images, taken between 2011 September 30 and 2012 January 28 at the Pan-STARRS Station on Haleakala, Hawaii (two rather discordant ones, on November 26 and December 9 averaged), and by the Mt. Lemmon Survey on Catalina near Tucson, Arizona (see the MPC Database in footnote 1), is plotted as a function of time, reckoned from perihelion, t_π, in Figure 1. In spite of two gaps, an 8-month long pre-discovery one in 2012 and a two-month long in 2013 due to the comet's conjunction with the Sun, the light curve appears to show that the comet's normalized brightness evolved in cycles, each of which started with an *ignition (activation) point*. The comet brightened throughout what we call an *expansion stage* of the cycle until a *stagnation point* was reached. At this time the comet's brightness began to stall and subsequently might drop a little in the course of the cycle's *depletion stage*. Eventually each cycle terminated at the next cycle's ignition point. The duration of an expansion stage is thus equal to the time difference between the stagnation and ignition points and the duration of a depletion stage equals the temporal distance from the stagnation point to the next ignition point. In their sum, the lengths of the expansion and depletion stages make up the duration of the cycle. Figure 1 shows a total of five cycles, A through E. The last two are, however, hard to see, as they fall on the steep portion of the light curve; they are clearly discernible in Figure 2, a plot of the normalized brightness against heliocentric distance r.

[2] A nearly complete HI1-A set of apparent magnitudes measured by Hui is posted at `http://groups.yahoo.com/neo/groups/cometsml/conversations/messages/22492`. Hui kindly provided us with a short extension of this set in a personal communication.

[3] Our phase corrections refer the normalized magnitudes to a zero phase angle, not to 90°, as does Marcus (2007).

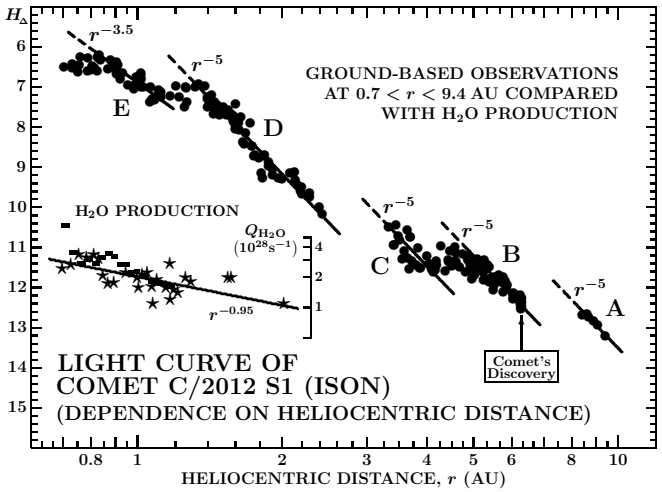

Figure 2. Magnitudes H_Δ of comet C/2012 S1, normalized to a unit distance from the observer and to a zero phase angle, plotted against heliocentric distance. The plot shows, as solid circles, selected ground-based brightness observations, made between the distances of 9.4 and 0.7 AU from the Sun. They are compared with data on the water production rate, Q_{H_2O}, represented by stars, with the daily averages, as presented by Combi et al. (2014), shown as thick bars. Also depicted are the five activity cycles A–E.

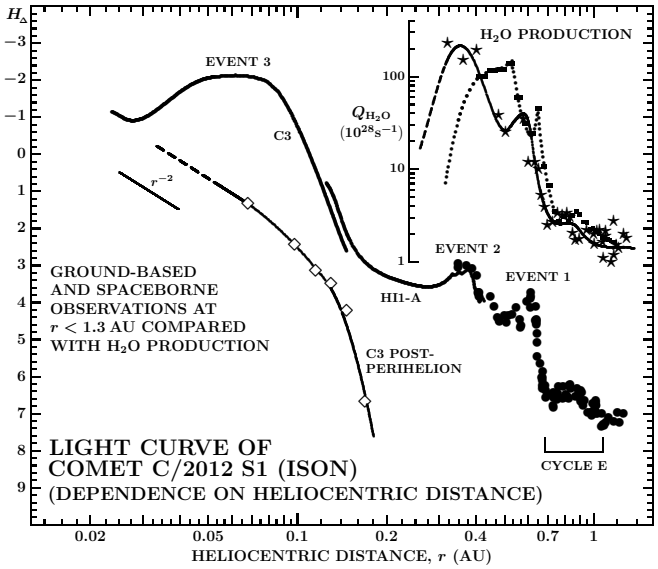

Figure 3. Ground-based and spaceborne normalized magnitudes H_Δ of comet C/2012 S1 plotted against heliocentric distance, from 1.3 AU to perihelion and shortly after perihelion. The ground-based data are represented by solid circles, the dense-data sets from preperihelion imaging with the SOHO's C3 coronagraph (Knight & Battams 2014) and with the STEREO-A's HI1 imager (Hui, footnote 2) are shown as thick labeled curves. Several C3-based post-perihelion data points by Nakano (2013a) and by Ye (footnote 1) are depicted with diamonds. The r^{-2} law of brightness variations is drawn for reference. The light curve is compared with the water production rate, Q_{H_2O}, plotted with the same symbols as in Figure 2. The dotted line is a fit to the daily averages of Q_{H_2O} by Combi et al. (2014).

A remarkable property of the expansion stages of the cycles A–D is nearly the same rate of the comet's brightening, as r^{-5}, with a lower rate only in the cycle E. The presence of depletion stages reduces the overall rate of brightening to about $r^{-2.5}$. Figure 3, which is, with an overlap, a continuation of Figure 2, covers a range from 1.3 AU to perihelion and shows that the cycle E terminated at the onset of a brief precursor to a major outburst. This event appears to be a sign that the long, rather orderly era of the comet's evolution had ended and that the object entered a stormy period, with rambunctious, unpredictable activity variations.

Since our interest in this study is being focused on the comet's behavior near the Sun, it is not our objective to examine in detail the nature and significance of the cycles of activity. We suggest, however, that their existence could be related to limited discrete reservoirs of ices — sources of activity on and just beneath the nucleus' surface. Accessed by the Sun's radiation in due time, each of these sources was activated (ignition point) and continued to be active over a limited period of time (expansion stage) until the bulk of the supply became essentially exhausted (stagnation point). The brightness then began to subside (depletion stage) until a new source of activity became available. The ability to reach the Sun's radiation and to sublimate profusely enough could be regulated both by the degree of volatility of icy species and by the depth of the reservoirs beneath the surface. In principle, the most volatile ices got released first, while water ice last. For example, carbon dioxide sublimates profusely, at rates greater than 10^{26} molecules per km^2 per second, at a subsolar point at 10 AU from the Sun and it could control the activity in the cycles A, B, and even C, as suggested by Meech et al. (2013b); carbon monoxide outgasses at similar rates still much farther from the Sun, more than 30 AU (e.g., Sekanina 1992). Mixtures of ices of uneven volatility are generally expected to drive the comet's activity cycles.

The duration of the activity cycles was getting progressively shorter as the comet was approaching perihelion, due apparently to the rapidly increasing rate of the Sun's heating of the comet's nucleus with decreasing heliocentric distance. The parameters of the cycles are summarized in Table 1. For each cycle, they include the times of the ignition and stagnation points, t_{ign} and t_{stg}, reckoned from perihelion t_π, the respective heliocentric distances, r_{ign} and r_{stg}, and the calendar dates, as well as the durations of the expansion and depletion stages. The time of the cycle A ignition point is of course unknown, as the comet's normalized brightness was already increasing in late September of 2011. The times of the cycle A stagnation point and the cycle B ignition point are known with large uncertainties because of the long gap between the last pre-discovery observation and the comet's discovery. As a result, only an estimate of a lower limit to the duration of the cycle A expansion stage and approximate durations of the cycle A depletion stage and the cycle B expansion stage are tabulated.

Figures 3 and 4, the latter representing a closeup of the near-perihelion light curve plotted against time and both covering practically the same time span, show that the stormy period of activity commenced in earnest almost exactly 16 days before perihelion, near November 13.0 UT. Opitom et al. (2013a) noticed a modest increase in the outgassing of minor species (such as CN and C_2) in early November, but this was accompanied by no robust increase in the dust production. A modest, about 50 percent, increase in the gas production was reported by Opitom et al. (2013b) during a 24 hour pe-

Table 1
ACTIVITY CYCLES OF COMET C/2012 S1: IGNITION AND STAGNATION POINTS, EXPANSION AND DEPLETION STAGES.

Cycle	Ignition point			Stagnation point			Duration of stage of	
	$t_{\rm ign}-t_\pi$ (days)	$r_{\rm ign}$ (AU)	calendar date (UT)	$t_{\rm stg}-t_\pi$ (days)	$r_{\rm stg}$ (AU)	calendar date (UT)	expansion (days)	depletion (days)
A	<-790	>9.4	<2011 Sept. 30	~-610	∼7.9	∼2012 Mar. 28	>180	∼110
B	~-500	∼6.9	∼2012 July 16	−263	4.50	2013 Mar. 10	∼237	51
C	−212	3.90	2013 Apr. 30	−140	2.95	2013 July 11	72	30
D	−110	2.51	2013 Aug. 10	−46	1.40	2013 Oct. 13	64	15
E	−31	1.07	2013 Oct. 28	−22	0.85	2013 Nov. 6	9	6

riod between November 11.4 and 12.4 UT, some 17 days before perihelion, with a comparable increase in the integrated brightness in the infrared, between 3 and 13 microns (Sitko et al. 2013), but again this growth of activity was not particularly significant. The cycle E was terminated in the next 24 hours, during which a brightening was vigorous enough to become apparent in both the light curve and water production rate. A sharp upswing began around November 14.0 UT, 14.8 days before perihelion, the onset of a massive outburst that is called *Event 1* in Figure 4. Boehnhardt et al. (2013) reported detection, on November 14.2 and again two days later, of arclet-like wings extending from the nucleus in opposite directions, whose appearance is known to have been associated with fragmentation of the nucleus in other comets in the past (Boehnhardt 2007); the wings were not detected on November 13.2 UT. Also coinciding with the onset of Event 1 was a major change in the comet's morphology, reported by Ye et al. (2013) from comparison of the comet's images taken by them on November 13.99 and 14.99 UT.

After reaching a peak brightness less than 2 days after the onset of Event 1, the comet faded a little, but another brightening was detected as early as November 19.4 UT, or 9.4 days before perihelion (Opitom et al. 2013c). This appears to have been a precursor to another major outburst, called *Event 2*, which, judging from the light curve based on Hui's data, started two days later, around November 21.2 UT, or 7.6 days before perihelion, exhibited multiple peaks centered on 6 days before perihelion, and then gradually subsided. This event proved very damaging to the integrity of the comet's nucleus, as discussed later. Yet, the brightness bottomed out once again 4.3 days before perihelion, followed by an out-of-control surge at an average rate of as much as 0.2 magnitude per hour prior to reaching a peak near magnitude −2 about 16 hours before perihelion (Knight & Battams 2014). This was *Event 3*. The rate of fading over the first two days after perihelion was almost equally steep.

Starting 8 days before perihelion, there is an excellent agreement between the light curves derived from ground-based observations and from Hui's HI1-A data. The HI1-A curve is, in turn, close to Knight & Battams' (2014) C3 data: in an overlapping interval of time seen in Figures 3 and 4 this C3 light curve runs in parallel less than 0.5 magnitude below the HI1-A curve.

In general, magnitudes from different instruments on board SOHO and STEREO are far less consistent. This topic has been addressed by Knight & Battams (2014)

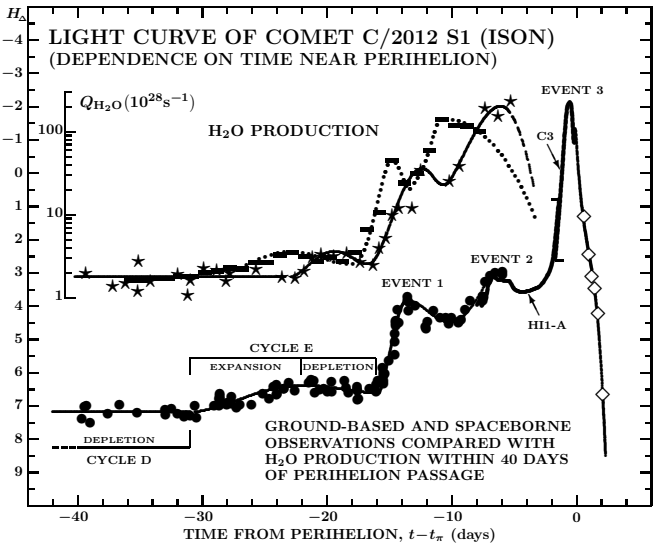

Figure 4. Light curve of comet C/2012 S1 between 40 days before perihelion and 2 days after perihelion and its comparison with the comet's water production rate variations. The short horizontal ticks show the overlap of the HI1-A and C3-based light curves. The other symbols are the same as those used in Figures 2 and 3.

in a recent paper, to which the reader is referred for details. After perihelion, all data show a steep and accelerating fading. In Figures 1 and 3–4 we illustrate the rate of this drop in brightness on the data by Nakano (2013a) and by Ye (footnote 1), which are ∼2.8 magnitudes brighter than Knight & Battams' (2014) post-perihelion data. The discrepancy appears to be an aperture effect: Nakano used 27 arcmin, while Knight & Battams only 7.5 arcmin, which indeed implies a difference of $5\log(27/7.5) = 2.8$ magnitudes, suggesting an essentially constant surface brightness over the measured area.

The normalized magnitude H_Δ in Figure 4 was next converted to an intrinsic brightness, independent of the heliocentric distance r, using a formula

$$\Im_0 = r^2 10^{2-0.4H_\Delta}. \quad (1)$$

If scattering of sunlight by dust particles dominated, the comet's brightness was proportional to their total effective cross-sectional area. For an assumed geometric albedo of 4 percent, the geometric cross-sectional area (for backscatter) was (in km^2)

$$X_{\rm dust} = 3.5\times10^5\Im_0. \quad (2)$$

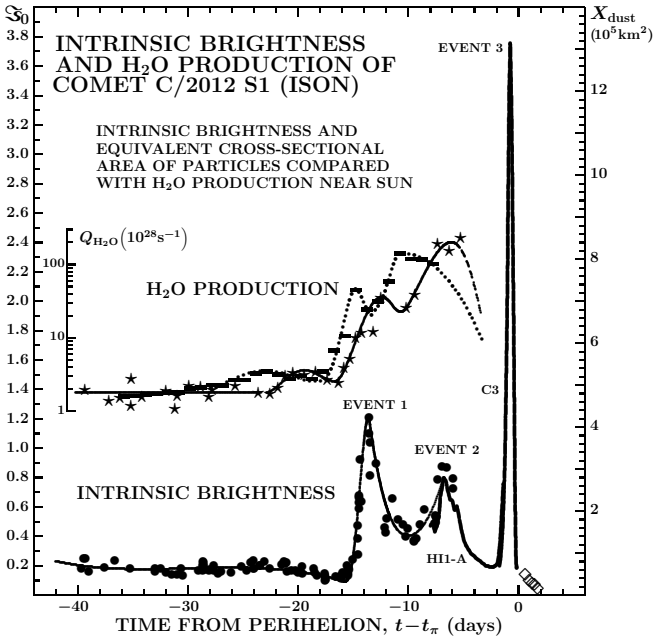
INTRINSIC BRIGHTNESS AND H2O PRODUCTION OF COMET C/2012 S1 (ISON)
INTRINSIC BRIGHTNESS AND EQUIVALENT CROSS-SECTIONAL AREA OF PARTICLES COMPARED WITH H2O PRODUCTION NEAR SUN
H2O PRODUCTION
INTRINSIC BRIGHTNESS
EVENT 1
EVENT 2
EVENT 3
C3
HI1-A
TIME FROM PERIHELION, t−tπ (days)

Figure 5. Intrinsic brightness of comet C/2012 S1 and an equivalent cross-sectional area of dust particles, $X_{\rm dust}$, in the coma plotted against time near perihelion and compared with the comet's water production rate variations. The symbols are the same as those used in Figures 3 and 4.

The difference between the geometric cross-sectional area and the cross-sectional area for scattering, which for submicron-sized particles depends on their optical properties, has been neglected.

The intrinsic brightness $\Im_0$ is displayed in Figure 5 as a function of time near perihelion. It had been remarkably constant prior to Event 1, averaging 0.2 unit, which is equivalent to an effective cross-sectional area for dust of 70,000 km^2. The two events are comparable in magnitude: Event 1 has a higher peak, Event 2 is broader. Their peaks remain at 14 and 6 days before perihelion, but the dip after Event 2 in the HI1-A data has moved to 2.4 days before perihelion (see Sec. 4.1). The peak intrinsic magnitude, reached ∼16 hours before perihelion, is equivalent to a total geometric cross-sectional area of 1.3×10^6 km^2, but this is undoubtedly a crude upper limit because of an expected strong contribution to $\Im_0$ from the doublet of atomic sodium near 5900 Å.

2.2. *Water Production Curve, Probable Early Fragmentation, and Correlations*

Starting with mid-September of 2013, positive detections of the comet's production of water were reported on many occasions, either from emissions of its photodissociation products, the hydroxyl in near-UV or radio wavelenghts and atomic hydrogen in Lyman-α, or directly in near-IR. The preliminary results have been published by Schleicher (2013a), Bodewits et al. (2013), Opitom et al. (2013a, 2013b, 2013c), Weaver et al. (2013), Keane et al. (2013), Mumma et al. (2013), Combi et al. (2013), Dello Russo et al. (2013), Remijan et al. (2013), Paganini et al. (2013), Crovisier et al. (2013), and Bonev et al. (2013). For the data based on direct H_2O feature measurements, the production rates are referred to the times of observation, while for the data derived from H or OH measurements, the rates are plotted at times approximately corrected for the disscociation lifetime of water (Huebner et al. 1992) but not for other effects. The most systematic set of water production rates has been published in a detailed paper by Combi et al. (2014), who studied the comet's hydrogen cloud in the full-sky Lyman-α images taken by the SWAN camera on board SOHO on 22 dates between October 24 and November 23. In addition to the production rates calculated from the individual images, Combi et al. also derived daily averages of the initial water production in the nucleus' proximity, using their time-resolved model. This information is particularly useful to investigations of temporal variations, including initiation of outbursts, in the comet's outgassing. Combi et al.'s data are plotted, together with the others, in Figures 2–5 and compared with the comet's light curve.

Temporal variations in the comet's water production were peculiar. Since the first detection, by Schleicher (2013a) 2.5 months before perihelion,[4] the average rate of increase over the next 7–8 weeks followed an $r^{-0.95}$ dependence (Figure 2) and can be described as sluggish at best. Because of the noise, we see no obvious signature of the cycle E's ignition point in the daily averages of the water production rate, but there is some evidence for the stagnation point around November 6 (Figures 4–5) and for the depletion stage in the days up to November 10. A minor surge began the next day, but by November 14 the production rate was a factor of 15 higher than five days earlier. This outburst coincided almost exactly with Event 1 in the light curve, as also noticed by Combi et al. (2014). After some decline, the water production rate jumped another factor of 3 on November 18, when it was nearly *two orders of magnitude* higher than three weeks earlier. This sharp peak coincided with the very beginning of Event 2 in the light curve. Between November 18 and the end of the SWAN data, the production rate's daily averages show a gradual, possibly accelerating, drop. No production of water was detected by Curdt et al. (2014) 0.7 hour before perihelion and by Combi et al. (2013, 2014) 5 days after perihelion.

M. Drahus reported in two web communications that monitoring the HCN emission at the IRAM observatory in Spain on November 21–25 indicated a dramatic *production drop* by a factor of at least 20.[5] Because observations show only small variations in the comet's HCN/H_2O production rate ratio (Coulson et al. 2013, Meech et al. 2013a, Paganini et al. 2013, Biver et al. 2013, Agúmdez et al. 2014), the sharp drop in the production of HCN was likely to accompany a similarly sharp drop in the water production during the 5-day period.

It turns out that, just like H_2O, a peak production of HCN, a parent molecule, coincided with Event 1, while its next peak was lagging the peak of the daily averages of water production, related to Event 2, by some 2–3 days, according to the preliminary findings (see the plot in the IRAM web news article; footnote 5). Only a weak HCN signal was detected with the IRAM dish about 1 day before perihelion.

[4] A water production rate of 3×10^{26} molecules s^{-1} reported by Schleicher (2013b) for 2013 March 5 was inferred from a CN production rate of 1.3×10^{24} molecules s^{-1}.

[5] These reports are at `http://groups.yahoo.com/neo/groups/comets-ml/conversations/messages/22461` & `22470`; and on IRAM site: `http://www.iram-institute.org/EN/news/2013/83.html`.

Short-term violent upturns in the production of water that began two weeks before perihelion suggest that the comet became prone to fragmentation, which appears to be the only avenue for activating new, sizable sources of water ice — deep in the interior of the nucleus. In the November 14 update to the first author's "on-the-go" investigation of the comet (Sekanina 2013a), he stated that it was "unclear whether the ... nature [of Event 1] is benign or cataclysmic."[6] In retrospect, it is likely that the physical mechanism responsible for Event 1 was the trigger that "catapulted" the comet toward its self-destruction by abruptly opening some of the nucleus' interior to the Sun's radiation. Thus, strictly, Event 1 was not cataclysmic over a period of a few days, but it was damaging in the sense that the nucleus was unable to recover afterwards. It is most likely that Event 1 was accompanying an early breakup of the nucleus (Sec. 4.2), an inference that is supported by Boehnhardt et al.'s (2013) report of arclet-like wings. As computer tests suggest, one could not expect any companion(s) to have been detected because by the time of the last ground-based imaging, on November 22.8 UT, or less than 9 days after the putative fragmentation event, typical secondary nuclei would have been separated less than 4 arcsec from the main mass and buried in the coma. Later on, when the comet was monitored by instruments on board SOHO and STEREO, the spacecraft imagers had inadequate spatial resolution. Judging from the skyrocketing water production rates, the initial breakup cascaded — as it usually does — into a set of fragmentation events that were fatal. If Drahus' preliminary report of a rapid decrease in the gas production by November 25 is (as expected) confirmed, then in the last three days before perihelion the comet's nucleus must have continued to orbit the Sun in a formation resembling a cluster of boulders and pebbles continuously crumbling into ever smaller pieces, eventually ending up with a *dust cloud*.

The reader will notice that this evolution led to a paradoxical situation in the sense that when many in the cometary community rejoiced at the comet finally brightening substantially, it was "on the ropes." Actually, all that is needed to make a comet reach apparent magnitude −2 at a distance of 0.075 AU from the Sun (the case of C/2012 S1 ∼16 hours before perihelion) is to achieve a cross-sectional area of dust of $\sim 10^6$ km^2, which is satisfied by an optically thin cloud of less than 10^{12} g of independent moderate-density particles 0.5 micron across!

2.3. *Dimensions and Mass Loss of the Nucleus*

Information on the production of water can be integrated to obtain a fairly reliable estimate for the mass losses suffered by the comet's nucleus over a period of at least two months. Since the nuclear mass — and therefore dimensions — must have been noticeably diminishing with time, a meaningful exercise in computing the comet's mass loss ought to be anchored to a starting point at which the nuclear size has been measured to a fairly high degree of accuracy. Li et al. (2013) observed the comet with a camera on board the Hubble Space Telescope on 2013 April 10, at a heliocentric distance of 4.15 AU, but were able only to determine that the nucleus was less than 4 km in diameter.

A much tighter limit on the nuclear size was reported by Delamere et al. (2013) from their detection of the comet with the Mars Reconnaissance Orbiter's High Resolution Imaging Science Experiment (HiRISE) around the time of the close encounter with Mars on 2013 October 1.7 UT. On the assumption that the signal in the brightest pixel was due exclusively to the comet's nucleus, it is found — at an adopted geometric albedo of 4 percent and with a constant correction of 0.04 magnitude per degree of phase angle — that the nuclear diameter was 1.0 ± 0.07 km,[7] which of course is still an upper limit on the true diameter. With a bulk density of 0.4 g cm^{-3}, the corresponding upper limit on the comet's mass at the time of the encounter with Mars is 2.1×10^{14} g.

It is now possible to assess the comet's mass loss of water between the close encounter with Mars on October 1 and the complete disintegration of the nucleus, which will be shown in Sec. 3 to occur a few hours before perihelion, on November 28. For the period October 24 through November 21, the water losses are given by Combi et al.'s (2014) daily averages of the production rate, equal to 1.81×10^{13} g. For the period October 1 through 24, the losses are computed by accepting the dependence of the production rate on heliocentric distance, $r^{-0.95}$, linked to Combi et al.'s daily average on October 24. This contribution equals merely 0.08×10^{13} g. Finally, for the period November 21 through 28, the losses of water are estimated by scaling up the HCN production rate from a preliminary curve in the IRAM web news item (footnote 5), linked to Combi et al.'s H_2O daily-average production rate on November 21. This contribution comes out to be 0.43×10^{13} g, with an estimated uncertainty of some $\pm 0.2 \times 10^{13}$ g. The total mass loss of water (which we equate with the total gas mass loss) over the entire 58-day period from the Mars encounter on amounts to 2.32×10^{13} g, with an error of about ±15 percent.

Next we estimate the comet's mass loss of dust in the same period of time. Using an instrumentation on board the Swift Space Telescope between October 7 and November 7, Bodewits et al. (2013) derived, from their measurements of the 3090 Å emission feature of OH, values of the water production rate in fair agreement with Combi et al.'s (2014) results, and from their measurements of the continuum, values of $Af\rho$, a dust-production rate proxy. By converting these values to dust production rates following A'Hearn et al. (1995), we find an average dust-to-water mass production rate ratio $\Re_0$ to amount to 1.5 ± 0.2. Assuming that it remained nearly constant throughout the 58 day period, the total mass loss from the comet, which equals the mass of the nucleus at the Mars encounter, amounts to 5.8×10^{13} g and, at an assumed bulk density of 0.4 g cm^{-3}, is equivalent to the nucleus' diameter of 0.65 km. with an estimated uncertainty of about ±0.05 km at a fixed bulk density and dust-to-water production rate ratio.

[6] Cometary outbursts, quite common phenomena, are entirely undiagnostic as to the future evolution of the afflicted objects: after experiencing an outburst, some comets behave as if nothing happened, some split, and only a tiny minority of them cataclysmically disintegrate.

[7] An albedo of 4 percent is the authors' assumption; Delamere et al. actually assumed an albedo of 3 percent and the upper limits on the diameter they derived from four observations were 1.25, 1.12, 1.05, and 1.12 km.

It therefore appears that the signal in the brightest pixel of the HiRISE detector was indeed contaminated significantly by dust. Considering that the geometric cross-sectional area of a sphere 1 km across is 0.785 km^2 and that Delamere et al.'s (2013) phase correction at the phase angles between 47° and 51°) was between 1.88 and 2.04 magnitudes, it follows that the total signal detected in the brightest pixel was equivalent to an observed cross-sectional area of 0.129 km^2 on the assumption of a geometric albedo of 0.04. Because a nucleus 0.65 km across accounts for a signal equivalent to an observed cross-sectional area of 0.055 km^2, an observed area of 0.074 km^2 is to be accounted for by the contaminating dust. Noting that the Marcus (2007) phase law for dust provides in this case a correction of 0.90 magnitude, we conclude that the geometric cross-sectional area of the dust is equal to 0.17 km^2. Using some simplifying but inconsequential assumptions, we next examine whether and under what conditions can a self-consistent model account for this cross-sectional area of dust in the brightest pixel of the HiRISE imager.

2.4. *Accounting for Contamination of the Nucleus' Signal by Dust Ejecta*

To estimate or constrain a contribution from dust that could contaminate the nucleus' signal detected by the HiRISE imager, we consider spherical dust particles with radii between a and $a + da$ released from the nucleus of C/2012 S1 between times t and $t+dt$, $\dot{N}(t)\,dt f(a)\,da$, where $\dot{N}(t)$ is the total number of particles ejected per unit time interval at time t and $f(a)\,da$ is a normalized particle-size distribution law. We require that particle radii be limited to a range of $a_{\min} \le a \le a_{\max}$ and that therefore

$$\int_{a_{\min}}^{a_{\max}} f(a)\,da = 1. \tag{3}$$

Reckoning t backward from the time of observation, the geometric cross-sectional area of ejected particles with radii between a and $a + da$ is

$$dX_{\rm dust} = \pi a^2 f(a)\,da \int_0^\infty \dot{N}(t)\,dt. \tag{4}$$

Delamere et al. (2013) state that at closest approach the HiRISE pixel scale at the comet was 13 km. Since the comet's dimensions were computed from the data at phase angles of 47°–51°, the pixel size was then about 17 km and its cross-sectional area was equivalent to that of a circle 9.6 km in radius. We call this radius $r_{\rm pix}$ and limit our investigation to a case in which (i) the nucleus is at the pixel's center, (ii) the dust emission is isotropic, and (iii) particles move radially away from the nucleus with a constant expansion velocity that depends on particle size. Thus, all particles of the same size and ejected at the same time populate an expanding spherical surface around the nucleus. In this approximation of true observational circumstances, the signal from the nucleus is contaminated by dust particles as long as they stay in the volume circumscribed by a cylindrical surface whose axis points to the observers' spacecraft and whose cross-sectional area equals that of the pixel. While all dust at distances $r_{\rm dust} < r_{\rm pix}$ from the nucleus contaminates its signal, only a fraction of dust at $r_{\rm dust} > r_{\rm pix}$ does so. These latter particles move in directions other than along a perpendicular to the line of sight and their fraction, decreasing with increasing $r_{\rm dust}$, is determined by the intersection of the expanding spherical surface with the cylindrical surface of radius $r_{\rm pix}$. In general, the cross-sectional area of particles with radii between a and $a + da$ that contaminate the nucleus' signal is

$$dX_{\rm cntm} = \pi a^2 f(a)\,da \int_0^\infty \dot{N}(t)\,\Phi(a,t)\,dt, \tag{5}$$

where the function $\Phi(a,t) \le 1$.

More specifically, the computation of the fraction of particles on the surface of a sphere of radius $r_{\rm dust} > r_{\rm pix}$ that contaminate the nucleus' signal involves a spherical cap circumscribed by the cylindrical surface. The fraction is given by the ratio of the cap's height from its base of radius $r_{\rm pix}$ to the sphere's radius $r_{\rm dust}$ and equals $1 - \sqrt{1 - (r_{\rm pix}/r_{\rm dust})^2}$. It is noted that the fraction of contaminating dust particles drops rapidly with increasing radius of the sphere. When $r_{\rm dust}$ is 1.5 times larger than $r_{\rm pix}$ the fraction is 0.255; when it is three times larger, the fraction drops to 0.057; and when $r_{\rm dust}$ is ten times as large as $r_{\rm pix}$, the fraction is down to 0.005. Since the expansion velocity of released particles is allowed to depend on their size, the spherical surface of the same radius $r_{\rm dust}$ is populated by dust that left the nucleus at different times; the larger the particles the earlier their release. For the particle-size dependence of the expansion velocity $\upsilon(a)$, which we assume to be independent of the distance from the nucleus, we adopt (e.g., McDonnell et al. 1987)

$$\upsilon(a) = \frac{\upsilon_0}{1+\chi\sqrt{a}}, \tag{6}$$

where υ_0 is the peak expansion velocity for $a \to 0$ and $\chi > 0$ determines the rate of velocity decrease with size and can be expressed in terms of a radius a_h of particles whose expansion velocity is $\frac{1}{2}\upsilon_0$,

$$\chi = a_h^{-\frac{1}{2}}. \tag{7}$$

The relation between time, that is, the age of a released particle at the time of observation, as the sphere's radius $r_{\rm dust}$ is simply

$$r_{\rm dust} = \upsilon(a)\cdot t = \frac{\upsilon_0 t}{1+\chi\sqrt{a}}. \tag{8}$$

Defining

$$t_{\rm pix} = \frac{r_{\rm pix}}{\upsilon_0}(1+\chi\sqrt{a}), \tag{9}$$

the total cross-sectional area of particles with radii between a and $a + da$ that contaminate the nucleus' signal is from Eq. (5)

$$dX_{\rm cntm} = \langle\dot{N}\rangle \pi a^2 f(a)\,da \times \left\{ t_{\rm pix} + \int_{t_{\rm pix}}^\infty \left[1 - \sqrt{1 - \left(\frac{t_{\rm pix}}{t}\right)^2} \right] dt \right\}, \tag{10}$$

where $\langle\dot{N}\rangle$ is an average value of $\dot{N}(t)$ over the ejection times of contaminating particles. This approximation can easily be justified, because we showed above that

Table 2
COMPUTED TOTAL GEOMETRICAL CROSS-SECTIONAL AREA OF DUST EJECTA CONTAMINATING NUCLEUS' SIGNAL.

Particle bulk density, ρ ($g\,cm^{-3}$)	Maximum particle radius, a_{max} (cm)	Total geometric cross-sectional area $X_{cntm}^{(\tau)}$ of contaminating dust (km^2)							
		Size distribution law $a^{-3.5}\,da$ with a_{min}				Size distribution law $a^{-3.75}\,da$ with a_{min}			
		0.05 μm	0.1 μm	0.2 μm	0.5 μm	0.05 μm	0.1 μm	0.2 μm	0.5 μm
0.4	175	0.100	0.074	0.055	0.039	2.396	1.455	0.890	0.472
0.8	87.5	0.074	0.055	0.042	0.030	1.455	0.890	0.550	0.297
1.2	58.3	0.062	0.047	0.036	0.026	1.090	0.671	0.417	0.228
1.6	43.8	0.055	0.042	0.032	0.024	0.890	0.550	0.344	0.190
3.5	20.0	0.041	0.031	0.025	0.019	0.517	0.324	0.207	0.118

the distances r_{dust}, from which large enough fractions of contributing particles come, are only tens of kilometers, which we will see are even for large particles equivalent to ejection times that precede the observation by only a day at the most. The integral in Eq. (10) equals

$$\int_{t_{pix}}^{\infty}\left[1-\sqrt{1-\left(\frac{t_{pix}}{t}\right)^2}\right]dt = t_{pix}\int_0^1 \frac{x(1-x)}{(1-x^2)^{\frac{3}{2}}}\,dx = t_{pix}\left(\frac{\pi}{2}-1\right), \tag{11}$$

so that

$$dX_{cntm} = \frac{1}{2}\langle\dot{N}\rangle\pi^2\frac{r_{pix}}{v_0}\,a^2 f(a)\,da, \tag{12}$$

where $\langle\dot{N}\rangle$ is an average number of dust particles released per unit time around October 1, the time of encounter.

Before integrating over all particle sizes from a_{min} to a_{max}, we express $\langle\dot{N}\rangle$ in terms of an equivalent mass dust production rate, $\dot{\mathcal{M}}_{dust}$, which we already computed from the water production rate and the dust-to-water mass production rate ratio in Sec. 2.2. Since for $\dot{\mathcal{M}}_{dust}$ one can write

$$\dot{\mathcal{M}}_{dust} = \frac{4}{3}\pi\rho\,\langle\dot{N}\rangle\int_{a_{min}}^{a_{max}} a^3 f(a)\,da, \tag{13}$$

a general formula for the total cross-sectional area X_{cntm} of dust particles that contaminate the signal of the nucleus in the HiRISE images is

$$X_{cntm} = \frac{3\pi}{8}\,\frac{r_{pix}}{v_0}\,\frac{\dot{\mathcal{M}}_{dust}}{\rho}\,\frac{\displaystyle\int_{a_{min}}^{a_{max}}(1+\chi\sqrt{a})\,a^2 f(a)\,da}{\displaystyle\int_{a_{min}}^{a_{max}} a^3 f(a)\,da}. \tag{14}$$

In this expression the independent entities are the particle-size distribution law $f(a)\,da$, the minimum particle size a_{min}, and the bulk density ρ of dust particles. Once these are prescribed, our exercise can proceed based on the already determined parametric values, $\dot{\mathcal{M}}_{dust} = 5.25\times10^5$ g s^{-1} and $r_{pix} = 9.6$ km. The three remaining parameters, a_{max}, v_0, and χ, are related to other physical quantities, as shown in part by Delsemme & Miller (1971) in their study of comet C/1959 Y1 and in part by Sekanina (1981) in his study of comet 109P, which for a particle expansion velocity employed an expression of the same type as is Eq. (6). The value of a_{max} depends on the water production rate and its efflux velocity, on the mass of the nucleus, and on the bulk density of dust particles; the value of v_0 is a function of the thermal velocity of water molecules and the dust-to-water mass production rate ratio; and the value of χ depends on these two and also on the water production rate, the size of the nucleus, and the bulk density of dust particles. To limit the number of variable parameters, we use only the upper limits for the nucleus' mass and size, and obtain the following expressions for the three parameters: $v_0 = 0.57$ km s^{-1}, $\chi = 11.4\sqrt{\rho}$ cm$^{-\frac{1}{2}}$, and $a_{max} = 70/\rho$ cm.

Four particle-size distribution laws are employed, of the type

$$f(a)\,da = n_0\left(\frac{a_{min}}{a}\right)^{\tau}da, \tag{15}$$

where n_0 is a normalizing constant [see Eq. (3)]. In conformity with the results of broad studies (e.g., Fulle 1999) of dust-particle size distributions in large number of comets, we choose for the power index τ the values of 3.0, 3.5, 3.75, and 4.0. After integrating Eq. (14), we obtain a total particle cross-sectional area $X_{cntm}^{(\tau)}$ for $\tau = 3.0$

$$X_{cntm}^{(3.0)} = \frac{3\pi}{4}\,\frac{r_{pix}}{v_0}\,\frac{\dot{\mathcal{M}}_{dust}}{\rho\,a_{min}}\,\frac{\varepsilon}{1+\varepsilon}\left[\chi\sqrt{a_{min}} - \frac{\varepsilon}{1-\varepsilon}\ln\varepsilon\right]; \tag{16}$$

for $\tau = 3.5$

$$X_{cntm}^{(3.5)} = \frac{3\pi}{8}\,\frac{r_{pix}}{v_0}\,\frac{\dot{\mathcal{M}}_{dust}}{\rho\,a_{min}}\,\varepsilon\left[1-\frac{\chi\sqrt{a_{min}}}{1-\varepsilon}\,\ln\varepsilon\right]; \tag{17}$$

for $\tau = 3.75$

$$X_{cntm}^{(3.75)} = \frac{\pi}{8}\,\frac{r_{pix}}{v_0}\,\frac{\dot{\mathcal{M}}_{dust}}{\rho\,a_{min}}\sqrt{\varepsilon}\,\left(1+\sqrt{\varepsilon}+\varepsilon+3\chi\sqrt{a_{min}}\right); \tag{18}$$

and for $\tau = 4.0$

$$X_{cntm}^{(4.0)} = -\frac{3\pi}{16}\,\frac{r_{pix}}{v_0}\,\frac{\dot{\mathcal{M}}_{dust}}{\rho\,a_{min}}\,\frac{1-\varepsilon}{\ln\varepsilon}\,(1+\varepsilon+2\chi\sqrt{a_{min}}); \tag{19}$$

where

$$\varepsilon = \sqrt{\frac{a_{min}}{a_{max}}} \ll 1. \tag{20}$$

For no plausible values of ρ and a_{min}, did the distribution laws with $\tau = 3$ and 4 satisfy the condition $X_{cntm} = 0.17$ km^2; the calculated area was always near 0.003 km^2 with the first law and always greater than 0.6 km^2 with the second law. Table 2 lists the results ob-

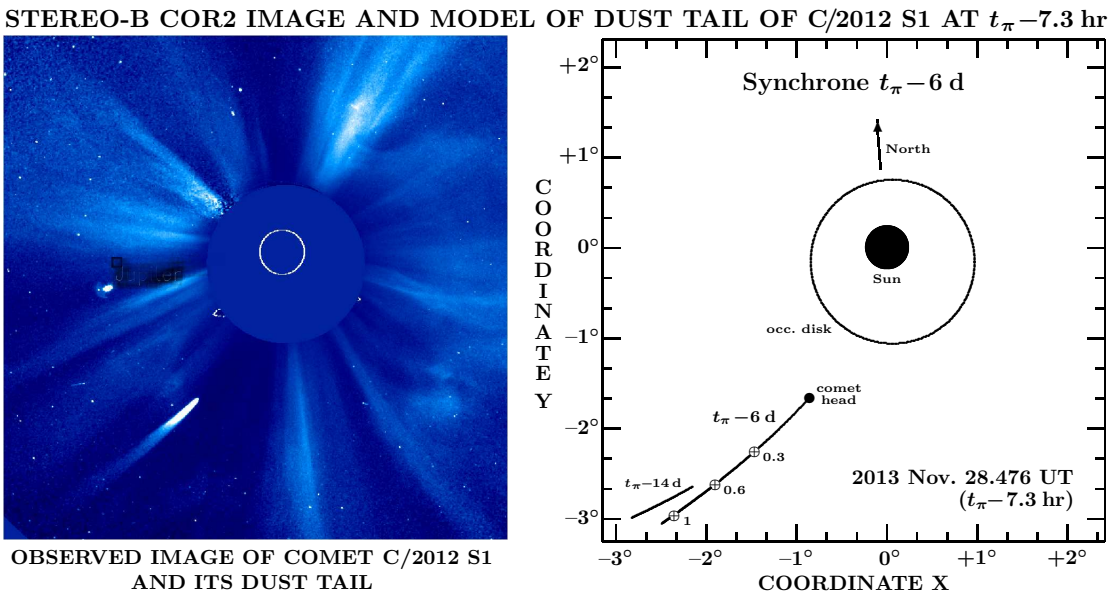

Figure 6. Appearance of comet C/2012 S1 and its dust tail in an image taken with the COR2 coronagraph on board the STEREO-B spacecraft on November 28.476 UT, 7.3 hours before perihelion and 8.8 $R_\odot$ from the Sun. The tail, to the southeast, is nearly straight and extends faintly almost to the edge of the frame. Its observed orientation and shape conform, in the panel to the right of the image, to a synchrone, a locus of projected positions of dust particles released from the comet's nucleus about 6 days before perihelion, t_π −6 d, thus correlating with Event 2. The synchrone is calibrated with values of β, a particle acceleration by solar radiation pressure, expressed in units of the Sun's gravitational acceleration. The brightest part of the tail corresponds to $\beta < 0.2$, typical for dust grains a few microns across and larger. The tail becomes extremely faint at $\beta > 0.6$, submicron-sized absorbing particles (such as metals or carbon-rich). Also shown in the panel is a section of a synchrone that describes the projected positions of dust ejecta from Event 1, 14 days before perihelion, t_π −14 d. The orientation of this synchrone is not in accord with the observed tail. The panel also offers information on the scale and orientation of the image. The bright spot to the northeast of the comet is Jupiter. (Image credit: NASA/SECCHI consortium.)

tained with the distribution laws $a^{-3.5}\,da$ and $a^{-3.75}\,da$, showing that all cross-sectional areas computed with the first law are smaller than 0.17 km^2 and, with one exception, all cross-sectional areas for the second law are greater than 0.17 km^2. Thus, the two laws — both in a range typical for size distributions of cometary dust — provide limits for the solutions that are consistent with the condition for the cross-sectional area of the dust contaminating the nucleus' signal in the brightest pixel of the HiRISE imager. Accordingly, we conclude that our result is self-consistent: from now on we adopt 0.65 km as a nominal diameter of C/2012 S1 at the Mars enounter time on October 1, 2013.

Given the small size of the nucleus, the estimated water production rate of $\sim 1.2 \times 10^{28}$ molecules s^{-1} at 1.64 AU from the Sun, at the time of encounter, shows a very impressive level of activity, to say the least. As addressed further in Sec. 4.2, the water production from the entire sunlit hemisphere of a nucleus 0.65 km in diameter should amount to $\sim 0.3 \times 10^{28}$ molecules s^{-1}, or only about one quarter of the observed rate. It is therefore suggested that most of the water vapor detected in the comet's atmosphere at distances well over 1 AU from the Sun was released from ejected icy-dust grains, whose total surface was more than sufficient to accomplish such a task. This scenario does not rule out the sluggish rate of increase in the water production with decreasing heliocentric distance during October and early November.

3. MORPHOLOGY OF THE COMET AND ITS TAIL ON SOHO AND STEREO IMAGES

Our primary objective in this section is close inspection of intrinsic changes in the comet's morphology as detected in the images taken with the coronagraphs on board SOHO (Brueckner et al. 1995) and STEREO-A and B (Howard et al. 2008) near perihelion. The results confirm that the correct answer to the question of what happened to the comet was available *shortly* after its perihelion passage (see Sekanina 2013b). The confusion caused by conflicting statements on the comet's survival or demise, reported in the media for days after perihelion and certainly not beneficial to the cometary community's reputation, could easily have been avoided.

Another objective in this section is to examine the manifestations, in the SOHO and STEREO images, of the history of the comet's activity and to correlate these results with those in Secs. 2.1–2.2. We are taking advantage of a powerful stereoscopic capability provided by the spatial configuration of the three spacecraft.

In the following, we model the morphology of the comet and its tail in eight particular images taken with the coronagraphs on board the three spacecraft over a period of time covering some 33 hours around perihelion. Additional images are then employed to investigate two more specific issues that have to do with the morphology of the head and sublimation of dust in the tail.

3.1. *Image Taken 7.3 Hours Before Perihelion*

To begin with, the left panel of Figure 6 presents the comet's preperihelion image taken with the COR2 coronagraph on board STEREO-B on November 28.476 UT. The comet, a little less than 2° from the Sun, displays a narrow, slightly curved tail that deviates about 15° from the antisolar direction. Both this orientation and a smooth appearance indicate the tail's dust nature. The right panel of the figure shows that the position angle of

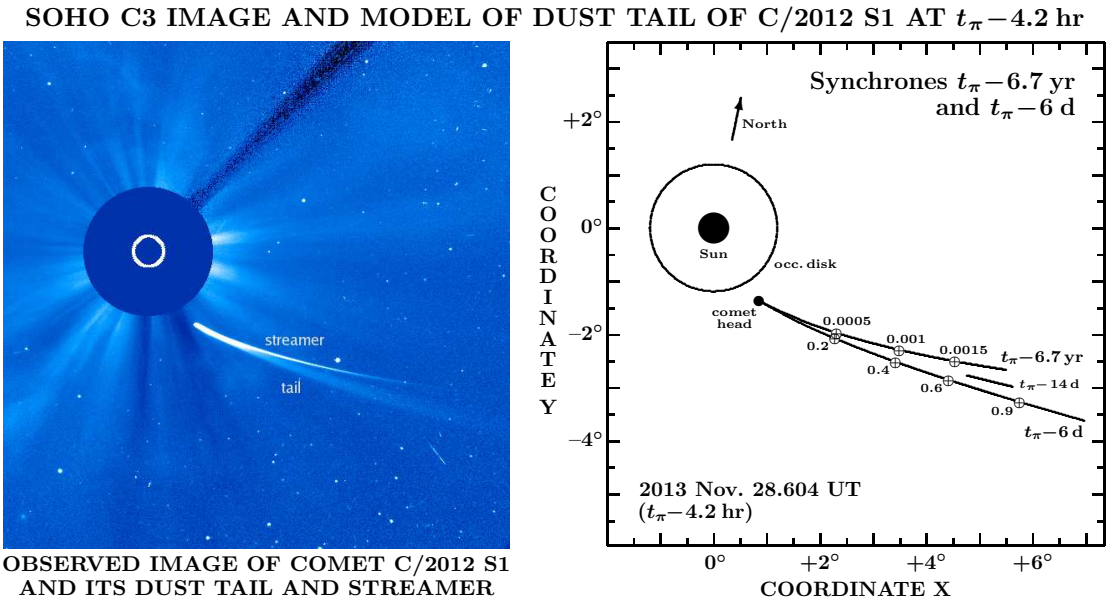

Figure 7. Appearance of comet C/2012 S1 and its dust tail and a streamer in an image taken with the C3 coronagraph on board the SOHO spacecraft on November 28.604 UT, 4.2 hours before perihelion and 5.9 $R_\odot$ from the Sun. The tail, the broader and less curved part of the bifurcated feature, extends to the edge of the frame, but becomes faint at distances greater than about 5° from the head. As seen from the right panel, the orientation and shape of this tail conforms to a synchrone for dust released from the comet's nucleus about 6 days before perihelion, thus again correlating with Event 2. As in Figure 6, the synchrone is calibrated with values of β, particle accelerations by the Sun's radiation pressure, expressed in units of the Sun's gravitational acceleration. The brightest part of the tail corresponds to $\beta < 0.2$, typical for dust particles several microns across and larger. Its faintest part is populated by submicron-sized absorbing particles with $\beta \gg 0.6$. Also shown in the panel is a section of a synchrone for dust ejecta from Event 1, which appear to contribute to the northern edge of the main tail. By contrast, the streamer is made up of sizable grains released from the comet at very large heliocentric distances; it is modeled by a synchrone for dust ejected from the comet at a distance of 20 AU from he Sun, 6.7 years before perihelion. For more description, see the caption to Figure 6. (Image credit: ESA/NASA/LASCO consortium.)

the tail's axis and its curvature are matched by a synchrone referring to the dust released around 6 days before perihelion, correlating apparently with Event 2 in Figures 4 and 5. The tail extends at least 1°.7 from the head, its brightest part populated — as shown by the model in the right panel of Figure 6 — by dust particles subjected to a radiation-pressure accelerations $\beta < 0.2$ the Sun's gravitational acceleration. Such particles are several microns across and larger. At a distance of 0°.5 from the head, the tail's width is estimated at ∼5 arcmin, which, interpreted as a particle-velocity effect, implies an ejection velocity of ∼0.25 km s^{-1}, a plausible value. On the other hand, the effect of the Event 2's temporal extent on the tail's width is found to barely exceed 1 arcmin for an estimated duration of ∼3 days, thus contributing little to the observed width. The phase angle was 59° at the head, but only 42° in the tail 1° away.

3.2. *Image Taken 4.2 Hours Before Perihelion*

The image in Figure 7, showing the tail to be bifurcated on November 28.604 UT, is a representative example of a long series of the comet's observations made with the SOHO's C3 coronagraph between at least November 27.4 and 28.8 UT that exhibit this feature. Testing of dust-emission models as well as a set of C3 images after November 28.8 UT demonstrate conclusively that these are in fact two independent and — as it turns out — very different tails that, in projection onto the plane of the sky, overlap near the nucleus, but deviate from one another farther away from it.

The longer, wider tail, making now an angle of almost 40° with the radius vector, closely fits the synchrone for dust released in the course of Event 2, centered on $t_\pi - 6$ days. The tail's apparent width, about 15 arcmin at 3° from the nucleus and only slowly increasing with distance, suggests particle-ejection velocities of up to 0.6 km s^{-1}, at an upper limit of plausible values. However, it is likely that the tail also contains a contribution from Event 1, merged with that from Event 2 into a single feature (Figure 7), which would account for about one half of the apparent width, and the required ejection velocities would accordingly be lower, not exceeding 0.3 km s^{-1}, and more in line with expectation.

The narrow, shorter tail is a different story. Referred to as a streamer in Figure 7, this feature's orientation and curvature practically trace the projected orbit behind the comet. The modeling of dust-particle motions shows that this is a typical property of the loci of sizable grains, released at near-zero velocities early, at very large heliocentric distances. The streamer could be called a developing *dust trail*, if it were not for this term having been introduced specifically for a persistent coarse-grained debris distributed along the orbits of periodic comets, both in front of and behind the parent body (e.g., Sykes et al. 1986, Sykes & Walker 1992, Reach et al. 2000).

Table 3 lists the position angles of the streamer and the properties of the grains that populate it at two distances from the comet's head, the first being the streamer's observed length in Figure 7. The table shows that the time of release cannot be determined from the streamer's position, only constrained to heliocentric distances larger than ∼5 AU, because the modeled loci of grains released at different times practically overlay one another. Columns 3 and 6 demonstrate that differences in the po-

MAJOR, WIDENING GAP BETWEEN THE STREAMER AND HEAD OF COMET C/2012 S1 IN IMAGES TAKEN WITH SOHO'S C2 CORONAGRAPH

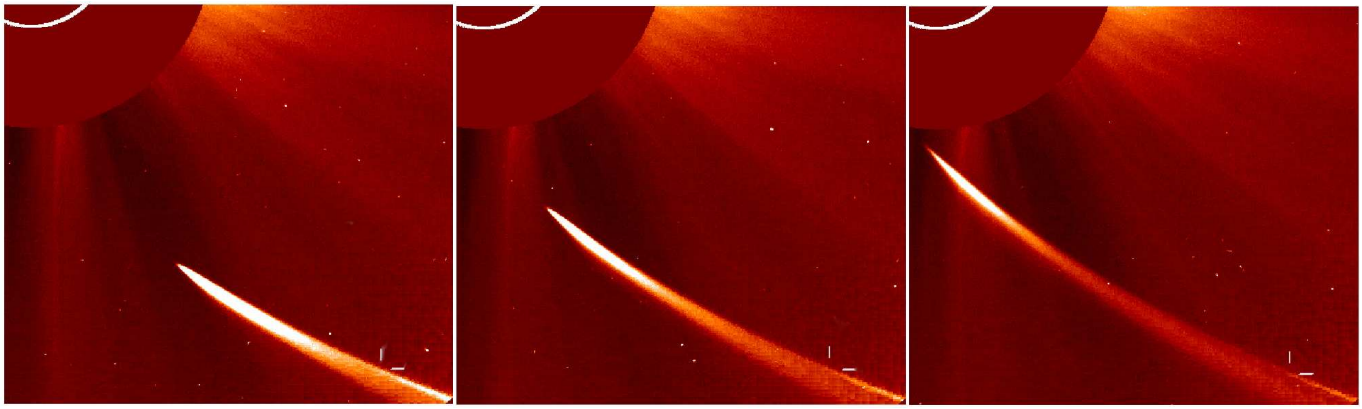

November 28.654 UT ($t_\pi - 3.0$ hr) | **November 28.692 UT ($t_\pi - 2.1$ hr)** | **November 28.725 UT ($t_\pi - 1.3$ hr)**

Figure 8. Examples of a major and widening gap, separating the disconnected dust streamer from the disintegrating head of comet C/2012 S1 in images taken with the C2 coronagraph on board SOHO shortly before perihelion. The streamer's forward tip, whose approximate location is marked by the short ticks in the lower right corner of each image, receded rapidly from the comet's head, but its position was nearly stationary relative to the Sun. The occulting disk with a contour of the Sun is in the upper left corner. The direction to the celestial north is essentially the same as in Figure 7. Each frame is about 95 arcmin wide and 85 arcmin high, which at the Sun's distance from the spacecraft translates to 4.0 by 3.6 million km. (Image credit: ESA/NASA/LASCO consortium.)

Table 3

COMPUTED POSITION ANGLES, RADIATION PRESSURE ACCELERATIONS, AND SIZES OF DUST GRAINS AT TWO POINTS OF THE STREAMER IN THE C3 IMAGE OF NOVEMBER 28.604 UT

Released[a] from comet		At 4°.5 from head[b]			At 1°.5 from head[b]		
$t_{\rm rls}$ (yr)	$r_{\rm rls}$ (AU)	Position angle	Acceleration β	Grain diam. (cm)	Position angle	Acceleration β	Grain diam. (cm)
−75.2	100	265°.83	0.000165	1.60	259°.33	0.000043	6.49
−26.6	50	265.82	0.000466	0.52	259.33	0.000120	2.22
−6.7	20	265.80	0.001836	0.11	259.32	0.000473	0.51
−2.4	10	265.73	0.005173	0.03	259.28	0.001334	0.16
−0.84	5	265.58	0.014534	0.01	259.19	0.003746	0.04

[a] Time of release, $t_{\rm rls}$, is reckoned from the forthcoming perihelion; $r_{\rm rls}$ is heliocentric distance at the time of release.

[b] Acceleration β by solar radiation pressure is expressed in units of the Sun's gravitational acceleration; grain diameter is computed from β assuming that the efficiency for radiation pressure of the grains is unity and their bulk density satisfies Eq. (21) .

sition angle of grains released between 5 and 100 AU from the Sun are always less than 0°.3, whereas the accuracy of orientation measurement is certainly not better than ±0°.5. However, since comets with perihelia near or beyond 5 AU — especially the dynamically new ones, from the Oort Cloud — are known to possess the same kind of a tail (e.g., Sekanina 1975; Meech et al. 2009), it is highly unlikely that the streamer of C/2012 S1 formed at a distance comparable to or less than 5 AU. Meech et al. observed an Oort-Cloud comet C/2003 A2 *already with a tail* as far as 11.5 AU from the Sun preperihelion. Given an extremely low solar radiation pressure at those heliocentric distances, very extended periods of time are needed to develop a long enough tail to detect. The distance of release of dust grains in the streamer is arbitrarily chosen to be 20 AU in Figure 7, and the issue is addressed in greater detail in Sec. 5.

Table 3 shows that the *earlier* the release of the grains that made up the streamer, the *larger* they were. Because of a broad span of grain sizes, we introduce a size dependent bulk density ρ (expressed in g cm^{-3}),

$$\rho(\delta) = 3.5 - 3.1\left[1+\left(\frac{10}{\delta}\right)^{0.6}\right]^{-1} \quad (0.4<\rho<3.5), \quad (21)$$

where δ is the grain's diameter in microns. The streamer thus contained mostly *millimeter-sized and larger* dust.

Given the very large heliocentric distances involved, one would expect that the grains in the streamer were initially rich in ices, including water ice. However, the streamer's survival to heliocentric distances of less than 0.1 AU rules out the presence of *pure or nearly pure* icy grains, which would have sublimated away long ago.

Now why the streamer is not detected in the image in Figure 6? At 1°.5 from the nucleus its position angle should be 116°, 7° to the north of the synchrone $t_\pi - 14$ d, clearly separated from the tail. The only explanation for its absence that we can think of is an insufficient exposure time given the relatively narrow, red-sensitive window of the COR2 coronagraph. It should be pointed out that the comet soon began to saturate the detector of the C3 coronagraph but not of the COR2-B coronagraph.

A remarkable phenomenon was a major gap, widening with time, that separated the streamer from the comet's head. The disconnected streamer shows up in all images taken with the C2 coronagraph between November 28.65 and at least 29.11 UT, although only a short arc of it fits the instrument's field of view and it becomes very faint after 28.8 UT. Three examples are displayed in Figure 8, covering a period of less than 2 hours. The disconnection is also seen in the images taken with the C3 coronagraph between November 28.7 and at least 29.1 UT. The forward tip of the streamer remained nearly stationary relative to the Sun. The obvious interpretation is in terms of rather sudden, complete sublimation of grains in

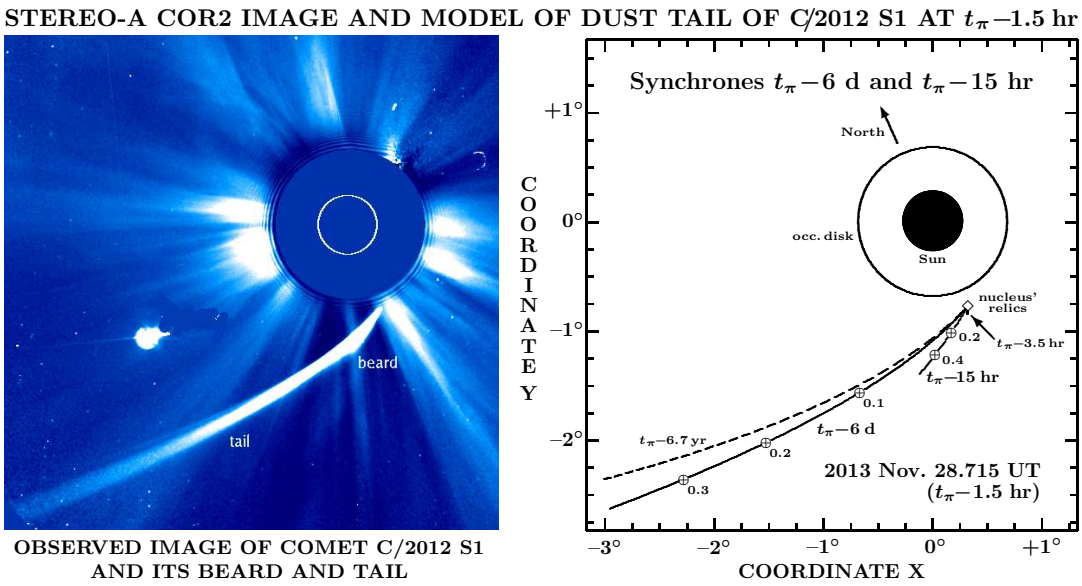

Figure 9. Appearance of comet C/2012 S1 and its dust tail and a "beard" in an image taken with the COR2 coronagraph on board the STEREO-A spacecraft on November 28.715 UT, 1.5 hours before perihelion and 3.4 $R_\odot$ from the Sun. A peculiarity of this image is the comet's displaying a "beard" that emanates to the southeast from what was left of the comet's nucleus and that is made up of microscopic dust released only about 13–14 or so hours earlier. The tail is once again matched best with a synchrone representing the Event 2 ejecta, which consist of dust particles several microns in diameter and larger. The nucleus' relics are depicted by a diamond. For more description, see the captions to Figures 6 and 7. The bright spot above the tail is Venus. (Image credit: NASA/SECCHI consortium.)

the streamer, once they approached the Sun to a certain critical distance. In projection this distance is estimated at about 1°.9 in Figure 8. The absence of the streamer in the image in Figure 6 cannot be explained by this effect. The fascinating subject of dust sublimation in the streamer is addressed at some length in Secs. 5.1–5.3.

The phase angle was 82° at the head, but 97° at 1°.5 from it in the tail and 113° in the streamer, which implies a moderate effect of forward scattering by the large grains (Marcus 2007).

3.3. *Image Taken 1.5 Hours Before Perihelion*

A peculiar feature immediately apparent in the image of the comet, taken on November 28.715 UT with the COR2 coronagraph on board STEREO-A and shown in Figure 9, is a bright "beard" extending a little more than 30 arcmin to the east-southeast from the head. This feature becomes apparent as early as November 28.6 UT only in STEREO-A images. Its sharp southern boundary is best matched by a synchrone for dust emitted from the nucleus some 15 hours before perihelion, at 15 $R_\odot$ from the Sun. In Figures 3–5, this time correlates with Event 3, the last upsurge of brightness before its eventual sharp decline. A peak solar radiation pressure $\beta_{\rm peak}$ on particles in the beard is about 0.4 the Sun's gravitational acceleration, suggesting that the particles are micron-sized and larger.

The comet's most prominent feature in this image is the long, slightly curving dust tail, as in the images in Figures 6 and 7 (Secs. 3.1–3.2). It again is matched best by a synchrone for mostly microscopic dust ($\beta < 0.4$) emitted during Event 2, about 6 days before perihelion. As in the STEREO-B image in Figure 6, there is no clear evidence of the streamer made up of old, massive grains. The phase angle decreased from 118° at the disintegrated nucleus and in the beard to 112° in the tail 2° away.

3.4. *Image Taken 3.3 Hours After Perihelion*

Taken on November 28.918 UT with the C2 coronagraph on board SOHO, this is the first post-perihelion image of the comet that we model. It shows, in Figure 10, an early stage of the most persistent feature observed along the outbound leg of the orbit — a fan-shaped cloud of dust. It emanates from an approximate site of the *nuclear condensation that is no longer apparent*. The eastern boundary of the fan is at this time — unlike later — much fainter than the western boundary, and at first sight the fan may appear to be narrower than it actually is. The direction of the eastern boundary provides a *key piece of information* on the comet — the time when the *emission of dust irrevocably ceased*. From the boundary's measurements on a number of images, this occurred *3.5 hours before perihelion* with an estimated uncertainty of ±0.3 hour. At that time, the *disintegration* of the nucleus was apparently *completed* and the *existence of C/2012 S1 was over* (Sec. 4.2). Dust particles that made up the eastern boundary of the fan were a few microns across and larger ($\beta < 0.3$).

The dust that made up the beard in Figure 9 is now closer to the cloud's sharp western boundary, which consists of dust ejecta from a wide range of times, including both outbursts — Event 1 and Event 2. The temporal resolution of this boundary is poor, permitting no more definite conclusions. Fortunately, a continuation of this boundary in Figure 10 is a tail to the southwest of the Sun. Its position allows us to establish that it was made up of dust mainly from Event 2, with a probable, unresolved contribution from Event 1. Slightly to the north of the westernmost part of the tail one can barely detect very faint remnants of the streamer, described in Sec. 3.2. The western boundary of the cloud contained, regardless of the ejecta's age, only fairly large particles, not smaller than approximately 10 microns in diameter ($\beta < 0.05$),

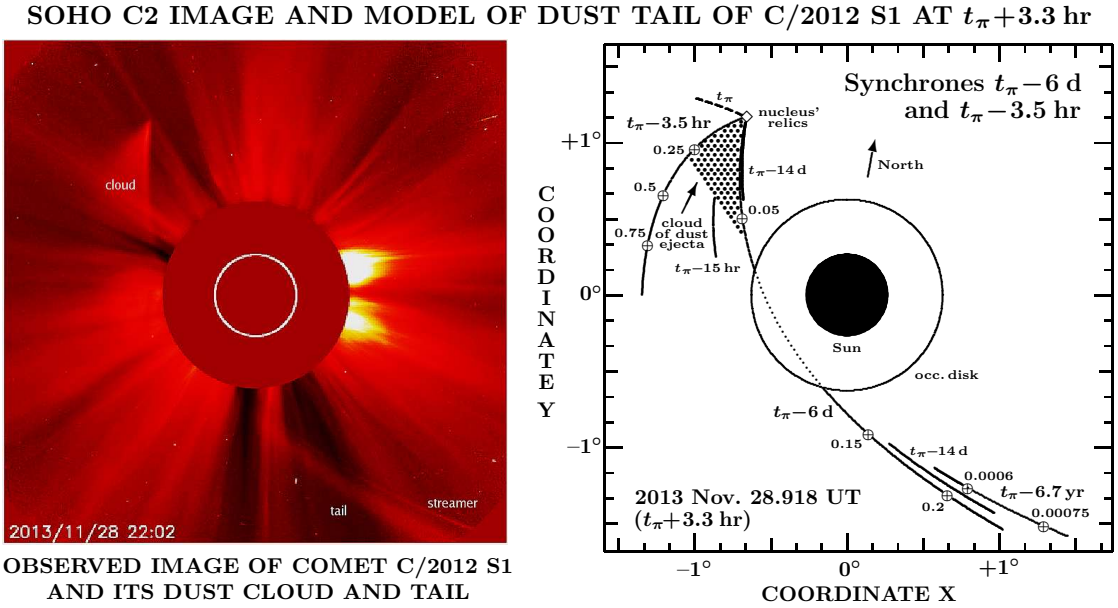

Figure 10. Appearance of comet C/2012 S1 and its dust cloud and tail in an image taken with the C2 coronagraph on board the SOHO spacecraft on November 28.918 UT, 3.3 hours after perihelion and 5.0 $R_\odot$ from the Sun. This image shows a dust cloud emanating from the site of the nuclear condensation that is no longer apparent. The dust cloud is a fan-shaped feature that contains all the dust ejected before, and surviving the passage through, perihelion. The eastern boundary of the cloud marks the emission of dust 3.5 hours before perihelion, at which point the activity ceased. The synchrone fitting the beard in Figure 9 (t_π −15 hr) is shown to be in the western part of the fan. A synchrone, to the east, for dust that would have been released at perihelion is seen to correspond to no feature in the image. On the other hand, a tail is shown made up of dust particles ejected mostly during Event 2, which did not pass their perihelion points as yet; and a barely detectable disconnected streamer, terminating — also before perihelion — at a smaller angular distance from the Sun than in the images in Figure 8. For other description, see the captions to Figures 6, 7, and 9. (Image credit: ESA/NASA/LASCO consortium.)

while the tail to the southwest of the Sun was composed mostly of particles a few microns across ($\beta \simeq 0.2$). The surviving segment of the disconnected streamer appears to terminate at a smaller angular distance from the Sun than in the images in Figure 8 (Secs. 5.1–5.3).

Much of the emission fan in Figure 10 contains dust ejected at times of major preperihelion activity. It is a common occurrence, especially among comets with small perihelion distances, that a "sequence" of significant preperihelion dust-production events shows up as a fan-shaped feature shortly after perihelion. By reading and interpreting its orientation, the comet's preperihelion dust-emission history can often be unequivocally established. With more information provided by the tail on the other side from the Sun, one finds out from Figure 10 that the dust that "counts" was all released over a period of ∼6 days terminating 3.5 hours before perihelion. Only an *earlier* preperihelion history of dust emission can at best be determined from images taken shortly before perihelion, as illustrated in Figure 9: the 6-day old ejecta make up the tail there as well, but the termination of activity 3.5 hours before perihelion (or 2 hours before that image was taken) presents itself as an unrecognizable blip near the head.

Also plotted in Figure 10 are (i) a synchrone confirming that no dust was ejected at perihelion, thus reiterating that by that time the comet was dead; and (ii) a synchrone fitting the streamer, seen with difficulties from the image's edge to no closer than ∼1°.5 from the Sun.

The phase angle at the site of the disintegrated nucleus in Figure 10 was 96°, while along both boundaries of the fan and in the tail it was in a general range from 50° to 90°, ruling out any forward-scattering effect.

3.5. *Image Taken 5.7 Hours After Perihelion*

In the image in Figure 11, taken with the COR2 coronagraph on board STEREO-A on November 29.017 UT, the fan-shaped cloud of preperihelion dust ejecta is located a little less than 2° to the north of the Sun, with the tail trailing to the southeast of it. The boundaries of the cloud are again matched well by the synchrones for dust released, respectively, 6 days (the southern boundary) and 3.5 hours (the northern boundary) before perihelion. The cloud is limited to only $\beta \lesssim 0.2$ or so along the latter boundary that marks the end of activity — thus suggesting that the smallest particles were a few microns across — but along its southern boundary it extends across much of the image and is transformed into a tail made up of micron- and submicron-sized particles ($\beta \lesssim 0.7$). The tail appears fairly narrow; as it is gradually fading with time, its edges may no longer be bright enough to show up in the image, as suggested by a much wider separation between the short segments of the synchrones for dust released 8 and 4 days before perihelion. The synchrone for dust released at perihelion lies once again entirely outside the ejecta's fan.

The phase angle at the site of the disintegrated nucleus was 61°. It increased to 67° at a distance of 0°.7 along the fan's nothern boundary and to 79°, 118°, and 110° at distances 1°.3, 2°.6, and 3°.5, respectively, along the southern boundary. Only a limited enhancement of brightness is seen in the tail's middle parts due to forward scattering. The phase angle eventually decreased to 94° at 6° from the disintegrated nucleus, near the edge of the field of view. Very close to the occulting disk there was much interference from solar features.

STEREO-A COR2 IMAGE AND MODEL OF DUST TAIL OF C/2012 S1 AT t_π+5.7 hr

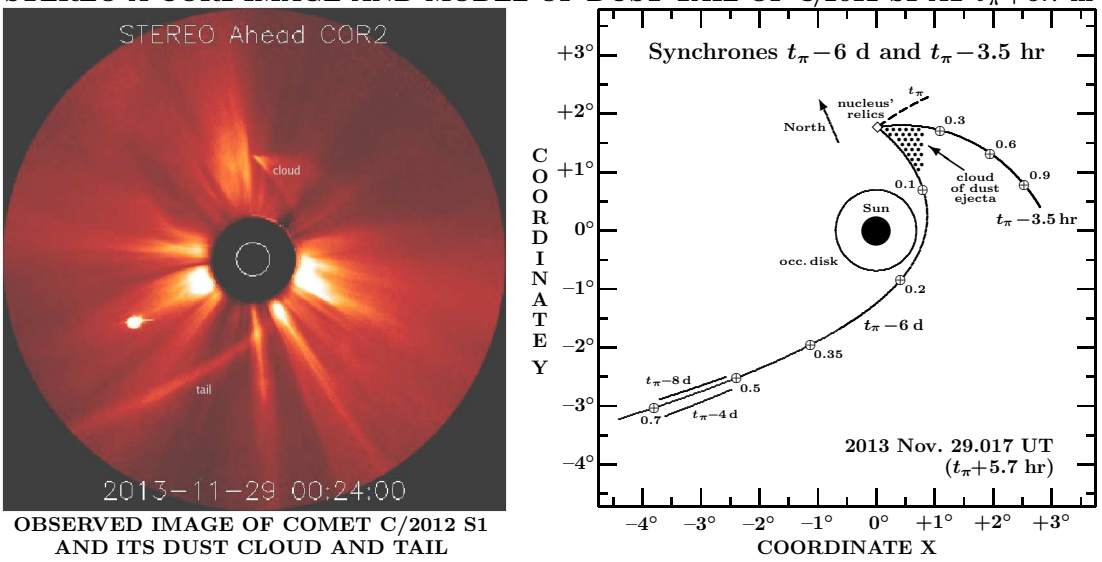

Figure 11. Appearance of comet C/2012 S1 and its dust cloud and tail in an image taken with the COR2 coronagraph on board the STEREO-A spacecraft on November 29.017 UT, 5.7 hours after perihelion and 7.3 $R_\odot$ from the Sun. The cloud of dust is again confined to a sector bounded by the synchrones for dust released, respectively, 6 days (southern boundary) and 3.5 hours (northern) before perihelion. To the southeast of the Sun, the southern boundary becomes a tail made up of dust ejected during Event 2. Segments of the synchrones for dust released 4 and 8 days before perihelion are plotted for comparison. While only particles several microns across and larger make up the northern boundary, the tail also contains submicron-sized grains. A synchrone for dust released at perihelion corresponds to no feature in the image. For more description, see the captions to Figures 6–7 and 9. (Image credit: NASA/SECCHI consortium.)

STEREO-B COR2 IMAGE AND MODEL OF DUST TAIL OF C/2012 S1 AT t_π+11 hr

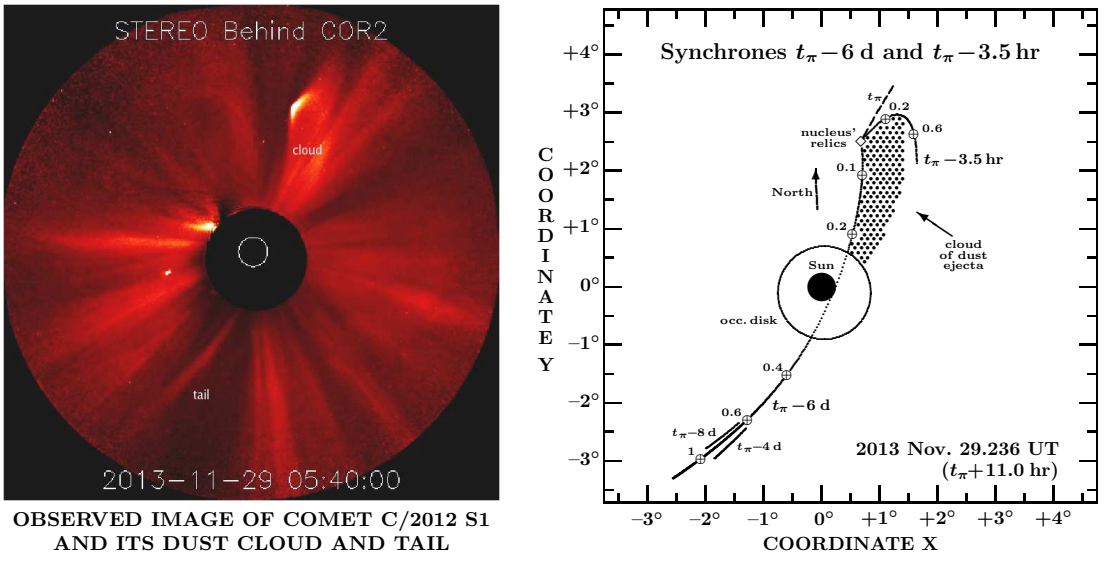

Figure 12. Appearance of comet C/2012 S1 and its dust cloud and tail in an image taken with the COR2 coronagraph on board the STEREO-B spacecraft on November 29.236 UT, 11.0 hours after perihelion and 11.9 $R_\odot$ from the Sun. The cloud of dust, now seen from a different perspective, makes up a very wide fan, whose brightness is enhanced by a significant forward-scattering effect, in contrast to the subdued tail. The fan consists again of dust ejecta from 6 days to 3.5 hours before perihelion, with no emission from times closer to perihelion. For more description, see the captions to Figures 6–7 and 9. (Image credit: NASA/SECCHI consortium.)

3.6. *Image Taken 11.0 Hours After Perihelion*

The image in Figure 12, obtained with the COR2 coronagraph on board STEREO-B, looks unusual in part because the spacecraft was only 13° above the comet's orbit plane at the time of observation, on November 29.236 UT. The dust cloud, which is in part superposed on some solar features, appears to be considerably brighter and to have much larger dimensions than in Figure 11, while the tail is now fainter. The two features are consistent with the scenario established from the previous images — they are products of the comet's activity between 6 days and 3.5 hours before perihelion, as shown in the right-hand side panel of Figure 12, but the apparent brightening is an effect of forward scattering of sunlight by dust particles in the cloud. While the phase angle reached 62° at the location of the disintegrated nucleus and mostly between 80° and 90° along the fan's northern boundary, it was steadily increasing along the southern boundary

SOHO C3 IMAGE AND MODEL OF DUST TAIL OF C/2012 S1 AT t_π+16.4 hr

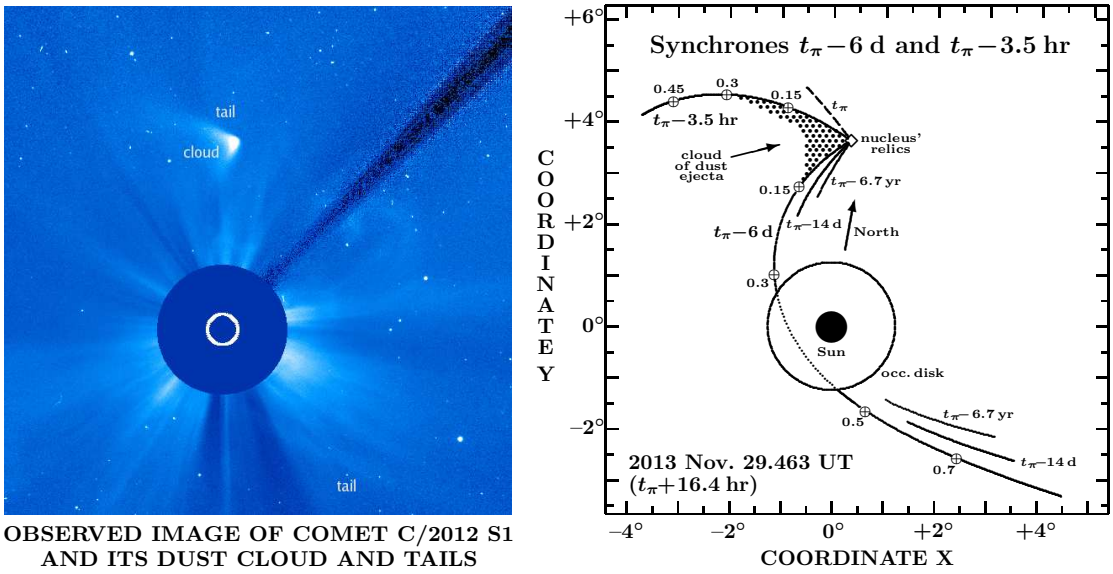

Figure 13. Appearance of comet C/2012 S1 and its dust cloud and tails in an image taken with the C3 coronagraph on board the SOHO spacecraft on November 29.463 UT, 16.4 hours after perihelion and 16.1 $R_\odot$ from the Sun. The northern branch of what now looks like a winged object, has become longer and brighter, looking like an independent tail. This is the branch that signals the end of the comet's activity 3.5 hr before perihelion. The fuzzy southern branch is no longer diagnostic of the age of the ejecta it contains, but the tail on the other side of the Sun is made up of the dust ejected in Event 2. The pseudo-condensation near the location of the disintegrated nucleus is due to effects of forward scattering. For more description, see the caption to Figures 6. (Image credit: ESA/NASA/LASCO consortium.)

to ∼120° close to the occulting disk. Inside the fan, the phase angles were even higher and often exceeded 140°. For example, for submicron-sized particles having $\beta \simeq 0.6$, located more than 1° to the south of the disintegrated nucleus, right in the middle of the bright blob in Figure 12, the phase angle was 144°, which implies a forward-scattering driven brightness enhancement by 2 magnitudes. The phase angle variations along the tail were, on the other hand, in a range from 40° to 90°. This example plainly shows that there is no need for a tempting but untenable hypothesis explaining this major brightening in terms of a surge of new, post-perihelion activity.

3.7. *Image Taken 16.4 Hours After Perihelion*

Forward scattering of sunlight by dust similarly explains the comet's apparent brightening in many images taken after perihelion with the C3 coronagraph on board SOHO. One of these, displayed in Figure 13, was obtained on November 29.463 UT. Comparison with Figure 10, exposed with the C2 coronagraph on board the same spacecraft suggests that there is now a pseudo-condensation at the site of the disintegrated nucleus, where there was none some 13 hours earlier. Even though different instruments were used, the change in the comet's appearance is rather startling. The phase angle at the location of the disintegrated nucleus was 96° in the C2 image in Figure 10, but it increased to 124° in the C3 image in Figure 13, a difference equivalent to more than 1 magnitude in a relative phase effect due to forward-scattering. In addition, the phase angle peaked in Figure 13 at the location of the pseudo-condensation, decreasing with increasing distance from it in what now looks like a winged object and reaching merely 116° just 1° from the pseudo-condensation along both wings.

There are other differences in the comet's appearance in Figure 13 compared to Figure 10. The northern branch, referring to the end of activity 3.5 hours before perihelion, has properties of an independent tail. It is now longer and more pronounced than the southern branch, which has become fuzzy, providing no longer a constraint on the age of the debris in it. A dust tail projecting on the other side of the Sun from the winged feature is, however, still visible, especially in the section made up of submicron-sized particles with $\beta \simeq 0.7$. The position of this tail shows that, once again, it is a product of Event 2 centered on 6 days before perihelion. The phase angles in the brightest parts of this tail in Figure 13 were in a range from about 90° to 100°.

3.8. *Image Taken 25.8 Hours After Perihelion*

The final image that is modeled was taken on November 29.854 UT, also with the C3 coronagraph. Presented in Figure 14, it resembles in many respects the image from Figure 13. However, the pseudo-condensation faded, while the tail to the northeast lengthened. The brightness of the cloud to the south of this tail also subsided. The other tail, to the south and southwest of the Sun, an area not shown in Figure 14, has disappeared. The phase angle at the site of the disintegrated nucleus still slightly increased, to 127°, helping to keep the pseudo-condensation alive. Along the northeastern tail, the phase angle, dropping a little, was equal to 119° at 1°.5 from the pseudo-condensation.

3.9. *Summary of Results from Modeled Images*

The eight modeled images of comet C/2012 S1 cover a period of about 33 hours. The three preperihelion images differ from one another in that they show diverse features, although all dusty as indicated by their large

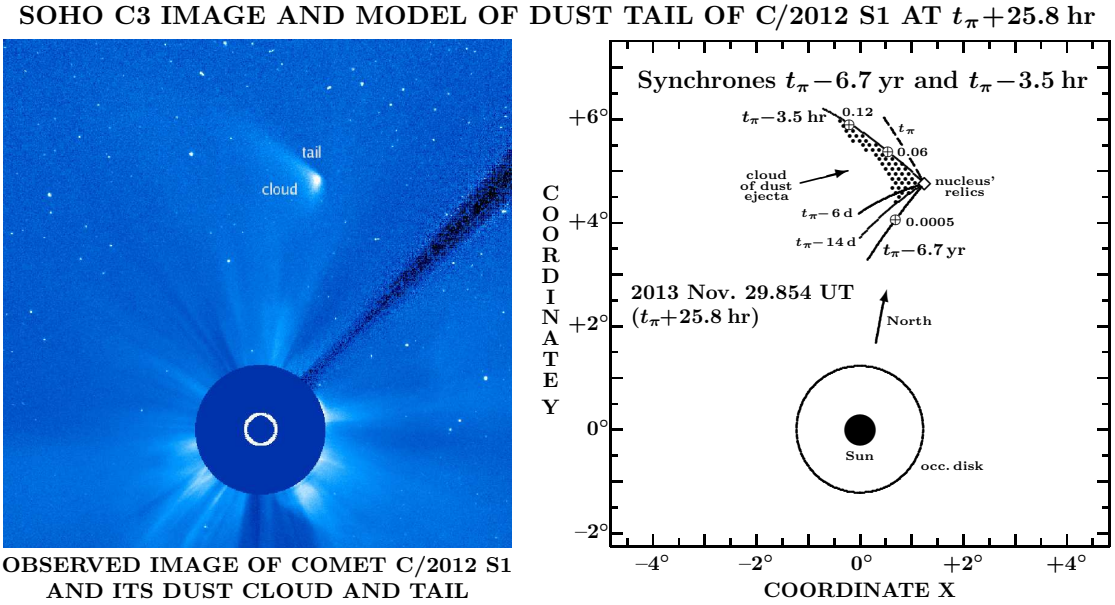

Figure 14. Appearance of comet C/2012 S1 and its dust cloud and tail in an image taken with the C3 coronagraph on board the SOHO spacecraft on November 29.854 UT, 25.8 hours after perihelion and 22.4 $R_\odot$ from the Sun. The pseudo-condensation is noticeably fainter than in the image in Figure 13. The northern branch now completely dominates the southern one and becomes the only tail (making ∼70° with the antisolar direction), because the old, preperihelion tail to the south of the Sun is no longer convincingly recognized. For other description, see the captions to Figures 9 and 13. (Image credit: ESA/NASA/LASCO consortium.)

deviations from the antisolar direction and a generally smooth appearance. The first image (Figure 6), taken with the COR2-B coronagraph 7.3 hours before perihelion when the comet was 8.8 $R_\odot$ from the Sun, displays only a narrow, slightly curved tail, a product of Event 2. Evidence for this outburst is repeatedly confirmed, by one feature or another, in six of the remaining seven images in Figures 7 and 9–14. Only in the last image a signature of this event is missing, apparently too obliterated due to dispersion in space.

The second image (Figure 7), taken with the SOHO's C3 coronagraph 4.2 hours before perihelion when the comet was 5.9 $R_\odot$ from the Sun, shows a bifurcated tail, a phenomenon caused by a partial overlap of two very different features. One is the dust tail from Event 2, probably with a contribution from Event 1, the other is a streamer that closely traces the projected orbit behind the comet. It is a product of activity at very large heliocentric distances and is disconnected from the head. The process of grain release may have proceeded over a long, rather indeterminate period of time. However, the age of the grains is more than ∼1 year. The comet was active at 9.4 AU from the Sun, the earliest images taken 26 months before perihelion. The streamer is not seen in the STEREO's COR2 images (both B and A), probably because of insufficient exposure times.

The third modeled image (Figure 9), taken with the COR2-A coronagraph 1.5 hours before perihelion when the head of the comet was only 3.4 $R_\odot$ from the Sun, displays — in addition to the usual tail — a prominent "beard," made up of dust released during Event 3, only a little more than 12 hours before observation.

The fourth modeled and the first post-perihelion image (Figure 10), taken with the C2 coronagraph 3.3 hours after closest approach when the comet was 5.0 $R_\odot$ from the Sun, shows two major morphological changes. One is a *total loss of the head with the nuclear condensation*, the other is a fan-shaped, sideways-pointing tail. The head's diappearance was recorded earlier in real time by the C2 coronagraph on board SOHO (Sec. 4.1). The leading boundary of the emission fan, oriented toward the southeast in this image, measured the *time of termination of the comet's dust production*. Determined independently from a number of images, this singular condition is found to have occurred *3.5 ± 0.3 hours before perihelion*; at that time *all activity ceased, never again to be resuscitated, the nucleus' disintegration was completed, and the existence of the comet as such was over*. This result refines an earlier preliminary determination (Sekanina 2013b) and is consistent with Curdt et al.'s (2014) conclusion, based on the scattered-light observations of the comet's dust tail in Lyman-α with the SUMER spectrometer on board SOHO merely 0.7 hour before perihelion. Their images suggest an outburst of dust about 8.5 hours before perihelion, followed by a sharp decline in the dust production over the next hours.

The source of much confusion in early media reports was the re-appearance of the comet's relics from behind the occulting disk of the C3 coronagraph (Figures 13–14). A bright pseudo-condensation was apparent in these images, but *no nuclear condensation*; the brightening was due to forward scattering of sunlight by microscopic dust in a relatively dense cloud, contrary to the comet's reappearance from behind the occulting disk in the C2 coronagraph (Figure 10), which preceded that in the C3 coronagraph. The reason for the discrepancy is this timing: in C2 the post-perihelion images covered a period from about 0.7 to 5 hours after perihelion, while in C3 the post-perihelion show did not start until about 3.5 hours after perihelion, with the pseudo-condensation steadily brightening up over another 3.5 hours as the heliocentric distance continued to increase. The phase angles

Table 4
Orbital Elements of Dust Particles Released from Comet C/2012 S1

Radiation pressure acceleration[a] β	Particle diameter[b] (mm/μm)	Orbital elements of released dust particles[c] as function of the time of release before perihelion											
		Perihelion distance ($R_\odot$)				Orbit eccentricity[d]				Perihelion time (hr)[e]			
		3.5 hr	6 d	14 d	6.7 yr	3.5 hr	6 d	14 d	6.7 yr	3.5 hr	6 d	14 d	6.7 yr
0.0001	26.9	2.68	2.68	2.68	2.68	1.0001	1.0000	1.0000	1.0000	0.00	0.00	+0.01	+1.18
0.0003	8.4	2.68	2.68	2.68	2.68	1.0003	1.0000	1.0000	1.0000	0.00	+0.01	+0.02	+3.55
0.001	2.2	2.68	2.68	2.68	2.68	1.0010	1.0001	1.0000	1.0000	0.00	+0.03	+0.07	+11.82
0.003	0.59	2.68	2.68	2.68	2.68	1.0031	1.0002	1.0001	1.0000	0.00	+0.10	+0.22	+35.51
0.01	0.12	2.69	2.70	2.70	...	1.0105	1.0007	1.0004	...	0.00	+0.34	+0.75	...
0.03	*24.9*	2.72	2.76	2.76	...	1.0323	1.0023	1.0013	...	−0.01	+1.03	+2.26	...
0.1	*5.1*	2.81	2.96	2.97	...	1.1199	1.0087	1.0049	...	−0.05	+3.55	+7.81	...
0.2	*2.2*	2.93	3.31	3.32	...	1.2820	1.0219	1.0123	...	−0.12	+7.51	+16.51	...
0.3	*1.4*	3.05	3.74	3.78	...	1.5036	1.0425	1.0240	...	−0.20	+11.96	+26.29	...
0.5	*0.78*	...	5.02	5.15	...	...	1.1330	1.0766	...	...	+22.81	+50.40	...
0.7	*0.54*	...	7.28	7.85	...	...	1.4503	1.2721	...	...	+36.87	+83.82	...
1	*0.37*	...	14.21	18.98	...	...	∞	∞	...	...	+57.70	+148.74	...

[a] Measured in units of the Sun's gravitational acceleration.
[b] Assuming the bulk density varies with particle size according to Eq. (21). Millimeters are in roman font, microns in italics.
[c] Release (ejection) velocity assumed to be zero.
[d] For $\beta = 1$ (motion in a straight line), the eccentricity is by definition infinitely large regardless of the time of release.
[e] Reckoned from the time of perihelion passage of the comet (Sec. 6); minus sign means before, and vice versa.

at the site of the disintegrated nucleus varied from 55° to 106° for the C2 post-perihelion images, but from 97° to nearly 130° for the C3 post-perihelion images. The pseudo-condensation was not very impressive until the phase angle reached about 113°. The maximum effect was observed between ∼10 and ∼22 hours after perihelion, when the phase angle ranged from 119° to 126°. Marcus' phase law predicts a brightness deficit, relative to backscatter, of 0.9 magnitude at a phase angle 55° and 0.3 magnitude at 97°, no enhancement at 106°, and enhancements of 0.25, 0.51, and 0.85 magnitude at, respectively, 113°, 119°, and 126°.

With the exception of the last modeled image in Figure 14, not all dust ejecta observed after perihelion were confined to the space enclosed by the emission fan. As a rule, the fan was accompanied, on the other side of the Sun, by a narrow tail. The tail was in fact an extension of the fan's trailing boundary, but because it usually appeared decoupled from the fan, it could be regarded as a separate feature. The dust along the trailing boundary and in the tail, although both originating in Event 2 (in some images merging with the ejecta from Event 1), differed from one another in the particle size and in that those in the tail did not as yet pass their perihelion points at the times of observation. All grains in the streamer, barely detected in the post-perihelion image in Figure 10, likewise were still approaching perihelion (Sec. 5).

A range of perihelion times of dust particles, released at four different times and subjected to various solar radiation pressure accelerations, is depicted in Table 4, which also lists the perihelion distance and eccentricity of the particles' orbits. The release times refer, respectively, to the termination of dust production, to Events 2 and 1, and to ejection at 20 AU from the Sun. No orbital elements are listed for particles which our modeling showed remained undetected in all eight images: those with $\beta \geq 0.5$ for the end of dust production and with $\beta \geq 0.01$ for the ejecta from a heliocentric distance of 20 AU.

A few examples illustrate the meaning of the difference between the perihelion times of a particle and the disintegrated nucleus. In order that the ejecta from Event 2 arrive at perihelion at the time the image in Figure 10 was taken, 3.3 hours after perihelion, they should have been subjected to a radiation-pressure acceleration of $\beta_{\rm per} = 0.0933$; their perihelion distance should have been 2.94 $R_\odot$ and the eccentricity 1.0080. All Event 2 ejecta with $\beta > \beta_{\rm per}$ arrived at their perihelia later, their perihelion distances were greater than 2.94 $R_\odot$, and their eccentricities greater than 1.0080; and vice versa. Since the Event 2 ejecta that made up the trailing boundary of the fan in Figure 10 had $\beta \ll 0.0933$, they already passed their perihelia, while the ejecta from the same event contained in the tail had $\beta \gg 0.0933$ and did not pass their perihelia as yet. Similarly one finds that $\beta_{\rm per}$ discriminating the two categories of Event 2 ejecta is 0.1557 for a perihelion time coinciding with the time when the image in Figure 11 was taken, 0.2794 for Figure 12, and 0.3884 for Figure 13.

The fact that in the post-perihelion images, such as in Figures 10–12, dust particles that had already passed perihelion populated the same synchrone as dust particles that in the same images were still moving toward perihelion offers evidence that the former particles had survived the passage with no obvious harm, as otherwise the critical segments of the synchrone would be void of dust. The survival of such particles was facilitated by their perihelion distances, which were noticeably greater than 2.67 $R_\odot$. On the other hand, since the perihelion distances of more sizable grains, in the range from many tens of microns across up, were always close to 2.67 $R_\odot$, the impact of the sublimation process — which is an extremely steep function of heliocentric distance close to the Sun — on these grains was much greater, so much so that their larger size might not have been enough to protect them. It thus becomes, counterintuitively, possible that smaller particles are more likely to survive than more sizable ones.

The leading boundary of the post-perihelion emission fan in Figures 10–14, a product of the terminating dust production 3.5 hours before perihelion, demonstrates the presence of particles larger than about 1 micron across ($\beta < 0.3$) but not the smaller ones. All such particles, released at a distance of 5.2 $R_\odot$ from the Sun, passed perihelion before the comet's disintegrated nucleus. The absence of submicron-sized particles (with $\beta > 0.3$) in the ejecta released 3.5 hours before perihelion may be either due to their absence in these ejecta from the very beginning, or due to their sublimation very shortly before or at perihelion. Because of what has just been said about the perihelion distances of such tiny grains, the first option appears to be more likely.

In the ejecta released during Event 2, submicron-sized particles were unquestionably present, as documented by the radiation-pressure accelerations we found in the lagging tail. However, it is not possible to say conclusively whether these grains survived their passage through perihelion or not because they did not reach that point until many days or weeks after the head did, by which time the comet's relics were too faint to observe.

Submicron-sized particles were certainly not present in the pseudo-condensation apparent in a number of C3 post-perihelion images, such as those in Figures 13 or 14. Their absence is dictated by the dynamics: if large grains did fragment profusely into submicron-sized particles many hours after perihelion, there would be a tail pointing away from the Sun. The absence of such tiny particles is also consistent with the strong forward-scattering effect already commented on. As summarized by Marcus (2007, and references therein), particles about 0.1 micron in diameter do not exhibit any forward scattering in the visible light and those around 0.5 micron across do so only to a very limited extent. It is the grains of microns to tens of microns in diameter and of high porosity that are the most efficient forward scatterers at phase angles near 130°.

The complete disintegration of the comet's nucleus and the termination of all activity before perihelion is supported by other evidence as well. In all the images we modeled, the synchrone predicted for dust emitted at perihelion is consistently located way outside the fan-shaped cloud of ejecta. No trace of the comet was detected by the Solar Dynamics Observatory (SDO) in immediate proximity of perihelion.[8] The conclusion is likewise corroborated not only by additional images, not modeled here, taken with the SOHO's C3 coronagraph until November 30 and with the STEREO-A's HI1 imager until December 7, but also by numerous unsuccessful searches via ground-based deep-imaging efforts between December 7 and 16 by Sako et al. (2013) and, as reported by Nakano (2013b), also by K. Kadota, by K. Yoshimoto, and by Y. Ikari, some of them down to a limiting magnitude 19.0. Last but not least, the Hubble Space Telescope failed to find any remnants or debris of the comet[9] on December 18. As for a possible meteor shower associated with the comet, Sekhar & Asher (2014) concluded that not even an ejection velocity of 1 km s^{-1} would be sufficient to deflect a meteoroid from the comet's path to impact the atmosphere of the Earth around the time of transit of the comet's orbit plane on 2014 January 16. Under such circumstances one must be extremely skeptical about any reports of possible detection (Golubev et al. 2014).

[8] See `http://sdoisgo.blogspot.com/2013/11/where-was-comet-ison.html`.

[9] See `http://hubblesite.org/hubble_discoveries/comet_ison.`

4. DISAPPEARANCE OF THE HEAD AND A TIMELINE OF NUCLEUS' FRAGMENTATION

A period of time that includes the time of termination of dust production, 3.5 hours before perihelion, is covered by a series of images taken with the C2 coronagraph on board SOHO. They show a rapidly changing morphology of the comet's head and tail over a span of 4 hours.

4.1. *Disappearance of the Head*

Six selected images from this set are enlarged in Figure 15, in which the first was exposed on November 28.567 UT, about 1.5 hours after the comet entered the field of view of the coronagraph. The general trend is from a bright and well-defined, practically symmetrical round head that gradually widens into a slightly curved tail, to a faint, sharply tipped head that becomes a narrow tail, brightening, up to a point, with increasing distance from the head. Although not apparent from the figure, the tail's axis makes a large angle with the antisolar direction, which keeps increasing with time, amounting to 25° in the first image and 51° in the last.

From cursory inspection, the most rapid fading appears to have taken place in the time span between the second and the fourth images in Figure 15, which includes the critical time 3.5 hours before perihelion (Sec. 3.9). A faint, arrow-shaped extension, steadily lengthening with time, is seen in the images to be protruding from the head on the forward side. It is barely recognizable in the first image, but becomes more prominent beginning with the third image. Concurrently, the leading boundary of the tail (on the left) becomes truncated at the head as if cut off on its outside along a nearly straight line. Again, this feature is marginally detected in the first image, but the resulting asymmetry of the tail relative to its axis is quite apparent from the second image on.

Also evident from Figure 15 is the tail's narrowing down with time. We measured the orientation and curvature of the tail's axis in all six images in Figure 15. The position angles at ∼0°.1 from the head are in column 3 of Table 5. We found that both the orientation

Table 5

Tail Orientation and Morphology in Images Taken with SOHO's C2 Coronagraph Shortly Before Perihelion.

Time of imaging		Position angle				Time of release of truncating ejecta
2013 Nov. (UT)	relative to perihelion	tail's axis	Event 2 synchr.	Difference	tail's cutoff	
28.567	$t_\pi - 5.1$ hr	254°	253°.5	+0°.5	...	.....
28.608	$t_\pi - 4.1$ hr	250	250.8	−0.8	239°	$t_\pi - 15.3$ hr
28.649	$t_\pi - 3.1$ hr	247	247.3	−0.3	237	$t_\pi - 16.3$ hr
28.683	$t_\pi - 2.3$ hr	244	243.3	+0.7	234	$t_\pi - 16.6$ hr
28.717	$t_\pi - 1.5$ hr	238	237.7	+0.3	228	$t_\pi - 12.9$ hr
28.733	$t_\pi - 1.1$ hr	234	234.2	−0.2	226	$t_\pi - 15.8$ hr

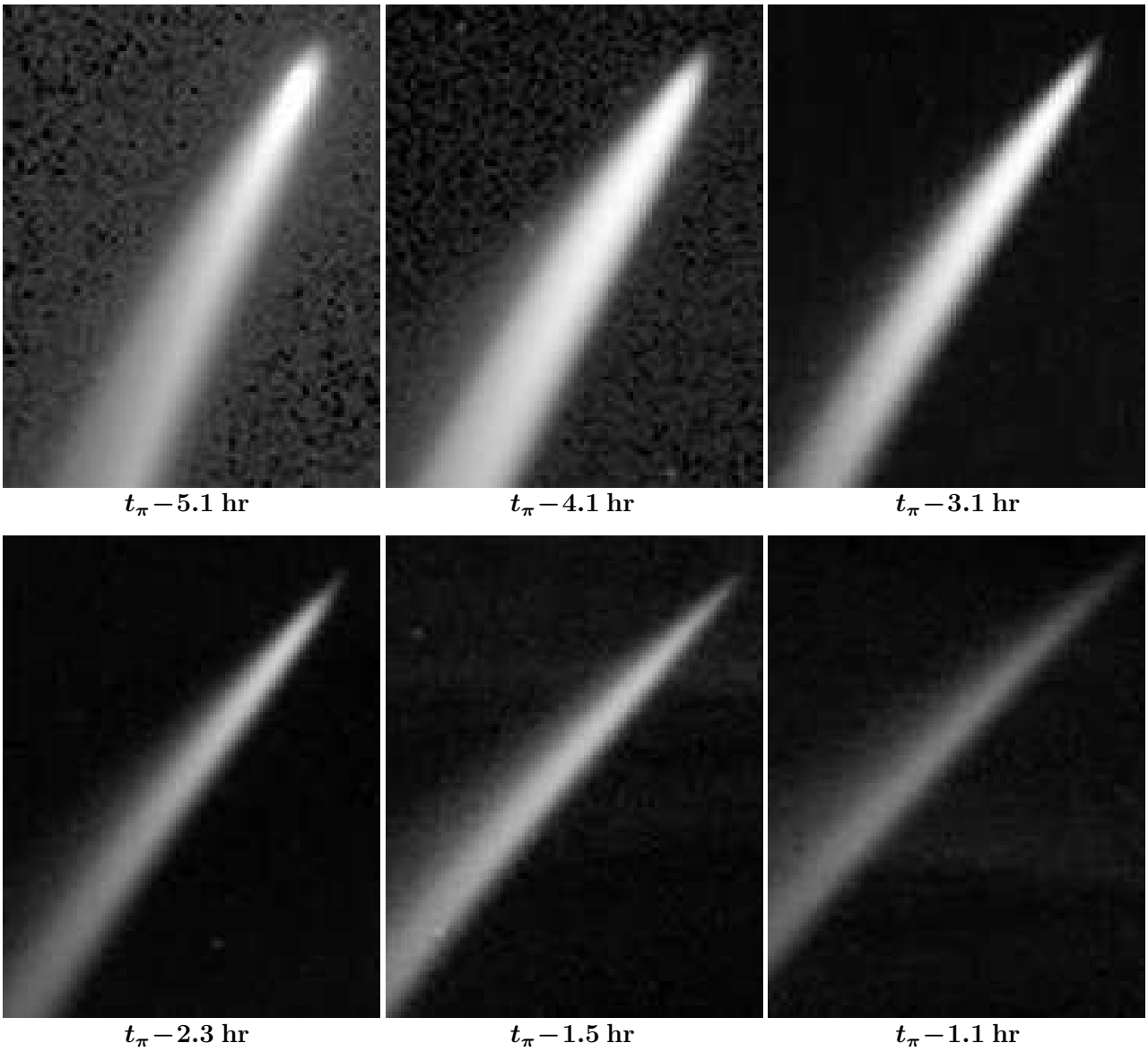
CHANGING MORPHOLOGY OF THE HEAD OF COMET C/2012 S1 DURING 4 HOURS SHORTLY BEFORE PERIHELION
$t_\pi - 5.1$ hr
$t_\pi - 4.1$ hr
$t_\pi - 3.1$ hr
$t_\pi - 2.3$ hr
$t_\pi - 1.5$ hr
$t_\pi - 1.1$ hr

Figure 15. Rapidly changing morphology of comet C/2012 S1 shortly before perihelion, at time t_π, resulting in the disappearance of the head in the images taken with the C2 coronagraph on board SOHO. The images were taken, respectively, on November 28.567, 28.608, 28.649, 28.683, 28.717, and 28.733 UT, when the comet was 6.9, 5.9, 5.0, 4.2, 3.5, and 3.2 $R_\odot$ from the Sun. The phase angles ranged from 87° to 51° from the upper left to the lower right. Along the diagonal each image measures 15.7 arcmin, or, on the average, 670 000 km, increasing by 5600 km between the first and the last images. The Sun is to the right. Note a faint, lengthening extension sticking out of the ever fuzzier head on the sunward side; a truncated leading boundary of part of the tail, starting at the tip and becoming progressively more conspicuous with time; and the tail's concurrently decreasing width. (Image credit: ESA/NASA/LASCO consortium.)

and the bending are in excellent agreement with those of the synchrone for the Event 2 ejecta. This is not surprising because this match consistently resulted from all images taken before perihelion and less than 1 day after perihelion that were modeled in Sec. 3. The identity of the tail with the debris from Event 2 allowed us to estimate the expansion velocity of dust particles. From the width near the lower left corner of each image, about 10 arcmin from the tip of the head, we find, after accounting for a small contribution from the ∼3-day duration of Event 2, the following velocities: (i) 96 m s^{-1} for particles whose $\beta = 0.019$, that is, about 47 microns in diameter according to Eq. (21) from the image taken 5.1 hours before perihelion; (ii) 64 m s^{-1} for particles 66 microns in diameter from the image taken 3.1 hours before perihelion; and (iii) 40 m s^{-1} for particles 91 microns in diameter from the image taken 1.5 hours before perihelion. However, these last particles are also situated about 6.4 arcmin from the head in the image in the upper left corner of Figure 15, and that tail's width suggests that their expansion velocity was at least 75 m s^{-1}, a value nearly twice as high. This discrepancy must mean that

the tail's observed width is a product of at least two separate components that partly overlap one another. This argument also explains the truncated nature of the tail in the rest of the images, which we address next, and the apparent failure of the tail, far from the head, to widen with increasing distance from it in the last two images in Figure 15.

The measured position angles of the line, along which the tail is truncated from the tip to the lower left in the images in Figure 15, are listed in column 6 of Table 5. The measurement could not be done in the first image, in which the truncation is hardly at all visible, but was relatively easy in the rest of them. This exercise could also have been performed using a dozen or so additional C2 images that are available, but the results for the five cases are unequivocal enough that there was no need to extend the sample. The last column of Table 5 presents the release times for the synchrones that correspond to the measured position angles. An average of the five entries is 15.4 ± 1.5 hours before perihelion, equivalent to a heliocentric distance of 0.07 AU or $\sim$15 $R_\odot$. This is the time of termination of dust production during an outburst, which we call *Event 3* and which accounts for the second tail in Figure 15 that overlaps the tail made up of the Event 2 ejecta. The beginning of this third event cannot be ascertained from the features in the figure because of the overlap.

Two correlations should be mentioned. One, the feature that causes the truncated tail in Figure 15 is undoubtedly identical with what we called a "beard" in Sec. 3.3, a feature so conspicuously apparent in Figure 9. Note that the STEREO-A image in that figure and the fifth of the six C2 images in Figure 15 were taken only a couple of minutes apart, so the same feature is expected to show in both under at least moderately favorable projection conditions. Thus, indeed, it is the beard that causes in Figure 15 the tail to be truncated in five images and to fail to widen, in the last two images, far from the head with increasing distance from it. Two, the time of termination of this third emission event practically coincides with the peak on the intrinsic-brightness curve in close proximity of perihelion in Figure 5, based on Knight & Battams' (2014) C3 clear-filter magnitudes. From this correlation one can expect that Event 3 began at the time of the last upswing on the intrinsic-brightness curve in Figure 5, that is, 2.4 days before perihelion, when the comet was 40 $R_\odot$ from the Sun and its nucleus already extensively fragmented (Sec. 4.2).

The sharp forward pointing extension from the head's tip cannot be interpreted as a product of near edge-on projection, because the SOHO spacecraft was about 42° out of the comet's orbital plane. The feature is generally too short to measure its position angle with adequate accuracy. However, the last two images suggest that it was aligned with the axis of the Event 2's tail. Being ahead of the rest of the comet in the orbit, the forward extension was necessarily the location of the *most massive fragments* left from the original nucleus during its extensive fragmentation in the course of Events 1 and 2 (Sec. 4.2). This implies that it is this *extension's forward tip* — rather than the head's sunward end — that pinpointed the site of the original nucleus in Figure 15, implying that the lengthening of the extension with time was due to the motion of the head relative to the extension's tip, a conclusion that is consistent with our orbital results (Sec. 6). The extension should have thus contained a lined-up procession of boulder- and pebble-sized objects and other coarse debris with near-zero differential velocities, imaged at a low spatial resolution. The feature is reminiscent of the elongated cloud of subnuclei of comet C/1999 S4 detected, at much higher resolution, by the Hubble Space Telescope (Weaver et al. 2001). The head itself contained a debris of less sizable dust particles whose dimensions may not have exceeded millimeters. The head lagged behind the extension primarily because of the differential effects of solar radiation pressure, just as the tail lagged behind the head. As dust was driven away from the Sun, the tail gradually contained ever larger particles; their lower ejection velocities may explain the mentioned narrowing down of the tail. A near "dissolution" of the entire object, best apparent in the last image of Figure 15, is evidence of the disintegration of the debris itself, after the termination of dust production. We suggest that dust particle sublimation may have played, in this near-perihelion stage of the comet's disintegration, a more important role than fragmentation. The sharp boundary of the truncated tail, signaling the termination of the major dust production some 15 hours before perihelion, could represent a precursor to the final breakup of more sizable debris, which continued to produce dust, at progressively lower rates, for another half day, until $\sim$3.5 hours before perihelion, and which accounted for the leading boundary of the fan-shaped feature that showed up in all post-perihelion images taken with the SOHO and STEREO coronagraphs.

4.2. *Timeline of the Comet's Disintegration*

The fragmentation sequence that led to the complete disintegration of the comet looks like a puzzle whose individual pieces finally appear to fall into place. We suggest below that the comet's highly variable water production rate during November played a pivotal role in determining the timeline and properties of this process.

To interpret the observed water production rate as a function of time, we introduce an averaged water sublimation rate, $\langle Z_{\rm subl} \rangle$, from a unit surface area on the sunlit hemisphere of an intact (unaffected by fragmentation) active icy nucleus as a function of the distance from the Sun by integrating over all zenith distances of the Sun, normalizing it in terms of the subsolar sublimation rate, scaling it by the size of the nucleus, and comparing it with observation. The sublimation rate is derived from a model in which the surface insolation is assumed to be spent on water sublimation and thermal reradiation, but not on heat conduction into the nucleus. With a Bond albedo near zero and a unit emissivity of the surface, a solution for the sublimation rate per unit surface area at the Sun's zenith distance ϑ and a heliocentric distance r, $Z_{\rm subl}(\vartheta, r)$, is found in an empirical form (Sekanina 1988)

$$Z_{\rm subl}(\vartheta, r) = Z_0(r)\, \Omega(\vartheta, r), \qquad (22)$$

where $Z_0(r)$ is the sublimation rate at a subsolar point at distance r, and $0 \le \Omega(\vartheta, r) \le 1$ is a relative sublimation rate at a zenith angle ϑ,

$$\begin{aligned} \Omega(\vartheta, r) &= \cos\vartheta - f_0(r) \sin^2\vartheta \quad && \text{for } 0 \le \vartheta \le \vartheta_0(r), \\ &= 0 && \text{for } \vartheta > \vartheta_0(r). \end{aligned} \qquad (23)$$

The expressions for Z_0, f_0 and ϑ_0, which allow one to compute the model's expected sublimation rates with a relative accuracy to better than ±1 percent at heliocentric distances $r < 1$ AU, are presented in Sekanina (1988).

The averaged rate $\langle Z_{\rm subl}\rangle$ per unit surface area at time t and a distance r is given by

$$\langle Z_{\rm subl}\rangle = Z_0 \int_0^{\frac{1}{2}\pi} \sin\vartheta\ \Omega(\vartheta, r)\, d\vartheta$$
$$= Z_0 \left[\sin^2\vartheta_0 - \tfrac{4}{3} f_0 (1-\cos\vartheta_0)^2 \left(1+\tfrac{1}{2}\cos\vartheta_0\right)\right]. \quad (24)$$

If $D_0(t)$ is the nucleus' diameter and $Q_{\rm obs}(t)$ the observed production rate of water at time t, the modeled production rate from the nucleus' entire sunlit hemisphere is $Q_{\rm subl}(t) = \frac{1}{2}\pi D_0^2 \langle Z_{\rm subl}\rangle(t)$ and the effective observed sublimation area is $X_{\rm obs}(t) = Q_{\rm obs}(t)/\langle Z_{\rm subl}\rangle(t)$. A convenient measure of the outgassing rate is a dimensionless quantity $\Theta_{\rm subl}(t)$, equal to the observed sublimation area expressed in units of the hemispherical area of the nucleus or to the ratio of the observed and modeled production rates,

$$\Theta_{\rm subl}(t) = \frac{X_{\rm obs}(t)}{\frac{1}{2}\pi D_0^2(t)} = \frac{Q_{\rm obs}(t)}{Q_{\rm subl}(t)}. \quad (25)$$

In the following we compare this model with the measured water production and total mass-loss rates of C/2012 S1 between the time of close encounter with Mars on October 1 and the time of complete disintegration on November 28, as referred to in Sec. 3.9. The model depends on three parameters: the nucleus' initial diameter (at the time of Mars encounter), its bulk density, and the dust-to-water mass production rate ratio. To examine a range of plausible solutions, we present in an extensive Table 6 not only the nominal case (Sec. 2.4), referred to as *Model G*, but also scenarios for seven other combinations of the three parameters. The table is organized in a manner as follows. Relevant parameter-independent quantities are listed for a selected set of dates between October 1 and November 28 in the first part of the table. Each date represents actually a 24-hour interval that starts 12 hours before and ends 12 hours after the tabulated time. This arrangement complies with Combi et al.'s (2014) daily water production averages, whose sequence, extrapolated beyond the original 28-day interval, is tabulated as an *observed production rate* $Q_{\rm obs}$. Because the production rates between October 1 and November 10 varied very slowly with time, this period is represented by only four entries. Besides the rates, the first part of Table 6 also presents, as a function of time, a *modeled averaged sublimation rate per unit surface area*, $\langle Z_{\rm subl}\rangle(t_{\rm obs})$, derived from Eq. (24), and an *effective sublimation area*, $X_{\rm subl}(t_{\rm obs})$, derived from the expression in the text between Eqs. (24) and (25).

The second part of Table 6 is divided into sections, one section per scenario. Each scenario satisfies the basic condition, requiring that the combination of the three parameters — the initial diameter, $D_0(t_{\rm enc})$, the bulk density, ρ, and the dust-to-water mass production rate ratio, $\Re_0$ — satisfy an equality between the mass of the nucleus, $\mathcal{M}_0(t_{\rm enc})$, at the time of encounter with Mars, $t_{\rm enc}$, and the mass-loss rate integrated from $t_{\rm enc}$ to the time of the comet's complete disintegration, $t_\star$, 3.5 hours before perihelion (Sec. 3.9):

$$\mathcal{M}_0(t_{\rm enc}) = \tfrac{1}{6}\pi\rho D_0^3(t_{\rm enc}) = \int_{t_{\rm enc}}^{t_\star} \mu_0 Q_{\rm obs}(t)\,(1+\Re_0)\, dt$$
$$= 2.32\times 10^{13}\,(1+\Re_0), \quad (26)$$

where $\mathcal{M}_0(t_{\rm enc})$ is in grams and $\mu_0 = 2.99\times 10^{-23}$ gram is the mass of a water molecule.

For each scenario Table 6 provides (i) a modeled water production rate, $Q_{\rm subl}$, at the middle of each time interval, $t_{\rm obs}$, from the entire sunlit hemisphere of an *intact* spherical nucleus of the given (gradually dwindling) dimensions; (ii) its remaining mass, $\mathcal{M}_0(t_{\rm fin})$, at the end of each 24-hour interval, $t_{\rm fin} = t_{\rm obs} + 0.5$ day, expressed by $\mathcal{M}_0(t_{\rm fin}) = \mu_0(1+\Re_0)\int_{t_{\rm fin}}^{t_\star} Q_{\rm obs}(t)\, dt$; and (iii) a water production rate ratio, $\Theta_{\rm subl}(t_{\rm obs})$, defined by Eq. (25). The water sublimation rate $Q_{\rm subl}$ represents an ideal, hypothetical case, whereas a ratio $\Theta_{\rm subl}$ measures a "degree" of deviation from this case. If $\Theta_{\rm subl} < 1$, only a fraction of the sunlit hemisphere's surface is active. On the other hand, a ratio $\Theta_{\rm subl} > 1$, varying smoothly with time, typically indicates a major contribution to the total water production from sublimating icy-dust grains in the comet's atmosphere. Finally, a ratio $\Theta_{\rm subl} \gg 1$, varying erratically with time, suggests an explosion, a likely result of fragmentation that opens up the interior of the nucleus.

The first two scenarios in Table 6, *Models A* and *B*, are based on the assumption of the comet's maximum nuclear diameter at the time of Mars encounter (Sec. 2.3); in addition, a nominal dust-to-water production rate ratio of $\Re_0 = 1.5$ is adopted in the first case, a nominal bulk density of $\rho = 0.4$ g cm^{-3} in the second case. In the next two scenarios, *C* and *D*, the ratio $\Re_0$ is varied by a factor of two either way, with the bulk density kept at its nominal value. In the remaining four scenarios, *E* through *H*, the bulk density is varied from 0.2 to 0.5 g cm^{-3}, with $\Re_0$ kept at its nominal value.

Inspection of Table 6 suggests that the adoption of the maximum diameter of 1 km for the nucleus at the time of Mars encounter leads to an improbably low density for Model A and to extremely high dust-to-water production rate ratio for Model B; in addition, from Sec. 2.4 the particle size distribution function would have to be extraordinarily flat, with $\tau \lesssim 3$. We doubt that these two are realistic scenarios and we ignore them in the following. Since all remaining scenarios, Models C–H, require that the nucleus at Mars encounter be less than 1 km across, a significant contamination by dust of the brightest pixel in the HiRISE images, already suggested in Sec. 2.4 on the basis of what is now called Model G, appears to be corroborated.

On the other hand, the diameter $D_0(t_{\rm enc})$ in a range of 0.6 to 0.8 km, implied by Models C–H, requires that the observed water production signature at the time of Mars encounter was due mostly to icy-dust grains in the atmosphere, since the ratio $\Theta_{\rm subl} \approx 2.6$–$5.1$. This ratio is seen to be systematically decreasing between October 1 and November 10, which is due largely to the sluggish rate of increase in the water production rate in the period October 1–24. As late as 18 days before perihelion, we still fail to see any sign of the comet's impending cataclysmic demise.

Table 6

Water Sublimation Models for Comet C/2012 S1 (2013 October 1–November 16).

	Midtime, t_{obs}, of 24-hour interval, from $t_{obs}-12$ hr to $t_{obs}+12$ hr (2013 UT)								
Quantity	Oct. 1.0	Oct. 24.0	Nov. 4.0	Nov. 10.0	Nov. 12.0	Nov. 13.0	Nov. 14.0	Nov. 15.0	Nov. 16.0
Time from perihelion, $t_{obs}-t_\pi$ (days)	−58.78	−36.78	−24.78	−18.78	−16.78	−15.78	−14.78	−13.78	−12.78
Heliocentric distance, r_{obs} (AU)	1.651	1.204	0.923	0.765	0.709	0.680	0.650	0.620	0.589
Observed production rate (10^{28} s^{-1})[a]	1.17	1.58	2.69	2.76	6.67	10.66	44.86	24.20	31.34
Modeled averaged sublimation rate per unit surface area (10^{28}km^{-2}s^{-1})	0.43	0.94	1.72	2.59	3.06	3.35	3.69	4.09	4.56
Effective sublimation area (km^2)	2.70	1.68	1.57	1.06	2.18	3.18	12.15	5.92	6.87
MODEL A: Nucleus' diameter at Mars encounter = 1.00 km Bulk density = 0.11 g cm^{-3} Dust-to-water ratio by mass = 1.5									
Nucleus' production rate (10^{28} s^{-1})[b]	0.68	1.44	2.59	3.86	4.54	4.94	5.41	5.85	6.34
Remaining mass of nucleus (10^{14} g)[c]	0.581	0.562	0.546	0.534	0.527	0.521	0.492	0.476	0.456
Sublimation rate ratio, $\Theta_{subl}(t_{obs})$	1.7	1.1	1.0	0.7	1.5	2.2	8.3	4.1	4.9
MODEL B: Nucleus' diameter at Mars encounter = 1.00 km Bulk density = 0.40 g cm^{-3} Dust-to-water ratio by mass = 8.0									
Nucleus' production rate (10^{28} s^{-1})[b]	0.68	1.44	2.59	3.86	4.53	4.94	5.41	5.85	6.34
Remaining mass of nucleus (10^{14} g)[c]	2.093	2.024	1.967	1.924	1.900	1.876	1.771	1.715	1.642
Sublimation rate ratio, $\Theta_{subl}(t_{obs})$	1.7	1.1	1.0	0.7	1.5	2.2	8.3	4.1	4.9
MODEL C: Nucleus' diameter at Mars encounter = 0.58 km Bulk density = 0.40 g cm^{-3} Dust-to-water ratio by mass = 0.75									
Nucleus' production rate (10^{28} s^{-1})[b]	0.23	0.48	0.87	1.30	1.52	1.66	1.81	1.96	2.13
Remaining mass of nucleus (10^{14} g)[c]	0.406	0.393	0.382	0.374	0.369	0.364	0.344	0.333	0.319
Sublimation rate ratio, $\Theta_{subl}(t_{obs})$	5.1	3.3	3.1	2.1	4.4	6.4	24.7	12.3	14.7
MODEL D: Nucleus' diameter at Mars encounter = 0.76 km Bulk density = 0.40 g cm^{-3} Dust-to-water ratio by mass = 3.0									
Nucleus' production rate (10^{28} s^{-1})[b]	0.39	0.84	1.51	2,24	2.63	2.87	3.14	3.40	3.68
Remaining mass of nucleus (10^{14} g)[c]	0.926	0.895	0.870	0.851	0.841	0.830	0.784	0.759	0.726
Sublimation rate ratio, $\Theta_{subl}(t_{obs})$	3.0	1.9	1.8	1.2	2.5	3.7	14.3	7.1	8.5
MODEL E: Nucleus' diameter at Mars encounter = 0.82 km Bulk density = 0.20 g cm^{-3} Dust-to-water ratio by mass = 1.5									
Nucleus' production rate (10^{28} s^{-1})[b]	0.46	0.97	1.75	2.60	3.06	3.33	3.65	3.94	4.27
Remaining mass of nucleus (10^{14} g)[c]	0.579	0.560	0.544	0.532	0.526	0.519	0.490	0.475	0.454
Sublimation rate ratio, $\Theta_{subl}(t_{obs})$	2.6	1.6	1.5	1.1	2.2	3.2	12.3	6.1	7.3
MODEL F: Nucleus' diameter at Mars encounter = 0.72 km Bulk density = 0.30 g cm^{-3} Dust-to-water ratio by mass = 1.5									
Nucleus' production rate (10^{28} s^{-1})[b]	0.35	0.74	1.33	1.99	2.33	2.54	2.78	3.01	3.26
Remaining mass of nucleus (10^{14} g)[c]	0.579	0.559	0.544	0.532	0.525	0.518	0.490	0.474	0.454
Sublimation rate ratio, $\Theta_{subl}(t_{obs})$	3.3	2.1	2.0	1.4	2.9	4.2	16.1	8.0	9.6
MODEL G[d]: Nucleus' diameter at Mars encounter = 0.65 km Bulk density = 0.40 g cm^{-3} Dust-to-water ratio by mass = 1.5									
Nucleus' production rate (10^{28} s^{-1})[b]	0.29	0.61	1.10	1.64	1.93	2.10	2.30	2.49	2.70
Remaining mass of nucleus (10^{14} g)[c]	0.580	0.561	0.545	0.533	0.527	0.520	0.491	0.476	0.455
Sublimation rate ratio, $\Theta_{subl}(t_{obs})$	4.0	2.6	2.4	1.7	3.5	5.1	19.5	9.7	11.6
MODEL H: Nucleus' diameter at Mars encounter = 0.61 km Bulk density = 0.50 g cm^{-3} Dust-to-water ratio by mass = 1.5									
Nucleus' production rate (10^{28} s^{-1})[b]	0.25	0.53	0.95	1.41	1.66	1.81	1.98	2.14	2.32
Remaining mass of nucleus (10^{14} g)[c]	0.579	0.560	0.544	0.533	0.526	0.519	0.490	0.475	0.455
Sublimation rate ratio, $\Theta_{subl}(t_{obs})$	4.7	3.0	2.8	2.0	4.0	5.9	22.7	11.3	13.5

[a]Daily averages of the water production rate from Combi et al. (2014) for the dates October 24 through November 16; extrapolated to October 1 by applying a law $r^{-0.95}$ (Figure 2) linked to Combi et al.'s daily average for October 24.

[b]Derived from the described water sublimation model for an intact spherical nucleus of given dimensions at time t_{obs}, outgassing from the entire sunlit hemisphere.

[c]Derived from the described water sublimation model and the adopted dust-to-water mass production rate ratio; the mass refers to the end of the 24-hour period of time. From November 13–14 on, the nucleus was made up of a progressively increasing number of fragments.

[d]Nominal model (Sec. 2.4).

Table 6 (continued)

WATER SUBLIMATION MODELS FOR COMET C/2012 S1 (2013 NOVEMBER 17–28).

Quantity	Midtime, t_{obs}, of 24-hour interval, from $t_{obs}-12$ hr to $t_{obs}+12$ hr (2013 UT)								
	Nov. 17.0	Nov. 18.0	Nov. 19.0	Nov. 20.0	Nov. 21.0	Nov. 22.0	Nov. 24.0	Nov. 26.0	Nov. 28.0
Time from perihelion, $t_{obs}-t_\pi$ (days)	−11.78	−10.78	−9.78	−8.78	−7.78	−6.78	−4.78	−2.78	−0.78
Heliocentric distance, r_{obs} (AU)	0.557	0.525	0.491	0.456	0.420	0.382	0.300	0.206	0.083
Observed production rate (10^{28} s^{-1})[a]	59.17	139.7	119.2	116.7	101.1	(80)	(15)	(15)	(5)
Modeled averaged sublimation rate per unit surface area (10^{28}km^{-2}s^{-1})	5.14	5.84	6.73	7.88	9.38	11.5	19.1	42.3	287
Effective sublimation area (km^2)	11.5	23.9	17.7	14.8	10.8	(6.97)	(0.78)	(0.35)	(0.02)
MODEL A: Nucleus' diameter at Mars encounter = 1.00 km Bulk density = 0.11 g cm^{-3} Dust-to-water ratio by mass = 1.5									
Nucleus' production rate (10^{28} s^{-1})[b]	6.97	7.58	7.87	7.78	7.57	7.11	5.90	9.00	34.4
Remaining mass of nucleus (10^{14} g)[c]	0.418	0.328	0.252	0.177	0.112	0.060	0.031	0.017	<0.001
Sublimation rate ratio, $\Theta_{subl}(t_{obs})$[b]	8.5	18.4	15.2	15.0	13.3	11.2	2.5	1.7	0.15
MODEL B: Nucleus' diameter at Mars encounter = 1.00 km Bulk density = 0.40 g cm^{-3} Dust-to-water ratio by mass = 8.1									
Nucleus' production rate (10^{28} s^{-1})[b]	6.97	7.58	7.86	7.77	7.55	7.08	5.80	8.73	31.9
Remaining mass of nucleus (10^{14} g)[c]	1.505	1.181	0.904	0.633	0.398	0.212	0.108	0.057	<0.001
Sublimation rate ratio, $\Theta_{subl}(t_{obs})$[b]	8.5	18.4	15.2	15.0	13.4	11.3	2.6	1.7	0.16
MODEL C: Nucleus' diameter at Mars encounter = 0.58 km Bulk density = 0.40 g cm^{-3} Dust-to-water ratio by mass = 0.75									
Nucleus' production rate (10^{28} s^{-1})[b]	2.34	2.54	2.64	2.61	2.54	2.38	1.97	2.99	11.3
Remaining mass of nucleus (10^{14} g)[c]	0.292	0.229	0.176	0.123	0.078	0.042	0.022	0.012	<0.001
Sublimation rate ratio, $\Theta_{subl}(t_{obs})$[b]	25.3	55.0	45.2	44.7	39.9	33.6	7.6	5.0	0.44
MODEL D: Nucleus' diameter at Mars encounter = 0.76 km Bulk density = 0.40 g cm^{-3} Dust-to-water ratio by mass = 3.0									
Nucleus' production rate (10^{28} s^{-1})[b]	4.05	4.40	4.56	4.51	4.38	4.10	3.34	4.99	17.7
Remaining mass of nucleus (10^{14} g)[c]	0.666	0.522	0.399	0.279	0.175	0.093	0.047	0.024	<0.001
Sublimation rate ratio, $\Theta_{subl}(t_{obs})$[b]	14.6	31.8	26.1	25.9	23.1	19.5	4.5	3.0	0.28
MODEL E: Nucleus' diameter at Mars encounter = 0.82 km Bulk density = 0.20 g cm^{-3} Dust-to-water ratio by mass = 1.5									
Nucleus' production rate (10^{28} s^{-1})[b]	4.70	5.11	5.30	5.24	5.09	4.77	3.89	5.84	21.0
Remaining mass of nucleus (10^{14} g)[c]	0.416	0.327	0.250	0.175	0.110	0.058	0.030	0.015	<0.001
Sublimation rate ratio, $\Theta_{subl}(t_{obs})$[b]	12.6	27.4	22.5	22.3	19.9	16.8	3.9	2.6	0.24
MODEL F: Nucleus' diameter at Mars encounter = 0.72 km Bulk density = 0.30 g cm^{-3} Dust-to-water ratio by mass = 1.5									
Nucleus' production rate (10^{28} s^{-1})[b]	3.58	3.89	4.04	3.99	3.88	3.63	2.95	4.40	15.5
Remaining mass of nucleus (10^{14} g)[c]	0.416	0.326	0.249	0.174	0.109	0.058	0.029	0.015	<0.001
Sublimation rate ratio, $\Theta_{subl}(t_{obs})$[b]	16.5	35.9	29.5	29.2	26.1	22.0	5.1	3.4	0.32
MODEL G[d]: Nucleus' diameter at Mars encounter = 0.65 km Bulk density = 0.40 g cm^{-3} Dust-to-water ratio by mass = 1.5									
Nucleus' production rate (10^{28} s^{-1})[b]	2.96	3.22	3.34	3.31	3.22	3.02	2.49	3.77	14.1
Remaining mass of nucleus (10^{14} g)[c]	0.417	0.328	0.251	0.176	0.111	0.059	0.031	0.016	<0.001
Sublimation rate ratio, $\Theta_{subl}(t_{obs})$[b]	20.0	43.4	36.7	35.3	31.4	26.5	6.0	4.0	0.35
MODEL H: Nucleus' diameter at Mars encounter = 0.61 km Bulk density = 0.50 g cm^{-3} Dust-to-water ratio by mass = 1.5									
Nucleus' production rate (10^{28} s^{-1})[b]	2.55	2.77	2.88	2.84	2.76	2.59	2.12	3.19	11.6
Remaining mass of nucleus (10^{14} g)[c]	0.417	0.327	0.250	0.175	0.110	0.059	0.030	0.016	<0.001
Sublimation rate ratio, $\Theta_{subl}(t_{obs})$[b]	23.2	50.4	41.4	41.0	36.6	30.9	7.1	4.7	0.43

[a]Daily averages of the water production rate from Combi et al. (2014) for the dates November 17 through 21; extrapolated to November 28 by mimicking the variations in the HCN production rate (see the IRAM website in footnote 5) and linked to Combi et al.'s daily average for November 21; these numbers are parenthesized.

[b]Derived from the described water sublimation model for an intact spherical nucleus of given dimensions at time t_{obs}, outgassing from the entire sunlit hemisphere.

[c]Derived from the described water sublimation model and the adopted dust-to-water mass production rate ratio by mass; the mass refers to the end of the 24-hour period of time. During the entire period of November 17–28, the nucleus was made up of a progressively increasing number of fragments.

[d]Nominal model (Sec. 2.4).

About 17 days before perihelion, on November 11–12, the downturn in $\Theta_{\rm subl}$ was suddenly reversed and on November 14 the ratio reached a peak between 12 and 25 in Models C through H, declining back to between 6 to 15 during the next two days. A new surge of water release began November 17, when $\Theta_{\rm subl}$ jumped by a factor of 1.7, and the next day by another factor of 2.2. For the nominal model, G, the increase in $\Theta_{\rm subl}$ between November 10 and 18 amounted to 41.7, up a factor of more than 25. Afterwards, the ratio began to decrease, quite possibly at an accelerated rate. The behavior of $\Theta_{\rm subl}$ is somewhat reminiscent, in the period from November 11 on, of the activity cycles (Sec. 2.1), with an ignition point on November 11, an expansion stage terminated at a stagnation point on November 18, and a depletion stage ending on November 28.

However, two enormous peaks and the temporal extent suggested that much more was at stake in this case than an injection of a cloud of icy grains into the atmosphere. The persistence of exceptionally high levels of water production and the erratic variations in its rate were diagnostic of a major augmentation of the sublimation surface, which is hard to achieve without suddenly opening the nucleus' interior by its severe fragmentation.

Let us assume that sublimating fragments of the nucleus satisfy a size-distribution law, such that the number of fragments whose effective diameters are between D and $D+dD$ is $f(D)dD$ and the minimum and maximum diameters are, respectively, $D_{\rm min}$ and $D_{\rm max}$.[10] Accordingly, the total number, $N_{\rm frg}$, of fragments is

$$\int_{D_{\rm min}}^{D_{\rm max}} f(D)\,dD = N_{\rm frg}. \qquad (27)$$

From Eq. (25), the fragments' total sublimation area is

$$\int_{D_{\rm min}}^{D_{\rm max}} \tfrac{1}{2}\pi D^2 f(D)\,dD = \tfrac{1}{2}\pi D_0^2 \Theta_{\rm subl}. \qquad (28)$$

Assuming that all fragments were sublimating, a sum of their masses, $\mathcal{M}_{\rm frg}(D)$, should equal the mass of the nucleus, $\mathcal{M}_0$, at the onset of its fragmentation, $t_{\rm frg}$,

$$\int_{D_{\rm min}}^{D_{\rm max}} \mathcal{M}_{\rm frg}(D)\, f(D)\,dD = \mathcal{M}_0, \qquad (29)$$

where, as before, $\mathcal{M}_0 = \frac{1}{6}\pi\rho D_0^3$ for an intact nucleus at $t_{\rm frg}$, with ρ being a constant bulk density. Similar relation also applies to any fragment.

To illustrate the implications of these conditions in general and of the magnitude of $\Theta_{\rm subl}$ in particular, we adopt for the size distribution a law

$$f(D)\,dD = C_{\rm D} D^{-3.5}\,dD, \qquad (30)$$

where $C_{\rm D}$ is a constant. This law is identical with the size distribution law for a collisional model of asteroids and their debris, derived by Dohnanyi (1969). Although the fragmentation mechanisms are different, explosive phenomena are involved in both cases.

[10] The definition of the minimum fragment diameter, $D_{\rm min}$, excludes of course dust, whose mass is expressed through the ratio $\Re_0$. However, in an advanced stage of the fragmentation process, the difference between the smallest fragments and the largest dust particles may become blurred.

The integrals (27) to (29) now become

$$N_{\rm frg} = 0.4\, C_{\rm D} D_{\rm min}^{-2.5}\left[1-\left(\frac{D_{\rm min}}{D_{\rm max}}\right)^{\frac{5}{2}}\right],$$

$$D_0^2\,\Theta_{\rm subl} = 2\, C_{\rm D} D_{\rm min}^{-\frac{1}{2}}\left[1-\left(\frac{D_{\rm min}}{D_{\rm max}}\right)^{\frac{1}{2}}\right],$$

$$D_0^3 = 2\, C_{\rm D} D_{\rm max}^{\frac{1}{2}}\left[1-\left(\frac{D_{\rm min}}{D_{\rm max}}\right)^{\frac{1}{2}}\right]. \qquad (31)$$

Dividing the third equation by the second, we obtain

$$\frac{D_{\rm min}}{D_0}\,\frac{D_{\rm max}}{D_0} = \frac{1}{\Theta_{\rm subl}^2}. \qquad (32)$$

Dividing the first equation by the second, we find, after inserting from Eq. (32) for $D_{\rm min}/D_0$,

$$N_{\rm frg} = 0.2\,\Theta_{\rm subl}^5\left(\frac{D_{\rm max}}{D_0}\right)^2\left[1+\sum_{k=1}^{4}\left(\Theta_{\rm subl}\,\frac{D_{\rm max}}{D_0}\right)^{-k}\right]. \qquad (33)$$

We note that these conditions are independent of the nucleus' size, because the dimensions of fragments enter the equations only as fractions of the parent's dimensions. However, we have two equations for three unknowns, $N_{\rm frg}$, $D_{\rm min}$, and $D_{\rm max}$, so one of them is still a free parameter. We choose $D_{\rm max}$, the diameter of the largest fragment.

We now examine two extreme possibilities with major implications. One is a case in which the largest fragment has a diameter considerably (orders of magnitude) greater than the smallest fragment, $D_{\rm min} \ll D_{\rm max}$, but comparable to the parent's diameter, $D_{\rm max} = \Gamma_{\rm frg} D_0$, where $\Gamma_{\rm frg}$ is a number moderately smaller than unity. The diameter of the smallest fragment is then found to equal $D_{\rm min} = D_0/(\Theta_{\rm subl}^2\Gamma_{\rm frg})$ and, since $\Theta_{\rm subl}\Gamma_{\rm frg} \gg 1$,

$$N_{\rm frg} \simeq 0.2\,\Theta_{\rm subl}^5\,\Gamma_{\rm frg}^2\left[1+(\Theta_{\rm subl}\,\Gamma_{\rm frg})^{-1}\right]. \qquad (34)$$

At the other extreme, let the largest fragment be much smaller than the nucleus, $D_{\rm max} \ll D_0$, but just moderately greater than the smallest fragment, $D_{\rm min} = \Gamma_{\rm frg} D_{\rm max}$, where again $\Gamma_{\rm frg} < 1$. Then $D_{\rm min} = D_0\sqrt{\Gamma_{\rm frg}}/\Theta_{\rm subl}$ and

$$N_{\rm frg} \simeq 0.2\,\frac{\Theta_{\rm subl}^3}{\Gamma_{\rm frg}\left(1-\sqrt{\Gamma_{\rm frg}}\right)}. \qquad (35)$$

Thus, the number of fragments varies with the 5th power of the ratio $\Theta_{\rm subl}$ in the first case, but only with its cube in the second case.

Before we assess the extent of fragmentation in the period of time beginning in mid-November, we remark on one fundamental difference between Event 1 and Event 2. At the end of Event 1, the comet still retained about 85 percent of its water-ice reservoir available at the time of Mars encounter, whereas at the end of Event 2 the reservoir was nearly gone. This difference in the outcome suggests that after Event 1 the nucleus' debris included very large fragments (carrying the ice supplies), which, however, collapsed into much smaller, "dry" pieces during Event 2. Thus, Events 1 and 2 resemble, respectively, the first and the second extreme cases described above.

We now use Model G to assess the effects of fragmentation in Event 1 and 2. The other acceptable models, C–F and H, would provide fairly similar results. The nucleus' mass remaining after Event 1 is in Table 6 equivalent to an intact nucleus 0.62 km across. The ratio $\Theta_{\rm subl} = 19.5$, but an enhancement over the pre-outburst level of this ratio is estimated at only ∼17. A choice of, for example, 300 meters for the diameter of the largest fragment requires $\Gamma_{\rm frg} \approx \frac{1}{2}$, which implies that the smallest fragments are ∼4 meters across and that $N_{\rm frg} \approx 80\,000$ from Eq. (34). This is a meaningful, even though crude, order-of-magnitude estimate, all that we are interested in.

The nucleus' mass, 0.06×10^{14} g, remaining after Event 2 (Model G) is equivalent to a nucleus 0.30 km across, and we estimate the corrected ratio at $\Theta_{\rm subl} \simeq 41$. In order to get the same dimensions of the smallest fragments as before, one needs to adopt $\Gamma_{\rm frg} \approx 0.35$, in which case the largest fragment is about 12 meters across and $N_{\rm frg} \approx 100\,000$ from Eq. (35), a truly cataclysmic event. For comparison, the mass of the sublimated water ice and ejected dust, integrated over the duration of Event 2, amounted to 0.36×10^{14} g, six times the mass in the cloud of remaining fragments. They were in the next few days after Event 2 subjected to ever increasing temperatures and therefore to further fragmentation, and also to sublimation, especially of sodium compounds.

The applied model could be refined in several ways, for example, by distinguishing between sublimating and "dry" fragments, by varying the dust-to-water sublimation rate ratio with time, etc. Such a refinement would, however, require a number of additional assumptions and/or unavailable parameters. Our aim has been not to describe the process of the comet's disintegration in detail, but, rather, to illustrate what information can be extracted by applying a basic sublimation model.

To summarize, we propose that the timeline of the disintegration of comet C/2012 S1 went like this: The cycle E was definitely over by November 12, 16 days before perihelion, when a relatively minor increase in the production of water occurred, a precursor to Event 1. The peak water production rate, 16 times the rate four days earlier, coincided with a peak on the light curve. The comet tapped a limited source of water, evidently from its interior, that had been unavailable before. To make that happen, the nucleus had to be subjected to major fragmentation. If the production rate went back to normal in a matter of a day or two, Event 1 might have had no major effect on the comet's health. Instead, several days later the water-production rate went up another factor of 3. The mass of the already fragmented nucleus was in this explosion, closely related to Event 2 on the light curve, shattered into an estimated hundred thousand or so boulders, none much larger than several meters across. A major difference between Events 1 and 2 was in the degree of retention of water ice supplies by sizable fragments: it was fairly high in Event 1 but close to nil in Event 2, indicating a failure of these fragments to survive this latter event. Even much smaller boulders were still falling apart as late as hours before perihelion, as shown by a fading narrow extension protruding from the head in a series of SOHO's C2 preperihelion images.

Some 3 days before perihelion came a dramatic drop in the production of gas, as already discussed in Sec. 2.2. Although this development has not as yet been independently confirmed, the available results appear to imply that the comet's reservoirs of ices, including water ice, were at this point nearly or completely exhausted. The comet *de facto* ceased to exist already at this time, but the debris continued to orbit the Sun. The loss of ices deprived the comet of gas-driven activity, but by now, less than 0.2 AU from the Sun, the sublimation rate of sodium from dust was still increasing. In the meantime, the process of cascading fragmentation continued. The sodium sublimation rate was increasing not only because of the growing temperature, but also due to continuing fragmentation that was multiplying the total cross-sectional area of the debris. The flare-up during Event 3 was probably brought about in this fashion, as the peak near 15 $R_\odot$ compares favorably with similar peaks for the Kreutz minicomets. Curdt et al. (2014) placed a dust-emission event at 10 $R_\odot$, based on their observations made with the SUMER spectrometer on board SOHO. The life or death by sublimation was for each dust particle decided by its perihelion distance. Images taken merely an hour or so before perihelion suggest that the most resistant component of the disrupted nucleus, boulder-sized fragments, were also succumbing to the hostile environment, as the thin extension which they populated and which pointed from the head in the direction of motion in earlier images, was fading rapidly. The process of cascading fragmentation continued down to about 5 $R_\odot$, as shown by evidence from early post-perihelion images on the ultimate termination of all activity 3.5 hours before perihelion (Sec. 3.9).

4.3. *Estimated Size of the Largest Surviving Fragments of the Nucleus*

The question of what are the comet's largest surviving fragments has two sides: active vs inert ones. Knight & Battams (2014) remarked that "any remaining active nucleus was <10 m in radius." Our conclusion that all activity ceased 3.5 hours before perihelion implies that *no active* fragment of the nucleus survived. Our argument is consistent with no detection of any trace of a tail made up of perihelion or post-perihelion ejecta in the HI1 imager and in the coronagraphs C2, C3, COR2-A, and COR2-B. It also fits Curdt et al.'s (2014) failure to find any Lyman-α emission less than 1 hour before perihelion.

The problem of the largest inert fragments is more difficult and an answer more uncertain. Knight & Battams (2014) argue that the "limiting magnitudes of the SOHO and STEREO telescopes do not set meaningful upper limits on any surviving inactive fragments." While this is true, our examination of the comet's post-perihelion light curve (Figures 3–5) and morphology of its nucleus' relics (Figures 10–14) offers an approximate solution, based on an indirect method.

A necessary prerequisite for this approach is a selection of a size-distribution function of surviving inert material. As in Sec. 4.2, we employ the law from Eq. (30), which now covers both the nucleus' fragments and dust ejecta. Integrating it again from a minimum particle diameter, $D_{\rm min}$, to the maximum diameter, $D_{\rm max}$, that we search for, we find the relationship between the total mass, $\mathcal{M}_{\rm surv}$, of surviving particulates and their total cross-sectional area, $X_{\rm surv}$, in the form

$$\mathcal{M}_{\rm surv} = \tfrac{2}{3}\rho_{\rm eff} X_{\rm surv} \sqrt{D_{\rm min} D_{\rm max}}, \qquad (36)$$

where $\rho_{\rm eff}$ is an effective bulk density of the fragments. If the bulk density is related to the fragment size via Eq. (21), a plausible approximation for $\rho_{\rm eff}$ is

$$\rho_{\rm eff} = \sqrt{\rho_{\rm min}\,\rho_{\rm max}}, \tag{37}$$

where $\rho_{\rm min}$ is the bulk density of the smallest fragments, whose diameter is $D_{\rm min}$, and $\rho_{\rm max}$ the bulk density of the largest fragments. The diameter of these largest fragments is equal

$$D_{\rm max} = \left(\frac{3\mathcal{M}_{\rm surv}}{2\rho_{\rm eff} X_{\rm surv}} \right)^2 \cdot D_{\rm min}^{-1}. \tag{38}$$

The cross-sectional area of surviving fragments of the nucleus can be estimated from an intrinsic brightness $\Im_{\rm surv}$ of the comet's rocky relics in early post-perihelion images measured in a large aperture. The most appropriate data are the apparent magnitudes published by Nakano (2013a) and plotted in Figures 3–5.

Figure 3 shows that up to at least Nakano's first data point, referring to November 29.38 UT, or 0.60 day after perihelion, the light curve follows essentially an inverse-square law of heliocentric distance, so that $\Im_{\rm surv}$ and the total cross-sectional area of the nucleus' relics are practically constant. From an apparent magnitude of +0.5 that the object had at that time according to Nakano (2013a) in a 27-arcmin aperture, it follows that after accounting for the effects of SOHO-centric distance and the phase angle, $H_\Delta = +1.3$. From Eq. (1) with $r = 0.0681$ AU we obtain $\Im = 0.140$ and from Eq. (2) $X_{\rm surv} = 5 \times 10^4$ km^2, assuming the cloud was optically thin. Furthermore, the calculations show that the smallest particles that fitted a 27-arcmin aperture at the time had $\beta_{\rm min} = 0.052$ along the cloud's leading boundary and 0.055 along its trailing boundary (cf. Figure 13 for the object's appearance 2 hours later). On the average, these radiation-pressure accelerations indicate that $D_{\rm min} \simeq 11$ microns and $\rho_{\rm min} \simeq 1.9$ g cm^{-3}. The largest fragments should according to Eq. (21) have $\rho_{\rm max}$ close to 0.4 g cm^{-3}, so that $\rho_{\rm eff} \simeq 0.9$ g cm^{-3}.

The mass $\mathcal{M}_{\rm surv}$ of the surviving debris in the 27-arcmin aperture can be estimated only very approximately. Our guess for a crude upper limit is 5×10^{13} g, from Model G in Table 6, equal to the nucleus' mass just before Event 1. However, since much of that mass sublimated near perihelion (Sec. 4.1), a tighter estimate should be closer to 5×10^{12} g or less. Inserted with the other numbers into Eq. (38), the two mass limits lead to, respectively, $D_{\rm max} \ll 0.25$ m and $D_{\rm max} < 0.25$ cm. We thus find that the most sizable surviving inert fragments of the nucleus were unlikely to be larger than pebbles and may have been just subcentimeter-sized grains. The comet's disintegration was apparently quite complete, with no boulders left intact.

5. SUBLIMATION OF DUST IN THE STREAMER

In Sec. 3.2 we briefly investigated the nature of the sharp, narrow dust streamer, noting that a typical grain size was in the millimeter range and larger and that the release of grains from the nucleus dated back to the times when the comet was very far from the Sun. Because of the crowding of synchrones on top of each other, the times of release could not be determined with any degree of accuracy from the measured position angles.

Table 7
MEASUREMENTS OF STREAMER'S DISCONNECTION IN IMAGES TAKEN WITH THE C2 CORONAGRAPH.

Time of imaging		Streamer's tip		
2013 Nov. (UT)	relative to perihelion	separation from head	position angle	separation from Sun
28.654	$t_\pi - 3.00$ hr	0°.71	253°	1°.88
28.660	$t_\pi - 2.84$ hr	0.76	252	1.89
28.669	$t_\pi - 2.65$ hr	0.88	252	1.92
28.675	$t_\pi - 2.50$ hr	0.94	251	1.92
28.683	$t_\pi - 2.30$ hr	1.01	251	1.91
28.692	$t_\pi - 2.10$ hr	1.06	250	1.88
28.700	$t_\pi - 1.90$ hr	1.22	250	1.95
28.708	$t_\pi - 1.70$ hr	1.28	249	1.93
28.717	$t_\pi - 1.50$ hr	1.38	249	1.94
28.725	$t_\pi - 1.30$ hr	1.47	248	1.94
28.825	$t_\pi + 1.10$ hr	2.10	232	1.48
28.842	$t_\pi + 1.52$ hr	2.26	229	1.48
28.858	$t_\pi + 1.90$ hr	2.40	227	1.48
28.884	$t_\pi + 2.52$ hr	2.63	225	1.52
28.908	$t_\pi + 3.10$ hr	2.77	222	1.49

The streamer's disconnection from the head and its likely physical trigger — dust-grain sublimation near the Sun — were already mentioned in Sec. 3.2. In the following we describe our measurements of the point of disconnection in a number of images and our investigation of the phenomenon.

5.1. *Measurement of the Streamer's Disconnection in Images Taken with the C2 Coronagraph*

Even though the gap between the comet's head and streamer appears at first sight to end abruptly, inspection under magnification shows that there in fact is a steep but smooth transition. Measurements of the streamer's point of disconnection are therefore affected by errors that depend on the measurer's perception and judgment.

Because of the large pixel size (56 arcsec) of the C3 coronagraph, our measurements were limited to images taken with the C2 coronagraph. The results, presented in Table 7, show that most data points come from the preperihelion images in which the streamer was much brighter. Only every second image showing the disconnection point was measured in the post-perihelion images (in which however the streamer itself did not yet pass perihelion). The strong tendency for the disconnection point to stay at the same angular distance from the Sun is clearly demonstrated; errors of measurement are estimated at less than ±0°.1. Surprisingly, however, this critical distance differs in the pre- and post-perihelion images, amounting to, on the average, 1°.92 ± 0°.03 and 1°.49 ± 0°.02, respectively, This difference cannot be due to errors of measurement. Next, we develop and apply a sublimation model in an effort to estimate the thermophysical properties of the dust in the streamer.

5.2. *Sublimation Rate and Its Integrated Effect*

The streamer's termination on its sunward side allows one to estimate the sublimation heat of the material that made up the streamer and thus to confirm or refute the preliminary conclusion that water-ice grains could not be involved (Sekanina 2013c; also Sec. 3.2).

For a dust grain located at the point of disconnection of the streamer, the radius $a_{\rm rls}$ at the time $t_{\rm rls}$ of its release from the comet should equal a linear loss rate by sublimation, $da_{\rm subl}/dt$, integrated over the period of time from $t_{\rm rls}$ to the time of the grain's complete sublimation, $t_{\rm subl}$:

$$\Delta a_{\rm subl} = a_{\rm rls} = \int_{t_{\rm rls}}^{t_{\rm subl}} \frac{da_{\rm subl}}{dt}\, dt. \tag{39}$$

The loss rate of a grain's radius by sublimation is a function of the equilibrium temperature T and can be written in terms of the mass sublimation rate per unit area, $d\mathcal{Z}_{\rm subl}(T)/dt$, and the grain's bulk density, ρ,

$$\frac{da_{\rm subl}}{dt} = \frac{1}{\rho}\frac{d}{dt}\mathcal{Z}_{\rm subl}(T), \tag{40}$$

where

$$\frac{d}{dt}\mathcal{Z}_{\rm subl}(T) = \wp\sqrt{\frac{\mu}{2\pi\epsilon\Re T}}, \tag{41}$$

with $\Re$ being the gas constant (in cal mol^{-1}K^{-1}), a conversion factor $\epsilon = 4.1854\times10^7$ erg cal^{-1}, μ the molar weight (in g mol^{-1}), and $\wp$ the vapor pressure of the sublimating material (in dyn cm^{-2}), for which we write

$$\wp = \Lambda\exp\left(-\frac{L}{\Re T}\right). \tag{42}$$

In this expression L is the latent heat of sublimation of the material (in cal mol^{-1}). The coefficient Λ (in dyn cm^{-2}) is calculated from an approximate formula

$$\Lambda = \exp\left(22.105 + 0.956\times10^{-4}L\right). \tag{43}$$

Inserting from (40), (41), and (42) into (39), and replacing, as a variable, time t with heliocentric distance r, we find with a parabolic approximation and neglect of radiation pressure effects (because only large dust is involved), for the grain's radius (in cm) that sublimated away

$$\Delta a_{\rm subl} = C_0\int_{r_{\rm subl}}^{r_{\rm rls}} r^{\frac{1}{2}}\left(1-\frac{q}{r}\right)^{-\frac{1}{2}} T^{-\frac{1}{2}}\exp\left(-\frac{L}{\Re T}\right) dr, \tag{44}$$

where q is the perihelion distance (in AU) of the grain's orbit, the temperature is a function of heliocentric distance, $r_{\rm subl} = r(t_{\rm subl})$, $r_{\rm rls} = r(t_{\rm rls})$,

$$C_0 = \frac{\Lambda\sigma}{2k_{\rm G}\rho}\sqrt{\frac{\mu}{\pi\epsilon\Re}}, \tag{45}$$

$k_{\rm G} = 0.0172021$ AU$^{\frac{3}{2}}$ day^{-1}, and σ is a conversion factor, $\sigma = 0.864\times10^5$ s day^{-1}.

In general, the equilibrium temperature $T(r)$ of a dust grain of radius a in the radiation field of the Sun is derived from the balance between the solar energy absorbed and the energy reradiated at the given heliocentric distance r (e.g., Sekanina et al. 2001):

$$\frac{\pi a^2}{r^2}\int_0^\infty \mathcal{Q}_{\rm abs}(a,\lambda)S_0(\lambda)d\lambda = 4\pi a^2\int_0^\infty \mathcal{Q}_{\rm abs}(a,\lambda)\pi\mathcal{B}_\lambda(T)d\lambda, \tag{46}$$

where the integration is carried out over all wavelengths λ, $\mathcal{Q}_{\rm abs}(a,\lambda)$ in the grain's absorption efficiency at λ, $S_0(\lambda)$ is the solar flux at 1 AU, and $\pi\mathcal{B}_\lambda(T)$ is the Planck function. Because we deal with grains much larger than the wavelength, $\mathcal{Q}_{\rm abs}$ is practically constant (e.g., van de Hulst 1957), so that Eq. (46) becomes independent of the particle's cross-sectional area for absorption, $\pi a^2\mathcal{Q}_{\rm abs}$. The integral on the right side is proportional to T^4 and

$$T(r) = T_0\sqrt{r_0/r}, \tag{47}$$

where $r_0 = 1$ AU and $T_0 = 280$ K is a blackbody approximation. However, because of the particle's sublimation, only part of the absorbed solar radiation is spent on the reradiation of the energy and the temperature could increase with decreasing heliocentric distance somewhat less steeply than indicated by Eq. (47). With this caveat in mind (see below), we nevertheless insert it into Eq. (44) and substitute $z = \sqrt{r/q}$. Recognizing that substantial particle sublimation occurs only near $t_{\rm subl}$ and that therefore $r_{\rm rls}\to\infty$ represents an excellent approximation, the expression for $\Delta a_{\rm subl}$ becomes

$$\Delta a_{\rm subl} = C\int_{\sqrt{r_{\rm subl}/q}}^\infty z^{\frac{5}{2}}\left(1-\frac{1}{z^2}\right)^{-\frac{1}{2}}\exp(-Bz)\, dz, \tag{48}$$

where

$$C = 2C_0T_0^{-\frac{1}{2}}r_0^{-\frac{1}{4}}q^{\frac{7}{4}} \tag{49}$$

and

$$B = \frac{L}{\Re T_0}\sqrt{\frac{q}{r_0}}. \tag{50}$$

Equation (48) can easily be integrated numerically, after substituting a new variable, $\zeta = 1/z$,

$$\Delta a_{\rm subl} = C\int_0^{\sqrt{q/r_{\rm subl}}}\zeta^{-\frac{9}{2}}\left(1-\zeta^2\right)^{-\frac{1}{2}}\exp\left(-\frac{B}{\zeta}\right)d\zeta. \tag{51}$$

As a check, an approximate solution exists in closed form. To the extent that the term $1/z^2$ in Eq. (48) can be neglected, $[1-(1/z^2)]^{-\frac{1}{2}}\approx 1$, the integral becomes an incomplete Gamma function $\Gamma(h,x)$,

$$\int_{\sqrt{r_{\rm subl}/q}}^\infty z^{\frac{5}{2}}\left(1-\frac{1}{z^2}\right)^{-\frac{1}{2}}\exp\left(-Bz\right)dz \approx \int_{\sqrt{r_{\rm subl}/q}}^\infty z^{\frac{5}{2}}\exp\left(-Bz\right)dz = B^{-\frac{7}{2}}\,\Gamma\left(\frac{7}{2}, B\sqrt{\frac{r_{\rm subl}}{q}}\right). \tag{52}$$

Since for $h > 3$

$$\Gamma(h,x) = (h-3)(h-2)(h-1)\Gamma(h-3,x) + x^{h-1}e^{-x}\left[1+\frac{h-1}{x}+\frac{(h-2)(h-1)}{x^2}\right] \tag{53}$$

and

$$\Gamma(\tfrac{1}{2},x) = \sqrt{\pi}\left[1-\mathrm{erf}(\sqrt{x})\right], \tag{54}$$

the final form of an approximate solution to Eq. (48) in close form is

$$\Delta a_{\rm subl} = \frac{\Lambda\sigma}{k_{\rm G}\rho}\sqrt{\frac{\mu}{\pi\epsilon\Re T_0}}\left(\frac{L}{\Re T_0}\right)^{-\frac{7}{2}}r_0^{\frac{3}{2}}\left\{\tfrac{15}{8}\sqrt{\pi}\left[1-\mathrm{erf}\left(\sqrt{b}\right)\right] + b^{\frac{5}{2}}\exp(-b)\left[1+\frac{5}{2b}+\frac{15}{4b^2}\right]\right\}, \tag{55}$$

Table 8

Dust Grain Sublimation Parameters for Streamer in Images Taken witth the C2 Coronagraph.

Time of imaging 2013 Nov. (UT)	Sublimation distance from Sun, $r_{\rm subl}$ ($R_\odot$)	Sublimation parameters of dust grains for a preperihelion time of release, $t_{\rm rls}$, from the comet											
		at 10 AU from Sun			at 20 AU from Sun			at 50 AU from Sun			at 100 AU from Sun		
		Grain acceleration β	Grain diam. (cm)	Sublimation heat (cal mol^{-1})	Grain acceleration β	Grain diam. (cm)	Sublimation heat (cal mol^{-1})	Grain acceleration β	Grain diam. (cm)	Sublimation heat (cal mol^{-1})	Grain acceleration β	Grain diam. (cm)	Sublimation heat (cal mol^{-1})
28.654	6.91	0.000510	0.47	90 100	0.000181	1.45	85 800	0.0000459	6.00	80 100	0.0000163	17.3	75 800
28.660	6.89	0.000541	0.44	90 500	0.000192	1.36	86 200	0.0000487	5.65	80 500	0.0000172	16.3	76 100
28.669	7.03	0.000623	0.38	90 000	0.000221	1.17	85 700	0.0000561	4.89	80 000	0.0000199	14.1	75 800
28.675	7.04	0.000660	0.36	90 100	0.000234	1.10	85 900	0.0000594	4.61	80 200	0.0000210	13.3	75 900
28.683	7.01	0.000700	0.33	90 600	0.000249	1.03	86 300	0.0000630	4.34	80 700	0.0000223	12.5	76 400
28.692	6.90	0.000722	0.32	91 700	0.000256	1.00	87 300	0.0000650	4.20	81 600	0.0000230	12.1	77 300
28.700	7.15	0.000831	0.27	90 200	0.000295	0.86	86 000	0.0000748	3.63	80 400	0.0000265	10.5	76 200
28.708	7.06	0.000857	0.26	91 100	0.000304	0.83	86 800	0.0000771	3.52	81 100	0.0000273	10.2	76 900
28.717	7.10	0.000913	0.25	91 000	0.000324	0.78	86 700	0.0000822	3.30	81 100	0.0000291	9.56	76 900
28.725	7.09	0.000960	0.23	91 300	0.000341	0.74	87 000	0.0000865	3.13	81 400	0.0000306	9.08	77 100
28.825	5.51	0.001139	0.19	108 400	0.000405	0.61	103 300	0.0001026	2.62	96 600	0.0000363	7.63	91 500
28.842	5.49	0.001236	0.17	109 100	0.000439	0.56	104 000	0.0001113	2.41	97 200	0.0000394	7.02	92 100
28.858	5.51	0.001330	0.16	109 200	0.000472	0.52	104 100	0.0001198	2.23	97 300	0.0000424	6.51	92 200
28.884	5.62	0.001505	0.14	108 400	0.000535	0.45	103 300	0.0001356	1.96	96 700	0.0000480	5.73	91 600
28.908	5.56	0.001627	0.13	109 500	0.000578	0.41	104 400	0.0001466	1.80	97 700	0.0000519	5.29	92 600

where

$$b = \frac{L}{\Re T_0}\sqrt{\frac{r_{\rm subl}}{r_0}} = B\sqrt{\frac{r_{\rm subl}}{q}}. \qquad (56)$$

Equations (51) and (55) represent a constraint on the relevant properties of grains: $\Delta a_{\rm subl}$, ρ, μ, $r_{\rm subl}$, and L. Next, we investigate this constraint for the material that made up the streamer of comet C/2012 S1.

5.3. *Determination of Heliocentric Distance at Point of Disconnection and Range of Sublimation Heat for Dust Grains in the Streamer*

In Table 7 we summarize the angular distances of the measured points of disconnection (complete grain sublimation) in the streamer. Viewed from SOHO, the angles 1°.5 and 1°.9 correspond, at its distance from the Sun, to heliocentric distances of ∼5.5 and ∼7.0 $R_\odot$, respectively.

The discrete distances of the points of disconnection require an explanation. The streamer's fainter part, terminating at 5.5 $R_\odot$ in the post-perihelion images, should also show up in the preperihelion images. Unfortunately, in projection it overlaps the northern boundary of the tail from Event 2 and is not recognized as a separate feature. The positions of the point of disconnection that terminates at 7.0 $R_\odot$ were determined from the preperihelion images despite the overlap only thanks to the exceptional brightness (Figure 8). By contrast, in the post-perihelion images the faint part of the streamer and the tail from Event 2 clearly separate from one another. The point of disconnection at 7.0 $R_\odot$ is undetected in these images either because it is too far to fit in or because it is no longer bright enough (in part because of backscatter). This interplay of coincidences suggests that the streamer consists of at least two components. It is in fact likely that there are quite a few more than two overlapping components — or separate "substreamers" — whose points of disconnection are located between 5.5 and 7.0 $R_\odot$, but, except for the two, they are too faint to detect.

Grains in the streamer are sorted by distance from the head so that, for a given time of release from the comet and near-zero release velocities, the smaller the acceleration by solar radiation pressure, β, the closer to the head they are. Thus, a proper approach is to determine β that the grains at the point of disconnection were subjected to in each measured image by applying the equations of grain motion. This solution also pinpoints the position of the grains in space, thus furnishing the heliocentric distance at complete sublimation, $r_{\rm subl}$.

A complication is that the time of release or the equivalent heliocentric distance cannot for the streamer be unequivocally determined (Sec. 3.2); we carried out the computations by assuming the grain release at 10, 20, 50, and 100 AU from the Sun (Table 8). The knowledge of β at a particular distance of the point of disconnection then provides us with a good estimate for the grains' size and therefore for $\Delta a_{\rm subl}$ in Eqs. (51) and (55). With the scattering efficiency for radiation pressure assumed to be unity (an excellent approximation for very large grains; e.g., van de Hulst 1957), the acceleration β (in units of the Sun's gravitational acceleration equal to 0.593 cm s^{-2} at 1 AU), exerted by solar radiation pressure on a grain whose diameter is δ (in microns) and bulk density ρ (in g cm^{-3}), is expressed by a well-known relation (e.g., Sekanina et al. 2001),

$$\beta(\rho, \delta) = \frac{1.148}{\rho\,\delta}, \qquad (57)$$

which is to be solved together with Eq. (21), the adopted relationship between the grain's bulk density and size.

From the described procedure we have so far been able to gain information on three of the five grain-dependent quantities that enter Eqs. (51) or (55). The only two remaining unknowns are the molar weight μ and the sublimation heat L. The effect of μ on L in the range of our solutions is shown below to be small, on the order of ±1–2 percent for μ varying by a factor of two or so.

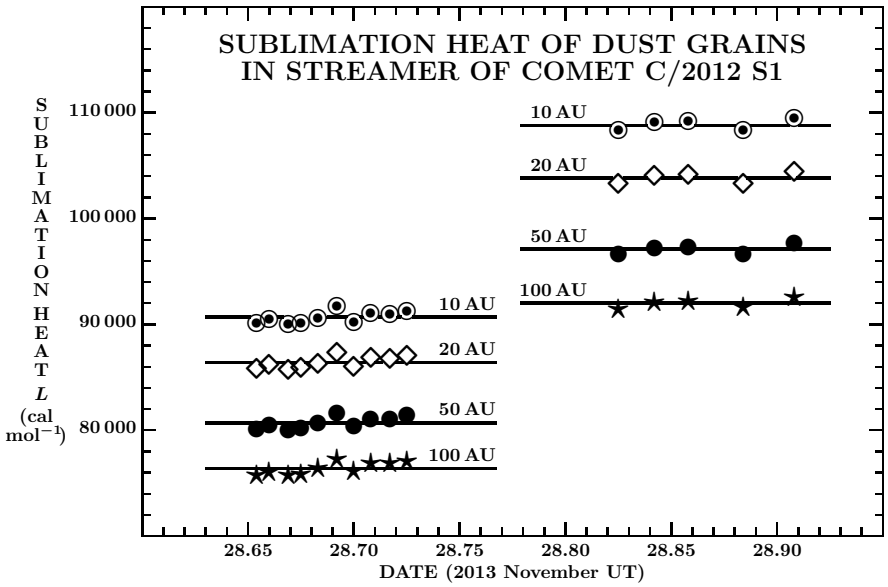

Figure 16. Sublimation heat L of dust grains in the streamer of comet C/2012 S1 derived from the heliocentric distance $r_{\rm subl}$ of the streamer's point of disconnecton in 15 images taken with the C2 coronagraph on board SOHO. Different symbols are used to plot the results for each of the four assumed heliocentric distances at grain release from the comet: 10, 20, 50, and 100 AU. The distance of complete sublimation, $r_{\rm subl}$, averaged 7.02 $R_\odot$ for the 10 preperihelion images on the left, but 5.54 $R_\odot$ for the five post-perihelion images. This difference is responsible for the systematic shift in the range of sublimation heat established from the pre- and post-perihelion images. Note that the sublimation heat for grains released at 10 AU, as derived from the preperihelion images, is very close to the sublimation heat for very large grains (pebbles) released at 100 AU, as derived from the post-perihelion images.

The sublimation heat L of the dust in the streamer is by far the most important quantity. We are now ready to use Eq. (51) [with Eq. (55) as a check] to determine L from the perceived sublimation effect that causes the streamer's disconnection.

Our nominal runs in Table 8 used a generic molar weight of 100 g mol^{-1}. Not listed is the bulk density, which was always between 0.4 and 0.6 g cm^{-3} and can readily be ascertained from Eq. (21). The numbers are from the numerical integrations of Eq. (51); the approximate, close-form formula gave, as expected, consistently smaller values for $\Delta a_{\rm subl}$, mostly between 75 and 80 percent of the accurate value, thus fulfilling its task.

All measured preperihelion images resulted in nearly the same value for the sublimation heat, which depends significantly on the adopted heliocentric distance $r_{\rm rls}$ at the time of dust release from the comet and varies between about 91 000 cal mol^{-1} for 10 AU from the Sun to 76 000 cal mol^{-1} for 100 AU from the Sun. The sublimated grain diameter ialso depends a little on the time of imaging, as the critical sublimation distance $r_{\rm subl}$ is reached by grains of gradually decreasing size. During the 1.7 hours spanned by the preperihleion images, the diameter of the sublimated grains dropped by a factor of ∼2, amounting to a few millimeters for the assumed release distance of 10 AU but ∼10 cm or more for 100 AU.

The smaller set of post-perihelion images yielded similarly consistent results. Because of the smaller heliocentric distances $r_{\rm subl}$, the sublimation heat came out higher, between 109 000 cal mol^{-1} for the release distance of 10 AU and 92 000 cal mol^{-1} for 100 AU. During the 2 hours spanned, the diameter of the sublimated grains dropped by a factor of only 1.5 or so, varying from 1–2 mm for the release distance of 10 AU to as much as several centimeters for 100 AU.

Because the size of the sublimated away grains was decreasing with the time of imaging, the heliocentric distance at complete grain sublimation, $r_{\rm subl}$, should be slightly increasing with time in Table 8. In spite of some noise, a trend like this is indeed apparent in both the preperihelion and post-perihelion sets, and is also confirmed by the correlation coefficients, 0.70 and 0.71, respectively, even though the average rates, 2.6 ± 0.9 $R_\odot$ day^{-1} from the preperihelion images and 1.1 ± 0.6 $R_\odot$ day^{-1} from the post-perihelion images, are poorly determined. The respective average values of $r_{\rm subl}$ are 7.02 ± 0.09 $R_\odot$ and 5.54 ± 0.05 $R_\odot$, with the errors much smaller than the difference, 1.48 ± 0.10 $R_\odot$.

The values of the sublimation heat derived from the 15 images taken with the C2 coronagraph are plotted in Figure 16. To the extent that the range of assumed heliocentric distances at the times of grain release from the comet cover all realistic possibilities, one can conclude from the figure that the sublimation heat of the grains that made up the streamer was between 75 000 and 110 000 cal mol^{-1}. This is a highly refractory material, comparable, for example, to atomic iron (for which $L = 88\,100$ cal mol^{-1} in a temperature range of 1730–3130 K or a vapor-pressure range of 1–10^5 Pa),[11] but not as refractory as silicates (120 000–130 000 cal mol^{-1}). One can definitely exclude not only water ice, but also such substances as atomic sodium (25 000 cal mol^{-1}) and other similar metals that are much less refractory than the above lower limit on L suggests. As remarked, the choice of a molar weight has almost no effect on the value of the sublimation heat; replacing 100 g mol^{-1} with, for example, 50 g mol^{-1} leads to L smaller by 1200–1700 cal mol^{-1}.

[11] See, for example, `http://en.wikipedia.org/wiki/Iron`.

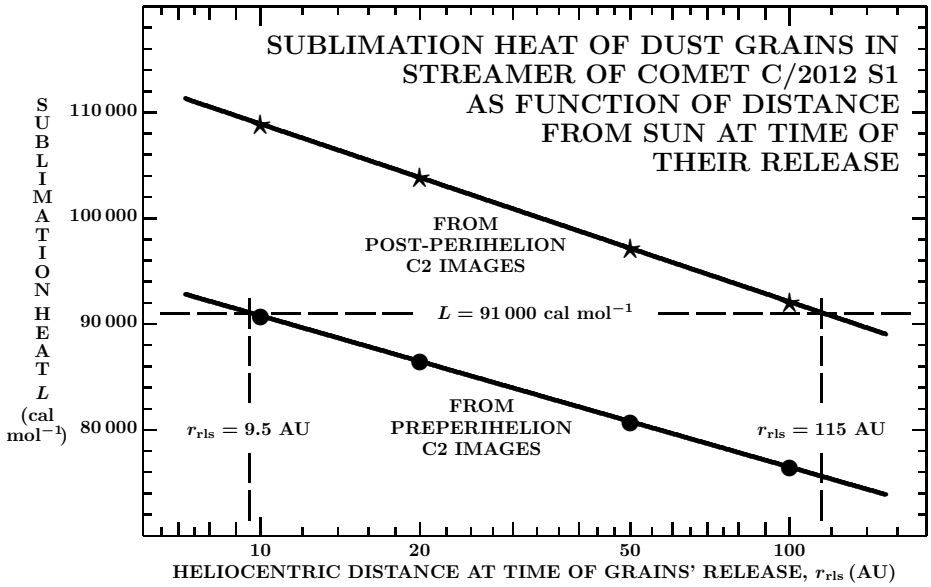
SUBLIMATION HEAT OF DUST GRAINS IN STREAMER OF COMET C/2012 S1 AS FUNCTION OF DISTANCE FROM SUN AT TIME OF THEIR RELEASE
SUBLIMATION HEAT L (cal mol−1)
110 000
100 000
90 000
80 000
FROM POST-PERIHELION C2 IMAGES
L = 91 000 cal mol−1
FROM PREPERIHELION C2 IMAGES
rrls = 9.5 AU
rrls = 115 AU
10
20
50
100
HELIOCENTRIC DISTANCE AT TIME OF GRAINS' RELEASE, rrls (AU)

Figure 17. Sublimation heat L of dust grains in the streamer plotted against heliocentric distance $r_{\rm rls}$ at the time of their release. Based on the averaged data points from Figure 16, this plot displays an exponential dependence of the sublimation heat L on the distance $r_{\rm rls}$. Note that the slopes of the lines of sublimated grains in the preperihelion and post-perihelion images are not the same. A solution that satisfies the constraint of a constant sublimation heat is depicted by a dashed line parallel to the axis of abscissae. In an intriguing scenario, the presence of grains with diameters of 1 mm or so and released 9.5 AU from the Sun is suggested to explain the points of disconnection of the streamer in the preperihelion images, while the presence of pebbles several centimeters in diameter and released 115 AU from the Sun is required to explain the points of disconnection of the streamer in the post-perihelion images. The sublimation heat of the streamer's material is approximately 90 000 cal mol^{-1}, close to that of atomic iron.

The results in Table 8 allow one to plot the average sublimation heat of material in the streamer as a function of heliocentric distance, $r_{\rm rls}$, at the time of release from the nucleus, separately from the preperihelion and post-perihelion images (Figure 17). Since $r_{\rm rls}$ correlates closely with the grain diameter, the difference between the two exponential relationships can be attributed either to differences in the dimensions of released grains of essentially the same material, or to different sublimation heats and, thus, to different materials. The first option sounds more credible, because particle dimensions in comets are known to vary widely; the other option appears factitious and is more difficult to justify.

Accepting the first option, the sublimation heat of the material that made up the streamer is the same for both the preperihelion and post-perihelion images. This constraint leads to an intriguing result: the solutions imply that a likely sublimation heat of the streamer's material amounts to about 90 000 cal mol^{-1}. For a sublimation heat significantly lower, the positions of the point of disconnection in the post-perihelion images would require boulder-sized or larger fragments to have been released at enormous heliocentric distances, on the order of many hundreds or even thousands AU; for a sublimation heat significantly higher, the positions of the point of disconnection in the preperihelion images would require that the heliocentric distances at release be too small, inconsistent with the arguments presented in Sec. 3.2. In a narrow range of acceptable scenarios, the grains that completely sublimated away in the preperihelion images were released from the comet near 10 AU from the Sun and were initially close to 1 mm across, while the grains that completely sublimated away in the post-perihelion images were released near 100 AU from the Sun and were initially more than 10 times larger, several centimeters across. One such solution is depicted in Figure 17, with two clouds of grains of a sublimation heat of 91 000 cal mol^{-1} released at, respectively, 9.5 AU and 115 AU. Returning to Eq. (47), we find that even at a heliocentric distance as small as 5.5 $R_\odot$, more than 98 percent of the solar radiation absorbed by a dust particle made up of a material of this heat of sublimation is spent on thermal reradiation; at larger distances the fraction is greater still. This means that Eq. (47) approximates the grain's equilibrium temperature quite satisfactorily and Eq. (51) is appropriate for determining the sublimation effect on dust in the range of relevant dimensions.

5.4. *Activity of Comet C/2012 S1 Far from the Sun*

Even though the presented solution is the best apparent choice given the options offered by Figure 17, one should ask whether this dust particle sublimation model can be defended on physical grounds. Reviewing briefly the past work on cometary activity at large heliocentric distances, we note that, on the observational side, the appearance of dynamically new comets has provided evidence of preperihelion activity at distances of more than 10 AU. One long-known source of this information is the orientation of narrow dust tails of such comets with perihelia beyond 2–3 AU (Sekanina 1975).[12] Later, the same conclusion was reached based, among others, on orbital evidence (Marsden et al. 1978), on an extent of sources of activity on the nucleus (Rickman et al. 1991), and on the depletion of carbon-chain molecules (A'Hearn et al. 1995). Fairly recently, dynamically new comets

[12] Strangely, major deviations in the orientation of these tails (mistaken for plasma tails) from the antisolar direction were in the 1960s thought to offer evidence, beyond 2 AU from the Sun, for now a long-abandoned hypothesis of a solar "breeze" (Chamberlain 1960, 1961).

have been directly observed as active objects displaying their tails at distances of more than 10 AU from the Sun preperihelion (Meech et al. 2009).

On the theoretical side, a consensus has been emerging over the past four decades (e.g., Patashnick et al. 1974, Klinger 1980, Smoluchowski 1981, Herman & Podolak 1985, Prialnik 1992, 2006, Jenniskens & Blake 1996, Enzian et al. 1998, Korsun & Chörny 2003, González et al. 2008) that a major source of cometary activity far from the Sun are processes in amorphous water ice that must exist in comets if ice deposition had taken place under the conditions of very low temperatures and low pressures.

The progress in the understanding of the physical processes involving amorphous water ice at low temperatures has been accelerated by numerous laboratory experiments. A typical procedure is to deposit water vapor in a vacuum chamber on a receptor cooled usually to 10–20 K; guest gases, such as CO, CO_2, CH_4, NH_3, N_2, etc., are co-deposited either simultaneously or subsequently (e.g., Bar-Nun et al. 1985, 1987, Laufer et al. 1987, 2005, Schmitt & Klinger 1987, Schmitt et al. 1989, Ayotte et al. 2001). Large amounts of the guest gases get trapped in the pores of amorphous ice, with an excess, if any, freezing on the surface. Upon gradually warming up the receptor, it is observed that once the excess gas sublimates away from the surface, intense release of gas from within the ice begins at 35–37 K. This gas evacuates pore space in the ice by its slow annealing, a process that proceeds in the laboratory stepwise as long as the temperature keeps increasing, and still can continue at temperatures as high as 110 K. Release of icy grains was observed in laboratory experiments when gas was escaping at high rates. Meech et al. (2009) proposed that "gas release during the annealing process between ∼37 K and 120 K can account for the activity ... of comets at distances [at which the] temperature could not reach the ∼120 K phase transition temperature" of the ice. Besides, a transformation of two metastable phases takes place between 38 K and 68 K, from high-density to low-density amorphous ice (Jenniskens & Blake 1994), a transition that requires a higher activation energy than the annealing.

To the extent that the results of these laboratory experiments are applicable to dynamically new comets, such as C/2012 S1, they imply dust grains' release as soon as a temperature of $T_{\rm anneal} \simeq 37$ K has been reached at the nucleus' surface. This temperature refers to a heliocentric distance $r_{\rm anneal}$ given by

$$r_{\rm anneal} = \left(\frac{T_{\rm ref}}{T_{\rm anneal}} \right)^2, \tag{58}$$

where a reference temperature $T_{\rm ref}$ (at 1 AU from the Sun) depends on the insolation regime of the nucleus. The only relevant piece of information on C/2012 S1 that we are aware of is Li et al.'s (2014) finding that the nucleus always faced the Sun with one hemisphere until shortly before perihelion. This mimicks a case of nonrotating regime, so that $T_{\rm ref} \simeq 394$ K and

$$r_{\rm anneal} \simeq 113 \text{ AU}. \tag{59}$$

This heliocentric distance essentially coincides with $r_{\rm rls}$ found in Figure 17 for a sublimation heat of 91 000 cal mol^{-1} from the positions of the points of disconnection of the streamer in the post-perihelion images.

As the comet continued to approach the Sun and its surface temperature eventually exceeded 120 K, an exothermic transition from amorphous to crystalline (cubic) ice began to affect the balance of energy at the surface. Crystallization of the annealed, but still gas-laden, amorphous ice completed the evacuation of the remaining trapped gases and in the process of their release dust grains were again lifted along. Because the crystallization time varies with the temperature T exponentially, as $\exp(-\text{const}/T)$, there is no single temperature that defines the beginning of this process. However, the crystallization process was essentially over by the time the temperature reached ∼150 K, while the rate of trapped-gas release peaked close to 130 K or 135 K. Schmitt et al.'s (1989) results show that trapped CO_2 — next to CO of considerable interest — has a peak evacuation rate near 125 K. Writing the relation between the crystallization temperature $T_{\rm cryst}$ and the crystallization heliocentric distance $r_{\rm cryst}$ in a form analogous to Eq. (58) and taking $T_{\rm cryst} = 125-130$ K, we find

$$r_{\rm cryst} = 9.2-9.9 \text{ AU}, \tag{60}$$

comparable to $r_{\rm rls}$ in Figure 17 for a sublimation heat of 91 000 cal mol^{-1} derived from the positions of the point of disconnection of the streamer in the preperihelion images.

To summarize, we find a remarkably consistent parallelism between the dust particle sublimation model for the streamer of comet C/2012 S1, on the one hand, and the existing consensus on the preperihelion activity of dynamically new comets at very large heliocentric distances, on the other hand. Specifically, we correlate a dust release event just beyond ∼100 AU with the initial annealing of amorphous water ice at 37 K and an event near 10 AU with the exothermic phase change from amorphous to cubic ice at 125–130 K; the released refractory material, pebble-sized in the first case and millimeter-sized in the second case, is found to possess thermal properties that are consistent with the heat of sublimation of ∼91 000 cal mol^{-1}. Cursory inspection suggests that the amount of the debris released during the explosive crystallization of amorphous ice exceeded that released during the annealing, a tentative conclusion that is qualitatively consistent with laboratory experiments (Meech et al. 2009). We do not rule out the existence of overlapping "substreamers" as products of additional, followup annealing events between 100 and 10 AU.

6. ORBITAL MODELING AND ANALYSIS

Given the violent events to which the comet was exposed, it is to be expected that the orbital motion was affected as well and that its analysis should contribute to the overall understanding of the comet's response.

The *Minor Planet Center* (MPC) published a number of successively improved gravitational solutions that eventually covered an orbital arc from the earliest prediscovery observations on 2011 September 30 to 2013 November 20 (Williams 2013a), merely two days short of the time of the comet's last ground-based astrometry. Only at that point were further gravitational runs abandoned (Williams 2013b). As a rule, the positional residuals from individual observations were not published, and it has been impossible to make any judgment on the quality of fit and the presence of systematic trends from

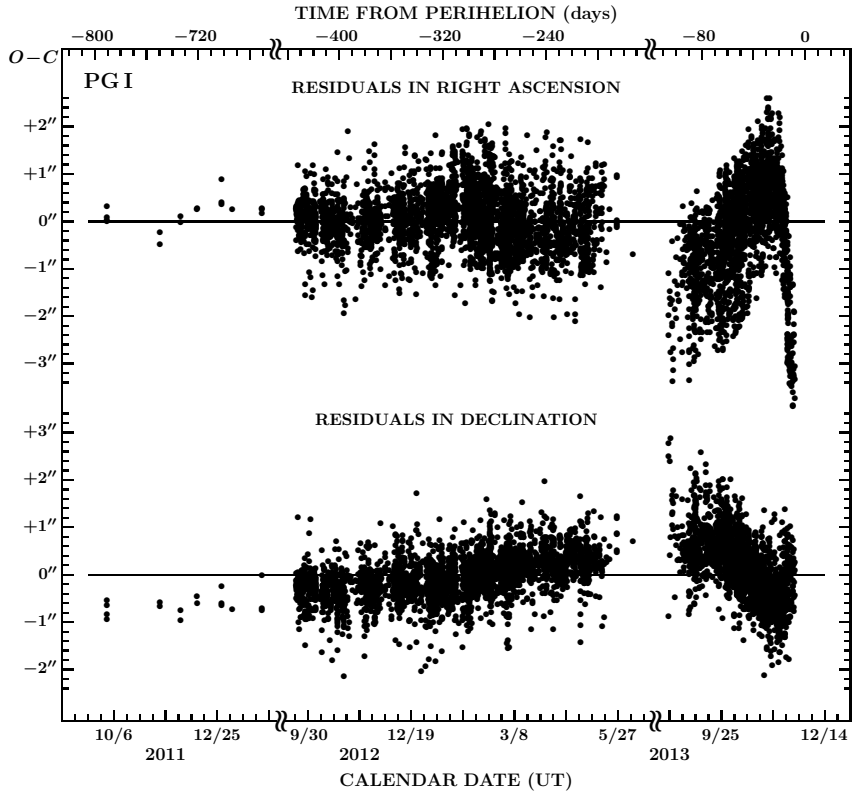

Figure 18. Distribution of residuals for 6166 observations from the gravitational solution PG I. Very strong trends are apparent in either coordinate after conjunction with the Sun; a continuous trend is also seen in declination throughout the pre-conjunction period of time.

a mean residual of ±0″.6, which depends primarily on an arbitrarily chosen cutoff for rejecting inaccurate observations. An exception was the first nongravitational solution (Williams 2013b), for which individual residuals were published, including those of discarded observations. Cursory inspection shows that, even though the value of the resulting nongravitational parameter was one of the largest on record, systematic trends in the residuals were still present, especially at both ends of the fitted orbital arc. This finding suggests that any gravitational solutions may have been unsatisfactory long before the second half of November of 2013.

Our objective is to understand effects of the comet's physical state on its orbital motion. All computations were carried out by the second author with an *EXORB7* orbit-determination code, developed by A. Vitagliano. The perturbations by the eight planets, Pluto, and the three most massive asteroids are included and the standard DE406 library used. Forced values of orbital elements and nongravitational parameters can be employed.

First, we considered the ground-based astrometry only (Secs. 6.1–6.4). After collecting 7770 positional observations of the comet from the MPC's observations database (see the reference to MPC in footnote 1), we first eliminated the 1099 that were listed twice, which left us with 6671 entries. Next, in preliminary runs we discarded all observations that left residuals greater than ±2″ from ad hoc osculating solutions that showed no trends in the residuals. We eventually ended up with a total of 6177 acceptable ground-based observations between 2011 September 30 and 2013 November 22, spanning 784 days. All observations were assigned the same weight.

Table 9
Summary of Purely Gravitational Solutions (PG) Derived for Comet C/2012 S1.

Solution	End date of used observations[a]	Number of observations	Mean residual	Systematic trends
PG I	2013 Nov. 20	6166	±0″.68	enormous
PG II	10	5941	±0.59	very strong
PG III	Oct. 30	5619	±0.56	strong
PG IV	15	5064	±0.54	moderate
PG V	Sept. 30	4579	±0.52	some in R.A.
PG VI	15	4238	±0.50	some in R.A.
PG VII	Aug. 31	3978	±0.48	some in R.A.
PG VIII	June 8	3923	±0.47	slight
PG IX	Jan. 31	1857	±0.43	nearly none

[a] Initial date was always 2011 September 30, the time of the earliest pre-discovery observation.

6.1. *Purely Gravitational Solutions (PG)*

We began with purely gravitational solutions. To examine the quality of fit they achieved, we linked all selected astrometric observations, starting with the earliest pre-discovery entries and ending with different dates in 2013 in the order of decreasing time span covered. The most important solutions among the ones we ran are summarized in Table 9.

The first gravitational solution, PG I, matching the time interval of the observations fitted by the MPC's last published gravitational solution (2011 September 30–2013 November 20; Williams 2013a), left a distribution of residuals presented in Figure 18. Considerable trends are apparent especially in right ascension in the

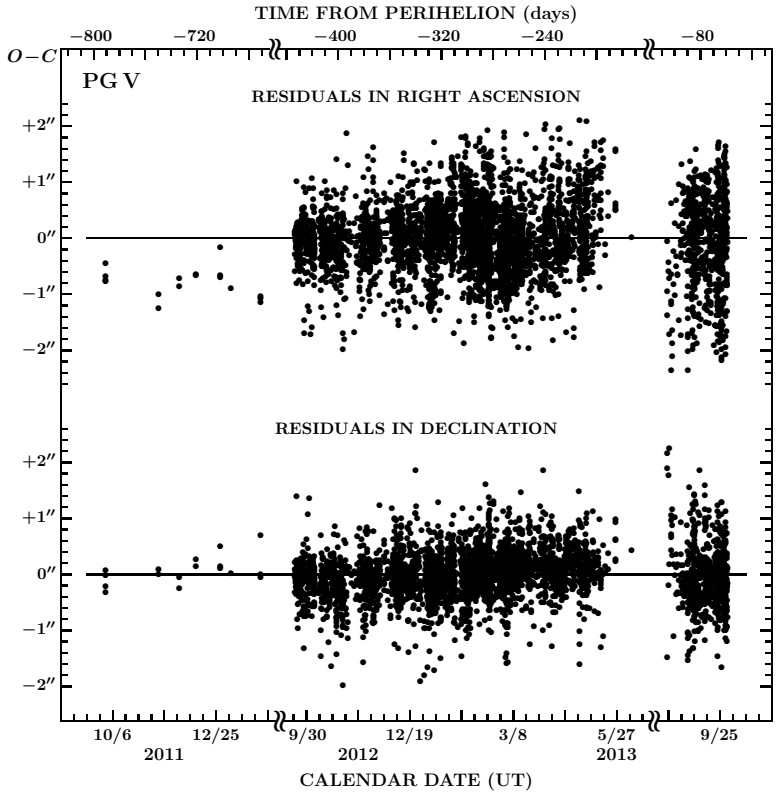

Figure 19. Distribution of residuals for 4579 observations from the gravitational solution PG V. Clear trends are apparent in right ascension among the pre-discovery observations and again near 100 days before perihelion.

period of time following the 2013 conjunction with the Sun, although the fit is poor at other times as well.

The last column of Table 9 indicates that as long as any post-conjunction observations were included (the solutions up to PG VII), the fit was, primarily in right ascension, never satisfactory. As an example, the residuals from the solution PG V are displayed in Figure 19. The residuals in R.A. from the pre-discovery, late pre-conjunction and early post-conjunction observations are unacceptable. The trend in the residuals in R.A. from pre-discovery observations was not completely rectified even by an improved solution PG VIII. To get a nearly-perfect fit by a gravitational solution, it was necessary to shorten the covered orbital arc to only about 16 months, terminating it at the end of January 2013, when the comet was some 4.9 AU from the Sun. The orbital elements from this solution, PG IX, are presented in Table 10 and the residuals are plotted in Figure 20. The residuals from the pre-discovery observations now show only a marginal trend in declination and none in R.A.

Table 10

Orbital Elements of Comet C/2012 S1 for the Period of 2011 September 30–2013 January 31 (Solution PG IX).

Epoch of osculation (TT)	2013 Nov 24.0
Time of perihelion, t_π (TT)	2013 Nov 28.7843 ± 0.0018
Argument of perihelion, ω	345°.5639 ± 0°.0001
Longitude of ascending node, Ω	295°.6547 ± 0°.0002
Orbital inclination, i	62°.3887 ± 0°.0012
Perihelion distance, q (AU)	0.01244418 ± 0.00000035
Orbital eccentricity, e	1.00000158 ± 0.00000008

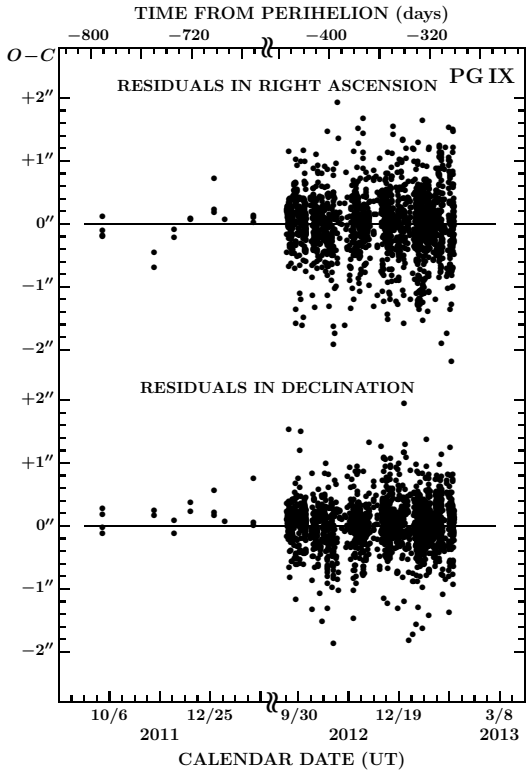

Figure 20. Distribution of residuals for 1857 observations from the gravitational solution PG IX. Practically no trends are apparent in either coordinate. This solution covers the longest observed orbital arc that can be fitted without use of nongravitational terms in the equations of motion.

Table 11

Summary of Standard Nongravitational Solutions (SN) for Comet C/2012 S1 and Parametric Values A_1, A_2, and A_3.

Solution	End date of observations employed[a]	Number of observations	Option	Mean residual	Parametric values (10^{-8} AU day^{-2}) A_1	A_2	A_3
SN I	2013 Nov. 22	6177	SN I_1	$\pm0''.56$	$+8.69 \pm 0.11$	...	...
			SN I_2	±0.56	$+8.06 \pm 0.12$	$+0.60 \pm 0.03$	...
			SN I_3	±0.55	$+10.82 \pm 0.34$	-0.54 ± 0.14	-1.89 ± 0.22
SN II	2013 Nov. 10	5941	SN II_1	±0.55	$+10.03 \pm 0.24$	...	...
			SN II_2	±0.55	$+9.41 \pm 0.24$	$+0.82 \pm 0.06$	...
			SN II_3	±0.55	$+9.24 \pm 0.39$	$+0.97 \pm 0.27$	$+0.26 \pm 0.46$
SN III	2013 Oct. 30	5619	SN III_1	±0.55	$+10.25 \pm 0.49$	...	...
			SN III_2	±0.54	$+9.54 \pm 0.49$	$+1.63 \pm 0.11$	...
			SN III_3	±0.54	$+10.01 \pm 0.50$	$+5.02 \pm 0.62$	$+5.9 \pm 1.1$
SN IV	2013 Oct. 15	5064	SN IV_1	±0.54	$+4.4 \pm 1.4$	...	...
			SN IV_2	±0.53	$+4.5 \pm 1.4$	$+4.66 \pm 0.36$	...
			SN IV_3	±0.53	$+11.4 \pm 3.9$	$+8.5 \pm 2.1$	$+6.7 \pm 3.5$
SN V	2013 Sept. 30	4579	SN V_1	±0.52	-10.0 ± 3.5	...	...
			SN V_2	±0.52	-6.8 ± 3.5	$+8.94 \pm 0.96$	...
			SN V_3	±0.51	-149 ± 22	-37.8 ± 7.0	-78 ± 12

[a] Initial date was always 2011 September 30, the time of the earliest pre-discovery observation.

The comet's original barycentric reciprocal semimajor axis, $(1/a_{\rm b})_{\rm orig}$, derived from this set of orbital elements, is equal to $+0.000\,035 \pm 0.000\,006$ AU^{-1}, within 2σ of an average perihelion-distance corrected value of $+0.000\,046$ AU^{-1} (Marsden et al. 1978), confirming that there is no doubt about C/2012 S1 being a dynamically new comet, arriving from the Oort Cloud.

In summary, purely gravitational solutions are generally found to fail fitting the orbital motion of comet C/2012 S1 except at heliocentric distances larger than ∼5 AU. We conclude that it is inappropriate to ignore the outgassing-driven nongravitational effects at smaller heliocentric distances and that their neglect at distances below 1.4 AU leads to strong systematic trends in the distribution of residuals.

6.2. *Standard Nongravitational Solutions (SN)*

To satisfy the need for incorporating nongravitational terms into the equations of motion, we turned to the standard 'Style II' formalism of Marsden et al. (1973). The applied dimensionless law $g_{\rm ice}(r)$ is based on a premise that a comet's nongravitational acceleration is driven by momentum transfer from the outgassing of water ice. This nongravitational law, a function of heliocentric distance r only and therefore symmetrical with respect to perihelion, is in Marsden et al.'s formalism expressed by an empirical formula,

$$g_{\rm ice}(r) = \alpha \left(\frac{r}{r_0}\right)^{-m} \left[1+\left(\frac{r}{r_0}\right)^{n}\right]^{-k}, \qquad (61)$$

where $r_0 = 2.808$ AU is a scaling heliocentric distance, at which the fraction of the solar energy spent in water-ice sublimation is about 0.023 times the fraction spent in reradiation of the surface. The values of the exponents are $m = 2.15$, $n = 5.093$, $nk = 23.5$, and $\alpha = 0.1113$ is a normalization coefficient that forces $g_{\rm ice}(1\,{\rm AU}) = 1$. For a low Bond albedo and unit emissivity, these constants apply to a so-called isothermal model, which averages the Sun's incident radiation over the surface of a spherical nucleus by assuming that the temperature does not vary from place to place. In reality, of course, the temperature does vary over the surface, but for the orbit-determination purposes the law from Eq. (61) has over the four decades since its inception in 1973 provided excellent service and still is employed worldwide nowadays.

The magnitude of the nongravitational acceleration at 1 AU from the Sun is given by the components of a right-handed coordinate system in three cardinal directions tied to the orbital plane: a radial component A_1, pointing in the antisolar direction; a transverse component A_2; and a normal component A_3. They are expressed in units of 10^{-8} AU day^{-2}, equivalent to 2.004×10^{-5} cm s^{-2}. The magnitude of the acceleration at a distance r from the Sun is therefore given as $\sqrt{A_1^2+A_2^2+A_3^2}\; g_{\rm ice}(r)$. However, A_3 is seldom determined, as part of an orbital solution, with satisfactory accuracy, while for single-apparition comets a meaningful value of A_1, if sufficiently large for reliable detection, is always positive (indicating that the acceleration points away from the Sun)[13] and, typically, it exceeds A_2 in absolute value, often by one order of magnitude (Marsden & Williams 2008). As a result, A_1 is the prime nongravitational parameter to solve for. Next, it is customary to solve for A_1 and A_2, and only quite rarely for A_1, A_2, and A_3, which usually yields a meaningless A_3 with an error exceeding the parameter's nominal value. These three options are in the following marked with subscripts 1, 2, and 3, respectively.

Some of the standard nongravitational (SN) solutions that we ran are listed in Table 11. We began testing these solutions by comparing them with the MPC's orbits. The first option of our first solution, SN I_1 in Table 11, using all accepted observations from 2011 Septem-

[13] It is not always appreciated that the parameter A_1 of this symmetrical nongravitational law has a very different meaning in orbital solutions that link successive returns of short-period comets (Sekanina 1993).

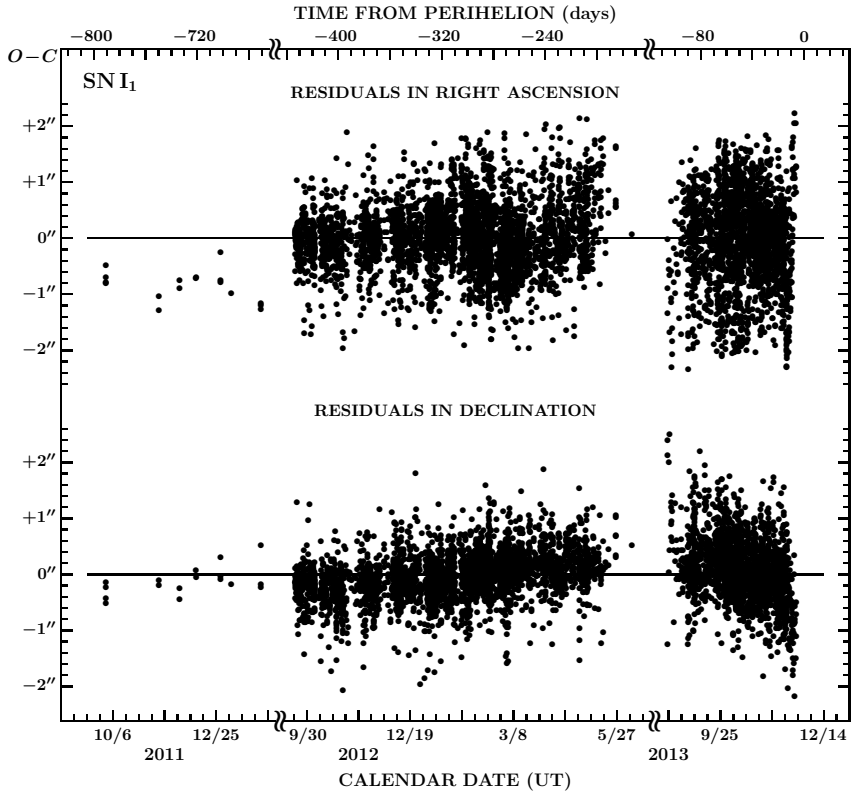

Figure 21. Distribution of residuals for 6177 observations between 2011 September 30 and 2013 November 22 from the standard nongravitational solution SN I$_1$. Although the quality of fit is better than by an equivalent gravitational solution, fairly strong systematic trends in both right ascension and declination still persist.

ber 30 through 2013 November 22, compares favorably with the MPC's first two published nongravitational sets of elements (Williams 2013b, 2013c), based, respectively, on 6120 and 6138 observations from the same period of time and resulting in $A_1 = +8.93 \pm 0.12$ and $A_1 = +9.13$ in units of 10^{-8} AU day^{-2}. The second option of the solution, SN I$_2$, similarly compares commendably with the MPC's most recently published nongravitational orbit (Williams 2014), based on 6217 observations and giving $A_1 = +7.84$ and $A_2 = +0.64$ in the same units. An agreement with the orbital results by Nakano (2013c), who derived $A_1 = +6.09 \pm 0.24$ and $A_2 = +0.66 \pm 0.07$ in the same units, is somewhat less satisfactory in the radial component.

The distribution of residuals from the SN I$_1$ solution is plotted in Figure 21. Similar distributions resulted from the SN I$_2$ and SN I$_3$ runs listed in Table 11. The quality of fit in Figure 21 is better than from the equivalent gravitational solutions, but not free from trends in either coordinate. We found the match between the standard nongravitational model and observations disappointing for two reasons: (i) solving in addition to A_1 also for A_2 and A_3 offered virtually no improvements; and (ii) comparison of Table 11 with Table 9 suggests that, except for SN I and SN II, the standard nongravitational solutions failed to reduce the mean residual over that given by the equivalent gravitational solutions. Playing only minor roles, the transverse and normal components could be neglected. And, finally, all SN solutions with the end date before November 2013 led to poorly defined and/or meaningless values of the parameters.

6.3. *Modified Nongravitational Solutions (MN)*

The failure of the standard nongravitational law $g_{\rm ice}(r)$ made us search for improvements. The most critical parameter in Eq. (61) is the scaling distance r_0. After introducing the law, Marsden et al. (1973) investigated the physical meaning of r_0 and found out that on the assumptions of an isothermal model's constant Bond albedo and emissivity and constant values of the exponents m, n, and k, the distance r_0 measured essentially the heat of sublimation L of the volatile substance that dominates momentum transfer to the nucleus, varying to a first approximation inversely as its square,

$$r_0 \simeq \left(\frac{\rm const}{L}\right)^2 . \qquad (62)$$

With the sublimation heat of 11 400 cal mol^{-1} for water ice, the constant equals 19 100 AU$^{\frac{1}{2}}$ cal mol^{-1} for the isothermal model under consideration here.

It should be noted that the only basis for introducing this generic form of what we call a modified nongravitational law is, as pointed out by Marsden et al. (1973), a similarity in the shapes of normalized sublimation curves for a variety of species except for major horizontal shifts in a plot of log (sublimation rate) against log (r/r_0) that generally fit Eq. (62). In other words, a normalized sublimation rate is incomparably less sensitive to the values of the exponents m (which always slightly exceeds 2), n, and k, than to the scaling distance r_0. This approach is a useful tool to examine momentum-transfer effects in the orbital motion due to species of unknown identity.

Table 12

Summary of Modified Nongravitational Solutions (MN) and Solution Accounting for Nucleus' Dwindling Dimensions (DD) for Comet C/2012 S1, Constants r_0, $r_\star$, and ξ, and Parametric Values A_1, A_2, and A_3.

Solution	Start and end dates of observations used	Number of observations	Option	Mean residual	Distance r_0 or $r_\star$ (AU)	Mass erosion rate exponent ξ	Parametric values (10^{-8} AU day^{-2})		
							A_1	A_2	A_3
MN I	2011 Sept. 30–2013 Nov. 22	6177	MN I_1	$\pm0''.56$	3.11 ± 0.16	...	$+8.67 \pm 0.11$	...	...
			MN I_2	±0.56	3.50 ± 0.18	...	$+7.87 \pm 0.12$	$+0.53 \pm 0.03$	...
			MN I_3	±0.55	2.27 ± 0.13	...	$+12.81 \pm 0.28$	-2.15 ± 0.16	-4.81 ± 0.27
MN II	2013 Feb. 1–2013 Oct. 30	3762	MN II_1	±0.58	1.93 ± 0.12	...	$+21.23 \pm 1.13$	...	...
			MN II_2	±0.58	2.10 ± 0.15	...	$+16.86 \pm 0.89$	$+2.04 \pm 0.30$	...
DD I	2011 Sept. 30–2013 Nov. 22	6177	DD I_1	±0.57	0.024; fixed	2.68 ± 0.04	$+7.82 \pm 0.11$	...	...
			DD I_2	±0.56	0.024; fixed	2.60 ± 0.04	$+7.02 \pm 0.11$	$+0.54 \pm 0.02$	...
			DD I_3	±0.56	0.024; fixed	2.35 ± 0.06	$+3.46 \pm 0.27$	$+1.25 \pm 0.06$	$+1.31 \pm 0.09$

Thus, to test the use of modified nongravitational solutions, we retained the values of m, n, and k for water ice from Eq. (61), but searched for the best fit by varying r_0 in a law $g(r; r_0)$, given by the same formal expression as the law $g_{\rm ice}(r)$ and normalized to $g(1\ {\rm AU}; r_0) = 1$.

Table 12 lists two examples of the modified solutions. The first, MN I, covered the entire period of ground-based observations and confirmed that the value of the scaling distance used in the standard nongravitational law was essentially valid over such long periods of time. A weighted mean of r_0 from the three options of the MN I solution equals 2.82 AU, in a remarkably good agreement with $r_0 = 2.808$ AU used in the standard law $g_{\rm ice}(r)$. The distributions of residuals were practically identical to those of the equivalent SN solutions and are not displayed.

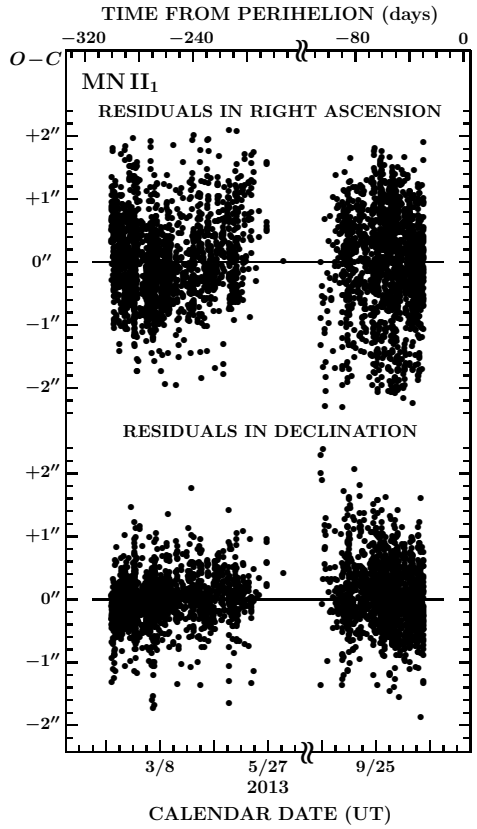

Figure 22. Distribution of residuals for 3762 observations between 2013 February 1 and October 30 from the modified nongravitational solution MN II_1. No obvious trends are apparent in either coordinate. This solution yields the most representative set of orbital elements (Table 13) that we are able to offer for the 9-months long period of time.

The second example of the modified solutions, MN II, covered only a limited period of time. In Sec. 6.1 we found that the gravitational solution PG IX offered a very satisfactory match to all observations from the period of time ending 2013 January 31. The period of time covered by the solution MN II started the next day and extended to 2013 October 30, thus avoiding the stormy period of activity (Sec. 2.1). The scaling distances r_0, derived as part of the two listed options, MN II_1 and MN II_2, agree with each other within the errors and are only moderately smaller than 2.8 AU. Both options provide nearly identical distributions of residuals that show no obvious trends in either coordinate. The residuals from the solution MN II_1 are in Figure 22 and the respective orbital elements, in Table 13, are judged to be the most representative for the given period of time that we are able to offer. We also tried to calculate an option MN II_3, but no clearly defined minimum on the curve of the sum of squares of residuals was found at $r_0 < 5$ AU and for all tested values of r_0 greater than 3.4 AU the radial component A_1 came out negative, suggesting that given the overall degree of accuracy, an excessive number of parameters was attempted to be solved for in this option.

Even though the modified nongravitational law $g(r; r_0)$ proves a useful tool in instances when the orbital motion is clearly inconsistent with the standard law, $g_{\rm ice}(r)$, its use is essentially a last-resort-type of a solution. The

Table 13

Orbital Elements of Comet C/2012 S1 for the Period of 2013 February 1–October 30 (Solution MN II_1).

Epoch of osculation (TT)	2013 Nov 24.0
Time of perihelion, t_π (TT)	2013 Nov 28.78122 ± 0.00007
Argument of perihelion, ω	$345^\circ.57506 \pm 0^\circ.00007$
Longitude of ascending node, Ω	$295^\circ.65252 \pm 0^\circ.00006$
Orbital inclination, i	$62^\circ.40108 \pm 0^\circ.00036$
Perihelion distance, q (AU)	$0.01244488 \pm 0.00000013$
Orbital eccentricity, e	$0.99994358 \pm 0.00000003$
Nongravitational parameters of law $g(r; r_0)$:	
Scaling distance r_0 (AU)	1.93 ± 0.12
Radial component A_1 (10^{-8} AU day^{-2})	21.23 ± 1.13

most beneficial byproduct of its successful application is presented by Eq. (62): one learns whether the nongravitational forces affecting the comet's motion were due primarily to sublimation of a species more volatile or more refractory than water ice, if r_0 deviates substantially from 2.8 AU.

6.4. *Nongravitational Solutions Accounting for Nucleus' Dwindling Dimensions (DD)*

The nongravitational laws under consideration have so far failed to account for the nucleus' gradual erosion, whose existence has in the previous sections been demonstrated beyond any doubt. Effects of cascading fragmentation on the comet's orbital motion could likewise be approximately mimicked by numerically simulating the dwindling dimensions of the nucleus modeled as a single body. To incorporate an eroding nucleus into the momentum-transfer considerations, we begin with a basic conservation of momentum equation. If at time t the mass of the nucleus is $\mathcal{M}(t)$, its mass loss rate by erosion is $\dot{\mathcal{M}}(t)$, the outflow velocity of the eroded mass is $\nu(t)$, the erosion-driven acceleration of the nucleus is $\eta(t)$, and an average momentum-transfer efficiency, depending primarily on the erosion rate distribution over the nuclear surface, is $\Psi < 1$, the differentiated conservation of momentum equation is

$$\dot{\mathcal{M}}(t)\,\nu(t) + \Psi\mathcal{M}(t)\,\eta(t) = 0. \tag{63}$$

If at time t a spherical nucleus of radius $\mathcal{R}(t)$ is shrinking at a rate of $\dot{\mathcal{R}}(t)$, the acceleration equals

$$\eta(t) = -\frac{3\Psi}{2}\,\frac{\dot{\mathcal{R}}(t)}{\mathcal{R}(t)}\,\nu(t) = -\frac{3\Psi}{2\rho}\,\frac{\dot{\mathcal{E}}(t)}{\mathcal{R}(t)}\,\nu(t), \tag{64}$$

where the minus sign, indicating that the direction of the dynamical impulse on the nucleus is opposite to that of the outflowing mass, is in the following considerations inconsequential. The rate of dwindling nuclear size, $\dot{\mathcal{R}}(t)$, is expressed as a function of the effective mass erosion (or sublimation) rate $\dot{\mathcal{E}}(t)$ per unit surface area and the bulk density ρ. The relation between the nuclear radius $\mathcal{R}(t)$ at time t and its radius $\mathcal{R}(t_0)$ at a reference time t_0, is given by

$$\mathcal{R}(t) = \mathcal{R}(t_0) - \frac{1}{\rho}\int_{t_0}^{t} \dot{\mathcal{E}}(t)\,dt, \tag{65}$$

where the rate $\dot{\mathcal{E}} > 0$.

It is more convenient to integrate over heliocentric distance r than over time. In that case it is necessary to distinguish whether or not the integration is carried out through perihelion, at time t_π. If it is, one needs to integrate in two parts, from t_0 to t_π and from t_π to t. Because C/2012 S1 disintegrated before perihelion, we contemplate from now on only that option. In order to derive an expression for the momentum-transfer law that is consistent with the formalism of the employed orbit determination code, we introduce two approximations.

The first approximation has to do with the conversion of the integration variable from time to heliocentric distance and is of the same nature as that used in Sec. 5.2 to derive Eq. (55). In a parabolic case, an increment dt is before perihelion related to an increment dr by

$$dt = -c_0\,r^{\frac{1}{2}}\Big(1-\frac{q}{r}\Big)^{-\frac{1}{2}}dr \approx -c_0\,r^{\frac{1}{2}}dr, \tag{66}$$

where c_0 is a constant and q is the perihelion distance. It is noted that this approximation is inadmissible when the integration is carried out through perihelion.

The other approximation concerns the erosion rate, for which — based on our experience with $g_{\rm ice}(r)$ — we assume a power law of heliocentric distance,

$$\dot{\mathcal{E}}(r) = h_0\,r^{-\xi}, \tag{67}$$

where $h_0 > 0$ and $\xi > 2$ are constants. This expression allows one to iteratively adjust ξ to the observations and thus to learn from the degree of steepness about the nature of a momentum-transfer effect.

Inserting from Eqs. (66) and (67) into Eq. (65), we obtain, after identifying t_0 with the time of complete disintegration, $t_\star$, when $\mathcal{R}(t_\star) = 0$ and $r = r_\star$,

$$\mathcal{R}(t) = \frac{c_0 h_0}{\rho}\int_{r_\star}^{r} r^{\frac{1}{2}-\xi}\,dr = \frac{c_0 h_0 r_\star^{\frac{3}{2}-\xi}}{\rho\,(\xi-\frac{3}{2})}\left[1-\left(\frac{r}{r_\star}\right)^{\frac{3}{2}-\xi}\right]. \tag{68}$$

Inserting Eqs. (67) and (68) into Eq. (64) and approximating the outflow velocity with a constant, $\nu(t) = \nu_0$, the expression for the acceleration $\eta(r)$ is finally

$$\eta(r) = \frac{3\Psi\nu_0(\xi-\frac{3}{2})\,r_\star^{-\frac{3}{2}}}{2c_0 a_0}\,\mathcal{G}(r; r_\star, \xi), \tag{69}$$

where

$$\mathcal{G}(r; r_\star, \xi) = a_0\,\frac{\left(\dfrac{r}{r_\star}\right)^{-\xi}}{1-\left(\dfrac{r}{r_\star}\right)^{\frac{3}{2}-\xi}} \tag{70}$$

and a_0 is a normalization constant,

$$a_0 = r_\star^{-\xi} - r_\star^{-\frac{3}{2}}. \tag{71}$$

The function for $\mathcal{G}(r; r_\star, \xi)$ in Eq. (70) formally matches the general expression for the momentum-transfer law $G(r; r_0, b_0)$ in an upgraded *EXORB* orbit determination code,[14] which reads

$$G(r; r_0, b_0) = \alpha_0\left(\frac{r}{r_0}\right)^{-m}\left[1+b_0\left(\frac{r}{r_0}\right)^{n}\right]^{-k}, \tag{72}$$

when $r_0 = r_\star$, $b_0 = -1$, $m = \xi$, $n = \frac{3}{2} - \xi$, $k = 1$, and $\alpha_0 = a_0$. Whereas r_0 in $g(r; r_0)$ measures the degree of volatility of a species [note that $G(r; r_0, +1) \equiv g(r; r_0)$], the value of $r_\star$ in $\mathcal{G}(r; r_\star, \xi)$ determines the point in the orbit where the disintegrating object ultimately perishes. This is a major difference that makes the $\mathcal{G}(r; r_\star, \xi)$ law diverge to infinity at $r = r_\star$ and undefined at $r \le r_\star$, that is, at $t \ge t_\star$. In practice, of course, no comet perishes at any particular point, but along a finite arc of the orbit. Accordingly, $r_\star$ should be perceived as a dynamical parameter that describes a general location in the orbit where the comet's motion ceased to follow any consistent pattern.

[14] At our request, A. Vitagliano kindly implemented the necessary modifications to his orbit determination code.

It should be remarked that a more complex function for $\dot{\mathcal{E}}$, such as $g(r; r_0)$, would require another modification of the orbit determination code. In principle, however, there is no limit to experimentation along these lines and a host of functions can in the future be tested in an effort to further refine the method of accounting for the nongravitational effects in the orbital motions of comets.

In order to understand the meaning of ξ from Eq. (67) in terms of a relationship between $\dot{\mathcal{E}}(r)$ and $G(r; r_0, +1)$ within a limited range of heliocentric distances, we examine this exponent, defined in that equation for any heliocentric distance by

$$\xi = -\frac{\partial}{\partial \ln r} \ln \dot{\mathcal{E}}(r), \tag{73}$$

as a function of the parameters of the $G(r; r_0, +1)$ law by requiring that at heliocentric distances near r' it also satisfies a condition

$$\xi(r') \simeq -\frac{\partial}{\partial \ln r} \ln G(r'; r_0, +1). \tag{74}$$

From Eq. (72) we find that

$$\xi(r') \simeq \begin{cases} m & \text{if } r' \ll r_0, \\ m+\frac{1}{2}nk & \text{if } r' = r_0, \\ m+nk & \text{if } r' \gg r_0, \\ m+\dfrac{nk}{1+(r'/r_0)^{-n}} & \text{elsewhere.} \end{cases} \tag{75}$$

With the values of the exponents for $g_{\rm ice}(r)$ from Eq. (61), we find that $\lim_{r\to 0} \xi(r) \approx 2$, $\xi(\frac{2}{3}r_0) \approx 5$, and $\xi(r_0) \approx 14$, which are useful specific values to keep in mind.

We applied the law from Eq. (70) to the whole set of ground-based observations to derive the solution DD I, listed in Table 12. The computations followed an approach, in which we first chose an arbitrary value of $r_\star$ and a sequence of arbitrary values of ξ. We optimized ξ for the given $r_\star$ by searching for the best fit with a minimum sum of squares of residuals, $\Sigma(\mathrm{o}-\mathrm{c})^2 = \min$. We repeated this procedure for a sequence of chosen values of $r_\star$ and searched for an optimized pair of values $r_\star$ and ξ using again $\Sigma(\mathrm{o}-\mathrm{c})^2$. We found that the fit continued to improve with decreasing $r_\star$ down to 0.01 AU, the least value employed in the computations. The quality of fit had a tendency to level off at $r_\star \lesssim 0.05$ AU. For example, in the option DD I_1 (Table 12), the sum of squares of residuals from an optimized solution for $r_\star = 0.01$ AU amounted to 98.3 percent of the sum for $r_\star = 0.3$ AU, but fully 99.92 percent of the sum for $r_\star = 0.05$ AU. A formal parabolic fit through a number of $\Sigma(\mathrm{o}-\mathrm{c})^2$ points showed that its minimum was reached at a slightly negative (and therefore meaningless) $r_\star$, but with a standard deviation exceeding its value. Fixing $r_\star$ at 0.024 AU, a heliocentric distance at which all activity ceased 3.5 hours before perihelion (Sec. 3.9), is at 1.7 times the standard deviation, well within the uncertainties involved.

Table 12 shows that in terms of the mean residual the DD I solution is competitive with MN I and also with SN I from Table 11. The distributions of residuals (not displayed) are also very similar. It appears that the proposed nongravitational law that accounts for the nucleus' dwindling dimensions does not enjoy any advantage over the other nongravitational laws in applications to observations taken long before the effect of dwindling dimensions could dominate. The role of this law in applications to observations from times that are close to the disintegration of the nucleus is investigated in Sec. 6.6.

6.5. *Astrometric Positions from STEREO-B*

In an effort to extend the comet's astrometric observations beyond the period of observability from the ground, which ended on 2013 November 22, we searched for adequate coronagraphic observations with instruments on board SOHO, STEREO-A, and STEREO-B. Because the comet did not enter the field of view of the C2 coronagraph until November 28.5 UT and the field of view of the COR-2A coronagraph until November 28.2 UT, by far the best prospects for acquiring acceptable spaceborne astrometry from the period after November 22 were offered by the COR-2 coronagraph on board STEREO-B; the comet entered this instrument's field of view as early as November 26.2 UT and the image taken at 6:25 UT was the first with the center of the head separated from the field's edge enough that it could be astrometrically determined; the second author measured all positions of the comet until 15:00 UT on November 28. The CCD images from November 26–27 were 2048 by 2048 pixels (equivalent to a pixel size of ∼15 arcsec or approximately 12 000 km at the comet), except between 9:56 and 14:24 UT on the 26th, when all were 1024 by 1024 pixels (with a pixel size twice as large); none of these images was measured. All images on November 28 were 1024 by 1024 pixels and, starting at about 10:54 UT, they showed an elongated nuclear region, making the measurement increasingly uncertain. Table 14 lists all derived astrometric positions until 12:00 UT November 28, when the comet was a little over 8 $R_\odot$ from the Sun.

The acquisition and reduction of the comet's images were accomplished with the use of the *Astrometrica* software package.[15] An aperture radius of 2 pixels, the smallest that *Astrometrica* allows, was employed. The brightest pixel in the comet's head was located first and then the centroid was shifted to match this position as close as possible, usually within 0.3 pixel. The decision to proceed this way was made in response to a recommendation by Yeomans et al. (2004) that the brightest pixel defines the position of the nucleus more accurately than a best-match two-dimensional Gaussian fit.

6.6. *Orbital Solutions Linking Ground-Based and Spaceborne Astrometric Observations*

Although the quality of the astrometric observations derived from the STEREO-B images is, because of the COR-2 detector's large pixel size, inferior compared to the ground-based astrometry, the extension of the orbital arc more than offsets this drawback. Indeed, in terms of true anomaly, the whole period of time covered by the ground-based data amounts to a range of less than 18°, while the 2.2-day long period of time covered by the data in Table 14 is equivalent to a range of 39°, more than twice as much! In addition, analysis of the orbital motion close to the Sun should offer unique complementary information on the comet's physical state during this critical time.

[15] See the website `http://www.astrometrica.at`.

Table 14

Astrometric Positions of the Head of Comet C/2012 S1 Measured in Images Taken with COR-2 Coronagraph on Board STEREO-B on 2013 November 26–28.

No.	2013 (UT)	R.A.(2000)	Dec.(2000)	No.	2013 (UT)	R.A.(2000)	Dec.(2000)
		h m s	° ′ ″			h m s	° ′ ″
1	Nov. 26.26762	06 48 56.46	+21 08 53.1	64	Nov. 27.64263	06 48 48.81	+21 10 55.9
2	26.28845	06 48 57.00	+21 08 54.2	65	27.65305	06 48 48.13	+21 11 08.4
3	26.30929	06 48 57.37	+21 08 50.7	66	27.66346	06 48 47.40	+21 11 11.1
4	26.33012	06 48 57.85	+21 08 46.9	67	27.68430	06 48 45.87	+21 11 36.0
5	26.35095	06 48 58.34	+21 08 33.3	68	27.69471	06 48 45.89	+21 11 38.1
6	26.37179	06 48 58.94	+21 08 31.7	69	27.70513	06 48 44.37	+21 11 51.1
7	26.39262	06 48 59.06	+21 08 28.5	70	27.72596	06 48 42.79	+21 12 08.1
8	26.41345	06 48 59.70	+21 08 26.3	71	27.73638	06 48 42.10	+21 12 20.9
9	26.60096	06 49 02.88	+21 07 50.8	72	27.74680	06 48 42.10	+21 12 22.9
10	26.62180	06 49 03.44	+21 07 40.9	73	27.76763	06 48 39.70	+21 12 50.2
11	26.64263	06 49 03.96	+21 07 38.0	74	27.77805	06 48 38.94	+21 13 03.8
12	26.66346	06 49 04.31	+21 07 36.8	75	27.78846	06 48 38.92	+21 13 06.3
13	26.68430	06 49 04.44	+21 07 34.8	76	27.80930	06 48 36.61	+21 13 33.8
14	26.70513	06 49 04.83	+21 07 31.6	77	27.81971	06 48 35.79	+21 13 48.4
15	26.72596	06 49 04.55	+21 07 31.5	78	27.83013	06 48 35.02	+21 13 52.4
16	26.74680	06 49 05.06	+21 07 30.4	79	27.85096	06 48 33.37	+21 14 19.8
17	26.76763	06 49 05.23	+21 07 28.7	80	27.86138	06 48 32.61	+21 14 34.1
18	26.78846	06 49 04.97	+21 07 26.0	81	27.87180	06 48 31.02	+21 14 49.1
19	26.80930	06 49 05.32	+21 07 22.3	82	27.89263	06 48 29.40	+21 15 07.8
20	26.83013	06 49 05.67	+21 07 21.4	83	27.90305	06 48 28.50	+21 15 21.5
21	26.85096	06 49 05.40	+21 07 21.7	84	27.91346	06 48 27.65	+21 15 35.9
22	26.87180	06 49 05.75	+21 07 19.7	85	27.93430	06 48 25.17	+21 16 06.2
23	26.89263	06 49 05.97	+21 07 17.6	86	27.94471	06 48 24.33	+21 16 21.3
24	26.91346	06 49 05.54	+21 07 18.0	87	27.95513	06 48 22.74	+21 16 38.0
25	26.93430	06 49 06.27	+21 07 24.7	88	27.97596	06 48 20.28	+21 17 18.6
26	26.95513	06 49 05.77	+21 07 24.3	89	27.98638	06 48 19.41	+21 17 33.2
27	26.97596	06 49 06.03	+21 07 22.3	90	27.99680	06 48 17.69	+21 17 50.7
28	26.99680	06 49 05.39	+21 07 24.0	91	28.01763	06 48 16.58	+21 18 13.2
29	27.01763	06 49 06.70	+21 07 17.9	92	28.02805	06 48 14.85	+21 18 38.6
30	27.03846	06 49 05.50	+21 07 19.5	93	28.03846	06 48 12.50	+21 18 53.1
31	27.05930	06 49 05.86	+21 07 24.6	94	28.05930	06 48 09.38	+21 19 41.9
32	27.08013	06 49 04.98	+21 07 35.1	95	28.06971	06 48 09.65	+21 19 50.2
33	27.10096	06 49 04.66	+21 07 32.2	96	28.08013	06 48 07.90	+21 20 14.0
34	27.12180	06 49 04.97	+21 07 33.3	97	28.10096	06 48 04.42	+21 21 14.6
35	27.14263	06 49 04.57	+21 07 34.4	98	28.11138	06 48 02.14	+21 21 22.9
36	27.16346	06 49 04.08	+21 07 45.1	99	28.12180	06 48 00.39	+21 21 49.1
37	27.18430	06 49 04.22	+21 07 43.6	100	28.14263	06 47 57.06	+21 22 42.2
38	27.20513	06 49 03.68	+21 07 44.6	101	28.15305	06 47 57.30	+21 22 50.2
39	27.22596	06 49 04.10	+21 07 53.9	102	28.16346	06 47 53.64	+21 23 25.0
40	27.24680	06 49 02.89	+21 07 56.8	103	28.18430	06 47 49.97	+21 24 23.2
41	27.26763	06 49 02.85	+21 08 06.9	104	28.19471	06 47 48.16	+21 24 50.4
42	27.28846	06 49 02.32	+21 08 08.4	105	28.20513	06 47 46.31	+21 25 20.7
43	27.30930	06 49 01.79	+21 08 18.3	106	28.22596	06 47 43.14	+21 26 25.0
44	27.33013	06 49 01.28	+21 08 20.6	107	28.23638	06 47 41.25	+21 26 53.8
45	27.35096	06 49 00.79	+21 08 31.8	108	28.24680	06 47 37.97	+21 27 24.9
46	27.37180	06 49 00.08	+21 08 33.0	109	28.26763	06 47 33.93	+21 28 26.1
47	27.39263	06 48 59.34	+21 08 45.2	110	28.27805	06 47 32.81	+21 28 52.9
48	27.41346	06 48 58.97	+21 08 47.0	111	28.28846	06 47 30.86	+21 29 26.0
49	27.43430	06 48 57.64	+21 09 01.3	112	28.30930	06 47 25.12	+21 30 57.3
50	27.44471	06 48 57.69	+21 09 02.0	113	28.31971	06 47 23.26	+21 31 32.8
51	27.45513	06 48 57.05	+21 09 13.3	114	28.33013	06 47 19.68	+21 32 06.7
52	27.47596	06 48 56.37	+21 09 15.5	115	28.35096	06 47 14.34	+21 33 35.2
53	27.48638	06 48 55.76	+21 09 27.5	116	28.36138	06 47 12.94	+21 34 06.0
54	27.49680	06 48 55.76	+21 09 27.6	117	28.37180	06 47 08.74	+21 35 05.3
55	27.51763	06 48 54.37	+21 09 42.9	118	28.39263	06 47 03.06	+21 36 37.6
56	27.52805	06 48 54.49	+21 09 44.2	119	28.40305	06 47 01.81	+21 37 08.5
57	27.53846	06 48 53.81	+21 09 55.1	120	28.41346	06 46 58.19	+21 38 07.1
58	27.55930	06 48 53.08	+21 10 08.9	121	28.43430	06 46 52.46	+21 39 43.4
59	27.56971	06 48 52.38	+21 10 10.3	122	28.44471	06 46 48.87	+21 40 44.0
60	27.58013	06 48 51.75	+21 10 22.4	123	28.45513	06 46 45.24	+21 41 44.4
61	27.60096	06 48 50.96	+21 10 26.0	124	28.47596	06 46 37.87	+21 43 50.8
62	27.61138	06 48 50.22	+21 10 38.3	125	28.48638	06 46 34.23	+21 44 54.9
63	27.62180	06 48 49.56	+21 10 50.8	126	28.49680	06 46 27.99	+21 46 28.7

Table 15

Summary of Gravitational and Nongravitational Solutions for Comet C/2012 S1 That Employ Ground-Based and Spaceborne Astrometry, and Their Parameters A_1, A_2, and A_3.

Solution	Start date of observations employed[a]	Number of observations	Option	Mean residual[b]	Distance r_0 or $r_\star$ (AU)	Mass erosion rate exponent ξ	Parametric values (10^{-8} AU day^{-2})[c]		
							A_1	A_2	A_3
PGs I	2011 Sept. 30	6303	.....	±3″.55	...	...	...	...	...
PGs II	2013 Oct. 31	684	.....	±7.74	...	...	...	...	...
SNs I	2011 Sept. 30	6303	SNs I_1	±2.84	...	...	$+10.45 \pm 0.19$	...	...
			SNs I_2	±2.74	...	...	$+9.34 \pm 0.20$	$+0.97 \pm 0.06$	...
			SNs I_3	±2.04	...	...	-0.62 ± 0.36	$+4.73 \pm 0.13$	$+6.45 \pm 0.19$
SNs II	2013 Oct. 31	684	SNs II_1	±4.72	...	...	$+52.2 \pm 2.3$	...	...
			SNs II_2	±3.75	...	...	$+113.6 \pm 5.7$	-12.6 ± 1.1	...
			SNs II_3	±3.61	...	...	$+65.1 \pm 9.5$	-0.2 ± 2.2	$+8.5 \pm 1$ 3
MNs I	2013 Oct. 31	684	MNs I_1	±2.77	0.438 ± 0.024	...	$+4.61 \pm 0.15$	...	...
			MNs I_2	±2.77	0.442 ± 0.025	...	$+5.24 \pm 0.27$	$+0.25 \pm 0.14$	...
			MNs I_3	±2.76	0.444 ± 0.025	...	$+6.09 \pm 0.83$	$+0.11 \pm 0.44$	-0.15 ± 0.35
NAs I	2013 Oct. 31	684	NAs I_1	±2.78	...	...	$+17.75 \pm 0.56$	...	...
			NAs I_2	±2.79	...	...	$+16.36 \pm 0.94$	$+0.99 \pm 0.54$	...
			NAs I_3	±2.80	...	...	$+13.1 \pm 2.5$	$+2.8 \pm 1.4$	$+1.4 \pm 1.0$
DDs I	2013 Oct. 31	684	DDs I_1	±2.77	0.003 ± 0.010	3.90 ± 0.10	$+4.37 \pm 0.14$	...	...
DDs II	2013 Oct. 31	684	DDs II_1	±2.77	0.024; fixed	3.86 ± 0.11	$+4.56 \pm 0.15$	...	...
			DDs II_2	±2.79	0.024; fixed	3.94 ± 0.11	$+3.58 \pm 0.19$	$+0.23 \pm 0.11$	...
			DDs II_3	±2.69	0.024; fixed	4.49 ± 0.18	$+0.08 \pm 0.14$	$+0.81 \pm 0.10$	$+0.44 \pm 0.06$

[a] End date was always 2013 November 28, the date of perihelion passage.
[b] This is an unweighted mean residual.
[c] Except that for all MNs I and NAs I options the unit is 10^{-15} AU day^{-2}.

As with the ground-based observations, preliminary runs were made to obtain ad hoc orbital solutions to check the residuals from the 126 STEREO astrometric observations in Table 14. No entry was discarded, as none of the residuals exceeded the pixel size. The 90 data points from November 26–27 displayed a scatter within ±10 arcsec in either coordinate and each was assigned a weight of 0.2 the weight of the ground-based observations, while the 36 data points from November 28 had residuals well within ±20 arcsec in either coordinate and each was assigned a weight of 0.1. The resulting set of all ground-based and spaceborne astrometric observations totaled 6303.

6.6.1. *Runs linking all 6303 observations.*

To test the linkage of the ground-based and spaceborne data in orbital computations, we began with a gravitational solution, PGs I, and with three options of the nongravitational solution SNs I, each of them based on all 6303 observations (a suffix "s" was added to every solution that included spaceborne observations to distinguish it from solutions based on the ground-based observations only).

The results are listed at the top of Table 15 and the distributions of residuals are plotted in Figure 23. The residuals show that neither the gravitational solution nor any nongravitational solution based on the standard law $g_{\rm ice}(r)$ could successfully link the comet's ground-based observations with its STEREO ones. Very strong systematic trends in the residuals of up to 5 arcsec in the ground-based data and in excess of 1 arcmin(!) in the STEREO data are seen in Figure 23. The fact that the fit based on the standard nongravitational law is only marginally better than the gravitational fit is particularly disappointing: the $g_{\rm ice}$ law overcorrected the residuals from the last ground-based observations and reduced the residuals from the STEREO observations by only some 10–20 arcsec, but did not remove the exponentially diverging trends. A physically meaningless negative value of A_1 resulted from the run SNs I_3 in Table 15.

What is the meaning of the trends in the residuals from the gravitational solution in Figure 23? From the strongly negative trend in right ascension and a moderately positive trend in declination in the last week of ground-based observations, the comet's observed geocentric motion relative to the computed one was increasingly toward the west-northwest. With respect to the Earth, the comet's motion was at that time in position angle 116°, that is, to the east-southeast, in exactly the opposite direction. During the two days of STEREO-B observations, the trend in the residuals was strongly positive in right ascension and almost equally strongly negative in declination, so that in reference to the spacecraft the comet's observed motion relative to the computed one was increasingly toward the southeast. The comet's motion with respect to STEREO-B was in position angle 318°, that is, to the northwest, again in exactly the opposite direction. In summary, the distribution of residuals during the last two weeks before perihelion show consistently that the comet's nucleus — or what was measured in its place — was increasingly lagging in the orbit behind the position expected from the gravitational law: *the comet was rapidly decelerating*. The deceleration did not however follow the standard nongravitational law, indicating apparently that *outgassing of water was not the primary trigger* of the nongravitational effects, the enormous production of water during Event 2 (Secs. 2.2–2.3) notwithstanding.

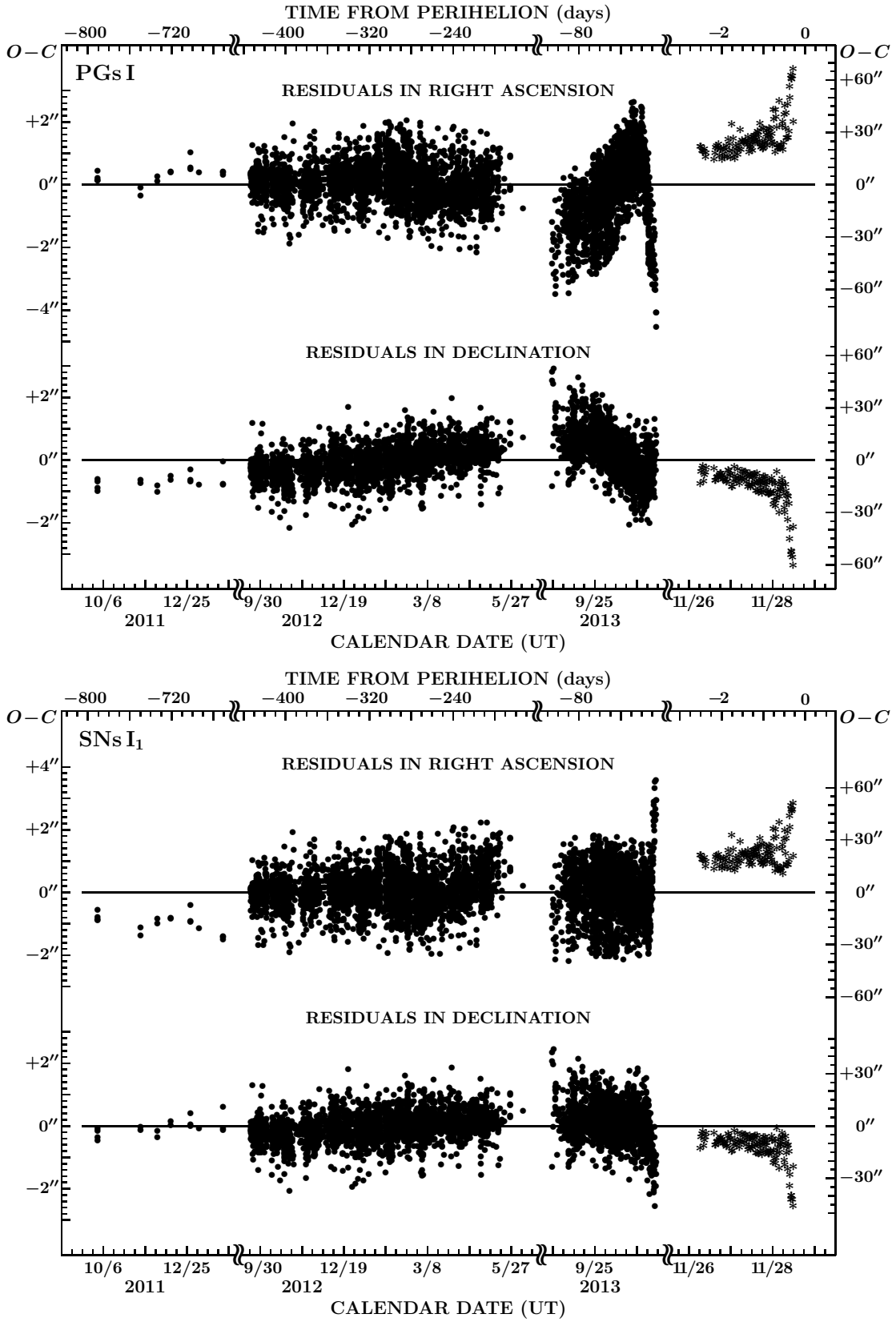
TIME FROM PERIHELION (days)
−800 −720 −400 −320 −240 −80 −2 0
O−C
PGs I
RESIDUALS IN RIGHT ASCENSION
+2″ 0″ −2″ −4″
+60″ +30″ 0″ −30″ −60″
RESIDUALS IN DECLINATION
+2″ 0″ −2″
+60″ +30″ 0″ −30″ −60″
10/6 12/25 9/30 12/19 3/8 5/27 9/25 11/26 11/28
2011 2012 2013
CALENDAR DATE (UT)
TIME FROM PERIHELION (days)
−800 −720 −400 −320 −240 −80 −2 0
O−C
SNs I1
RESIDUALS IN RIGHT ASCENSION
+4″ +2″ 0″ −2″
+60″ +30″ 0″ −30″ −60″
RESIDUALS IN DECLINATION
+2″ 0″ −2″
+30″ 0″ −30″
10/6 12/25 9/30 12/19 3/8 5/27 9/25 11/26 11/28
2011 2012 2013
CALENDAR DATE (UT)

Figure 23. Distributions of residuals for 6303 observations made between 2011 September 30 and 2013 November 28, from the solutions PGs I (top) and SNs I_1 (bottom). The ground-based data are depicted by bullets and their scales are on the left ordinate axis, the spaceborne data (the clusters on the far right) by asterisks and their scales (with steps a factor of 18 smaller) are on the right ordinate axis. The time scale is expanded for the spaceborne data by a factor of 40. The ground-based portion of the top plot resembles the distribution in Figure 18, while the quality of fit to the ground-based data at the bottom has somewhat deteriorated compared to that in Figure 21. The spaceborne data display an astonishingly large discrepancy with both solutions, showing residuals of up to nearly 70 arcsec.

6.6.2. *Runs PGs, SNs, and MNs linking observations from 2013 October 31–November 28.*

To examine whether the trends in the residuals from the STEREO-B data that dominate the appearance of Figure 23, could be due to an effect of an overwhelming preponderance of ground-based data on the fitting algorithm, we repeated the PGs and SNs runs over a much shorter period of time, with the number of ground-based observations reduced by about one order of magnitude. Since the MN II_1 solution provided a very satisfactory fit to the ground-based observations up to 2013 October 30, we now chose for the limited period of time a span from 2013 October 31 to November 28.

The results of these alternative runs, PGs II and SNs II, are listed in Table 15, while their distributions of residuals are in Figure 24. Cursory inspection reveals clear trends in the residuals from the ground-based observations and the diverging trends in the residuals from the spaceborne observations that are equally prominent as in Figure 23 (in the case of PGs II) or only slightly reduced (in the case of SNs II_1). Similar trends are also exhibited in the distributions of residuals from SNs II_2 and SNs II_3, which are not shown. We are satisfied that the exponentially diverging residuals from the STEREO observations were not a byproduct of the data selection process. It is noted that the unweighted mean residuals for these runs came out to be higher than in the solutions PGs I and SNs I. This was due to the fact that the fraction of less accurate spaceborne data increased from 2 percent to more than 18 percent of the total data used.

The next step was an application of the modified nongravitational law $g(r; r_0)$, keeping the exponents m, n, and k constant, as in Eq. (61), and optimizing the fit by varying only the scaling distance r_0. The results, referred to in Table 15 as the MNs I solution, were astonishing: r_0 came out to be a mere 0.44 AU and the fit was excellent, with no trends in the distribution of residuals, as illustrated in Figure 25. From Eq. (62) it follows that the comet's motion during this period of time was affected by one or more sublimating species whose sublimation heat was near $L \approx 29\,000$ cal mol^{-1}. The obvious candidate is atomic sodium,[16] known to sublimate profusely near perihelion from sungrazing comets and whose heat of sublimation is near 25 000 cal mol^{-1}.

We conclude from the runs of the modified nongravitational law that there is a contradiction between the nature of the outgassing-driven effects in the comet's motion at larger heliocentric distances (as described in Secs. 6.2–6.4, summarized in Tables 11–12, and resulting in the scaling distances of 2–4 AU) and near the Sun. For this reason we felt that there was no chance of successfully linking all 6303 observations from 2011–2013 with a single modified law and we made no effort to do so.

6.6.3. *Nongravitational solutions based on sublimation of sodium (NAs)*

Evidence that near the Sun the comet's orbital motion may have been subjected to strong outgassing of atomic sodium motivated us to formulate a new $g(r; r_0)$ law, equivalent to $G(r; r_0, +1)$ from Eq. (71), with constants that fit specifically the heliocentric-distance variations in the sublimation rate per unit surface area of atomic

[16] See, e.g., `http://en.wikipedia.org/wiki/Sodium`.

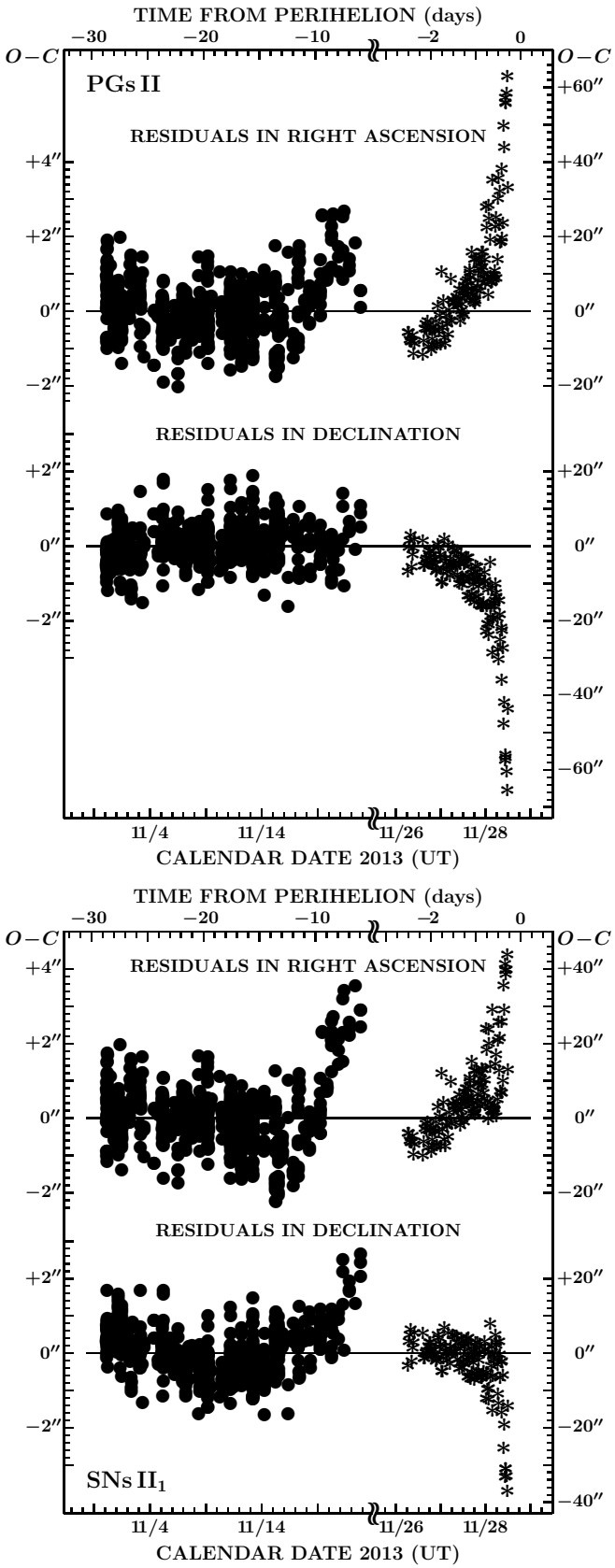

Figure 24. Distributions of residuals for 684 observations made between 2013 October 31 and November 28 from the solutions PGs II (top) and SNs II_1 (bottom). The spaceborne $O-C$ data are compressed by a factor of 10 compared to the scales of the ground-based data. See the caption to Figure 23 for more details.

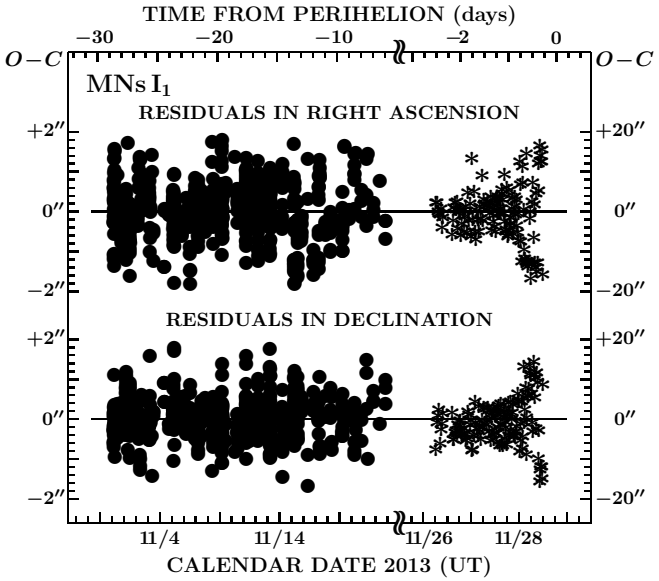

Figure 25. Distribution of residuals for 684 observations made between 2013 October 31 and November 28 from the run MNs I$_1$. Bullets are the ground-based data, asterisks the STEREO-B data. The $O-C$ scales of the latter are compressed by a factor of 10 compared to those of the former; recall that the November 28 data are twice as inaccurate as the November 26–27 data. Contrary to Figures 23 and 24, no trends in the residuals are apparent. Nearly identical distributions of residuals resulted from other two MNs I runs as well as the three NAs I runs. Only slightly different distributions, at the very end of the data set, resulted from the DDs I and DDs II solutions; see Table 15 for a summary of all these runs.

sodium derived for the isothermic model directly from the dependence of the saturated sodium-vapor pressure on the temperature. The constants that define this empirical sodium-sublimation law we refer to as $g_{\rm Na}(r)$ were found by least squares as follows:

$$\begin{aligned} r_0 &= 0.3458 \text{ AU}, \\ m &= 2.089, \\ n &= 3.603, \\ k &= 4.896, \\ \alpha_0 &= 1.3948 \times 10^9. \end{aligned} \tag{76}$$

Eleven values of the sodium sublimation rate between 0.01 AU and 0.8 AU were fitted by this law with a mean residual of ±5 percent.

The results, identified in Table 15 as a solution NAs I, show that the $g_{\rm Na}(r)$ law fitted the astrometric observations between 2013 October 31 and November 28 just as well as the modified nongravitational law with $r_0 \simeq 0.44$ AU. This is demonstrated by comparing the NAs I$_1$ and MNs I$_1$ runs. The distribution of residuals is at first sight indistinguishable from that in Figure 25, and we do not display it. The transverse and normal components of the nongravitational accelerations are not well defined, as in previous cases. In summary, we submit that the high probability of a major influence of sodium outgassing on the comet's orbital motion at heliocentric distances smaller than ∼1 AU is hereby confirmed. The issues as to whether the outgassing of sodium was the only major trigger of the observed nongravitational motion and what are the implications for the comet's nucleus are addressed in Sec. 6.7.

6.6.4. *Nongravitational solutions based on sublimation of silicates*

Sublimation of silicate grains, such as olivine or pyroxene, depends significantly on the grains' orbits, specifically on their perihelion distances (Sec. 3.9), which, in turn, are a function of the Sun's radiation pressure acceleration and the time of the grains' ejection from the nucleus. To investigate potential effects of silicate sublimation directly from the surface of the comet's nucleus, we followed the procedure described in Sec. 6.6.3 for atomic sodium and employed the dependence of the saturated vapor pressure on temperature for forsterite,[17] the magnesium-rich end-member of the olivine solid solution series (Mg_2SiO_4), measured by Hashimoto (1990). For $g_{\rm for}(r)$, the same $g(r;r_0)$ type of empirical law, we derived the constants as follows:

$$\begin{aligned} r_0 &= 0.01486 \text{ AU}, \\ m &= 2.634, \\ n &= 5.155, \\ k &= 3.320, \\ \alpha_0 &= 1.2591 \times 10^{36}. \end{aligned} \tag{77}$$

Ten values of the forsterite sublimation rate between 0.0055 AU and 0.03 AU were fitted with a mean residual of ±2.5 percent.

Application of this law to the observations from 2013 October 31 to November 28, produced no positive results. A solution that included only A_1 failed to converge, and solutions that also included A_2 and A_3 crashed. Given the value of r_0 in Eqs. (77), which is equivalent to about 3.2 $R_\odot$, and the heliocentric distance of the measured image closest to the Sun (Table 14), which exceeds 8 $R_\odot$, any forsterite-sublimation based solution forces a variation in the nongravitational acceleration close to r^{-20}, utterly incompatible with any realistic fit.

6.6.5. *Nongravitational solutions accounting for nucleus' dwindling dimensions near the Sun (DDs)*

In Sec. 6.4 we concluded that this type of nongravitational law offered competitive, but not superior, nongravitational solutions over extended periods of time, when the observations close to perihelion were not included.

We now tested this law, $\mathcal{G}(r;r_\star,\xi)$, on the same data set that was so satisfactorily fitted by the modified nongravitational law and the sodium-sublimation based law. Table 15 shows that the incorporation of the dwindling-dimensions effect (DDs) offers equivalent solutions.

We first applied the approach, described extensively in Sec. 6.4, that allowed us to optimize, successively, both $r_\star$ and ξ. This procedure led for the DDs I$_1$ run (A_1 only) to $r_\star = 0.003 \pm 0.010$ AU and $\xi = 3.90 \pm 0.10$. We noted that the optimized value of $r_\star$, though nominally inside the Sun, was only about 2σ away from the heliocentric distance of 0.024 AU, a point of termination of all activity, which already was substituted for $r_\star$ in Sec. 6.4 and which now defined the solution that is referred to as DDs II in Table 15. We then ran the three options with an individually optimized erosion-rate exponent ξ.

The distributions of residuals from all DDs II runs were nearly identical to the distribution in Figure 25. The

[17] The relationship between the vapor pressure and temperature is followed closely also above 2163 K, the melting point of forsterite.

Table 16
Orbital Elements of Comet C/2012 S1 for the Period of 2013 October 31–November 28 (Solutions MNs I_1, NAs I_1, and DDs II_1).

Orbital parameter/element	Solution MNs I_1	Solution NAs I_1	Solution DDs II_1
Epoch of osculation (TT)	2013 Nov 24.0	2013 Nov 24.0	2013 Nov 24.0
Time of perihelion, t_π (TT)	2013 Nov 28.77687 ± 0.00008	2013 Nov 28.77570 ± 0.00008	2013 Nov 28.77633 ± 0.00008
Argument of perihelion, ω	345°.5501 ± 0°.0010	345°.5402 ± 0°.0010	345°.5430 ± 0°.0010
Longitude of ascending node, Ω	295°.6684 ± 0°.0010	295°.6724 ± 0°.0009	295°.6785 ± 0°.0009
Orbital inclination, i	62°.3300 ± 0°.0032	62°.3144 ± 0°.0030	62°.3231 ± 0°.0032
Perihelion distance, q (AU)	0.0124714 ± 0.0000012	0.0124769 ± 0.0000012	0.0124781 ± 0.0000012
Orbital eccentricity, e	0.9999886 ± 0.0000018	1.0000327 ± 0.0000018	1.0000070 ± 0.0000017
Nongravitational law and parameters:			
Type of law	$g(r; r_0)$	$g_{\rm Na}(r)$	$\mathcal{G}(r; r_\star, \xi)$
Distance r_0 or $r_\star$ (AU)	0.438 ± 0.024	...	0.024; fixed
Mass erosion rate exponent ξ	...	...	3.86 ± 0.11
Radial component A_1 (10^{-15} AU day^{-2}) [a]	+4.61 ± 0.15	+17.75 ± 0.56	+4.56 ± 0.15

[a] Except for the solution DDs II_1, for which the unit is 10^{-8} AU day^{-2}.

only readily detectable differences were in the residuals from the very last STEREO-B observation, on November 28.4968 UT (Table 14), which, from the DDs II_1 run, amounted to −24 arcsec in right ascension and +25 arcsec in declination. Since this measurement was admittedly uncertain because of the elongation of the comet's image (Sec. 6.5), these large residuals (but still smaller than a pixel size), are inconsequential.

Nevertheless, we found consistently that the effect of dwindling dimensions of the nucleus did not play a major role in fitting the astrometric data, even though the law based on it offered a match that was competitive with those by some of the other employed laws and superior to the standard nongravitational law (the SN and SNs runs). It is possible that better results could be achieved with more complex expressions for the DD law, but such options cannot be exercised without first modifying the respective function in the orbit-determination software, such as the EXORB code.

Since we judge the three nongravitational laws about equally successful in fitting the astrometric data in the period of 2013 October 31–November 28, we present in Table 16 the sets of orbital elements from each of the solutions MNs I_1, NAs I_1, and DDs II_1. The sets differ from one another much more than a few times the formal mean errors due to the fact that the influence of the different nature of the nongravitational laws affecting the orbital elements is not included in the formal errors.

6.7. *Implications for C/2012 S1 from Results of Orbital Analysis*

The motion of C/2012 S1 was too complex to fit with a single, all-inclusive orbital solution. We found that the entire arc of the observed orbit could be divided into three parts:

(1) From the first observation at 9.4 AU down to 4.9 AU, that is, from 790 days to about 300 days before perihelion, the comet's motion was satisfactorily fitted by a gravitational solution, which implied an original barycentric reciprocal semimajor axis, $(1/a_{\rm b})_{\rm orig}$, equal to $+0.000\,035 \pm 0.000\,006$ AU^{-1}, equivalent to an initial aphelion distance of $57\,000 \pm 10\,000$ AU and an orbital period of 4.8 ± 1.2 million years, thus confirming that the comet arrived from the Oort Cloud.

(2) Between ∼300 days and ∼30 days before perihelion, at a range of heliocentric distances from ∼4.9 AU down to ∼1 AU, the comet's motion was subjected to a nongravitational acceleration, due to the momentum transferred primarily, but perhaps not solely, from outgassing of water; the best orbital solution was achieved by a modified nongravitational law with a scaling distance of $r_0 \simeq 2$ AU, fairly close to that of the standard law in the Style II formalism of Marsden et al. (1973).

(3) At heliocentric distances smaller than 1 AU, within ∼30 days of perihelion, the comet was moving in an orbit affected by strong nongravitational forces; the scaling distance of the modified law dropped dramatically to about 0.44 AU, suggesting that sublimation of sodium, rather than water ice, dominated the effect. An acceleration due to the Sun's radiation pressure could possibly have been a contributing factor in a late stage.

The sets of orbital elements that best fit the astrometric observations are presented in Table 10 for the first of the three periods of time, in Table 13 for the second period, and in Table 16 for the third period. This last table contains three orbits, each of which fitted the observations about equally well. We already commented on the differences among the individual elements from the three solutions being much greater than the formal errors. The inherent diversity of the laws in Table 16 manifests itself also in an extrapolated prediction of the true time of perihelion passage, which for a given set of elements is achieved by integrating it to the osculation epoch at perihelion.

For the set of elements from the solution DDs II_1 this integration could not in fact be performed because, by definition, the nongravitational acceleration reached a singularity at $r_\star = 0.024$ AU, 3.5 hours before perihelion. The diverse nature of the other two laws is reflected in a difference of 10.4 minutes between the obtained results: November 28.7829 TT from the MNs I_1 run and November 28.7757 TT from the NAs I_1 run. Since there was no reason to prefer either solution, we adopted their average, which was used throughout this paper when counting times from perihelion passage:

$$\begin{aligned} t_\pi &= 2013\ \text{November}\ 28.7793 \pm 0.0036\ \text{TT} \\ &= \quad 2013/11/28, 18\!:\!42.2 \pm 5.2\ \text{TT}. \end{aligned} \tag{78}$$

Table 17
NONGRAVITATIONAL ACCELERATIONS OF COMET C/2012 S1 COMPUTED FROM ORBITAL SOLUTIONS IN TABLE 16.

Distance from Sun (AU)	Computed nongravitational acceleration (units of Sun's gravitational acceleration)		
	Solution MNs I_1	Solution NAs I_1	Solution DDs II_1
0.04	0.0072	0.0121	0.0876
0.20	0.0052	0.0056	0.0031
0.50	0.000033	0.000005	0.000560

The preponderant component of the nongravitational acceleration in the most satisfactory solutions was the radial component, A_1, which was in all such cases positive, pointing away from the Sun and confirming that the comet's orbital motion was decelerated. This obviously means that the momentum transferred to the nucleus was from the material sublimating preferentially in the sunward direction, as expected. The transverse and normal components, A_2 and A_3, were, as a rule, one order of magnitude smaller and their inclusion in the solution usually failed to improve the quality of fit. The runs, in which only A_1 was solved for, were consistently preferred as the most dependable ones.

Because the nucleus disintegrated into pebbles and dust before it reached a heliocentric distance of 5 $R_\odot$, we see no role whatsoever for the Sun's tidal forces. Similarly, we do not see any effect on the orbit from sublimation of silicates, apparently because the distance from the Sun was still too large even at the time of the last astrometric observation. We suggest that thermal stress due to increasing temperature gradients triggering explosions of pressurized water vapor and other volatile species from heated and/or thermally damaged reservoirs in the nucleus' interior was most probably responsible for episodic primary fragmentation of the nucleus that subsequently turned into cascading fragmentation of its debris. Although thermal stresses in the nuclei of sungrazing comets are substantially smaller before perihelion than afterward (Sekanina & Chodas 2012), the cohesion of the nucleus of C/2012 S1 was obviously much too low to withstand them. The integrated effect on the orbital motion by continuous sublimation of sodium atoms (and, in smaller amounts, other materials) was at heliocentric distances of less than 1 AU apparently greater than by episodic outbursts of water molecules.

It is highly enlightening to compute the magnitude of the comet's nongravitational acceleration as a function of heliocentric distance from the three laws in Table 16. For three distances these accelerations (in units of the Sun's gravitational acceleration at the same distance) are listed in Table 17. It is known that for the relatively few one-apparition comets, for which the nongravitational parameters could be determined, the acceleration is usually on the order of 10^{-5}, seldom 10^{-4}, the Sun's gravitational acceleration (Marsden & Williams 2008), as indeed it was for C/2012 S1 at larger heliocentric distances (Tables 12 and 13; about 7×10^{-4} from the solution MN II_1). Nongravitational accelerations on the order of several times 10^{-3} the Sun's gravitational acceleration or higher, seen in Table 17, are unheard of. If, for example, the accelerations in the first row of Table 17 are due to sublimation of sodium atoms, the parent bodies from which they were released had typical dimensions in a centimeter to submeter size range at most, depending in part on the velocities of release (assumed hundreads of meters per second), bulk density (assumed a fraction of 1 g cm^{-3}), and the degree of sublimation anisotropy (assumed on the order of 0.1). This is the same range of dimensions that we estimated from independent evidence in Sec. 4.3. We should add that it is possible that a fraction of the nongravitational acceleration could be due to solar radiation pressure, although probably only a small fraction because centimeter-sized grains are subject to radiation-pressure accelerations not exceeding 10^{-4} the Sun's gravitational acceleration.

7. COMPARISON OF C/2012 S1 WITH KREUTZ SUNGRAZER C/2011 W3 (LOVEJOY).

This last section before the conclusions is dedicated to comparison, especially in close proximity to the Sun, of the physical behavior of C/2012 S1 with that of the most recent bright Kreutz sungrazer, C/2011 W3. To a considerable extent, the traits of either object are related to the different perihelion distances and to the very different origin (Oort Cloud vs Kreutz system). We address this issue because the two comets have sometimes been judged to possess similar properties. We limit our comparison primarily to images in the C2 and C3 coronagraphs on board SOHO, but similar studies can also be based on other instruments. We find major differences between the two objects, as follows:

(i) *Saturation of the coronagraphs' CCD detectors before perihelion*. The head of C/2012 S1 stopped saturating the detectors just hours before it disappeared behind the occulting disks of the two instruments; *whereas* the head of C/2011 W3 continued to saturate them until its disappearance.

(ii) *Morphology of the tail in preperihelion images*. The tail of C/2012 S1 was in these images bifurcated, consisting of a main feature and a streamer extending along the orbit; *whereas* the narrow preperihelion tail of C/2011 W3 showed no such morphology.

(iii) *Origin of the preperihelion tail*. The ejecta in the two components of the preperihelion tail of C/2012 S1 were very different in origin, released at vastly different heliocentric distances; *whereas* the ejecta in the preperihelion tail of C/2011 W3 were of uniform origin.

(iv) *Dynamical nature of the preperihelion tail in postperihelion images*. The preperihelion tail of C/2012 S1 in these images was invariably dominated by the ejecta released during an event around 6 days before perihelion and was closely approximated by a *synchrone* fitting this event; *whereas* the preperihelion tail of C/2011 W3 consisted of a stream of continuously emitted submicron-sized particles, described by a *syndyname*.

(v) *Survival of preperihelion particulate ejecta*. Some of the dust ejected from C/2012 S1 along the inbound branch of the orbit survived perihelion passage; *whereas* none of the solid material released from C/2011 W3 before perihelion was observed to survive.

(vi) *Nucleus condensation in the comet's head after its reappearance from behind the occulting disk*. C/2012 S1 displayed *no nuclear condensation* in the images; *whereas* C/2011 W3 was starlike, saturating the detectors.

(vii) *Orientation and outlines of the tail extension near the head in post-perihelion images*. The head of C/2012 S1 exhibited a fan-shaped feature pointing sideways of the Sun and no extension whatsoever in the antisolar direction; *whereas* the head of C/2011 W3 was first tailless, but soon was developing a new tail that rapidly grew in length and was directed approximately away from the Sun; later, a second, narrow tail began to show up exactly along the prolonged radius vector.

(viii) *Activity pattern in the light curve*. Between 9.4 and 0.7 AU from the Sun, the light curve of C/2012 S1 showed its preperihelion activity to have evolved in five progressively contracting cycles; *whereas* the light curve of C/2011 W3 displayed no such pattern; however, this object was under observation for only a very limited period of time before perihelion.

(ix) *Preperihelion vs post-perihelion brightness variations*. C/2012 S1 was intrinsically bright long before perihelion; on the average, it was brightening at a very slow rate upon its approach to perihelion, yet appearing vastly brighter shortly before perihelion than its debris afterwards; *whereas* C/2011 W3 was first extremely faint with a steep pace of brightening before perihelion; it reached its peak brightness shortly after perihelion.

(x) *Nucleus' disintegration*. The nuclei of both comets fell apart and dissipated, but the demise of the nucleus of C/2012 S1 occurred shortly before perihelion; *whereas* the collapse of C/2011 W3 took place after perihelion.

Most of these differences are due to a major distinction between the two objects in material strength, with the nucleus of C/2012 S1 being much less cohesive than that of C/2011 W3. We notice no obvious similarities between the two objects in physical behavior beyond the basic features of cometary appearance and activity.

8. CONCLUSIONS

The present investigation of comet C/2012 S1 offers a comprehensive analysis of its light curve, water production curve, morphology of the head and tail, and orbital motion, with the aim to learn about the comet's evolution and physical behavior in general, and about the developments that led to the comet's preperihelion disintegration in particular. Although emphasis is on features and events at small heliocentric distances, some information is acquired on the comet's activity far from the Sun as well. The results allow us to arrive at the following conclusions:

(1) The comet's intrinsic brightness appears to have been evolving in cycles, five of which, A–E, took place between the heliocentric distances of 9.4 AU and 0.7 AU, each consisting of an expansion stage and a depletion stage. The expansion stage began with an ignition (or activation) point and ended with a stagnation point, while the depletion stage began with the stagnation point and ended at the ignition point of the next cycle.

(2) The duration of the cycles grew progressively shorter with decreasing distance r from the Sun, from >290 days for the cycle A to 15 days for E. Their extent was much less uneven in terms of $\log r$. The cycles were probably caused by activation of limited, discrete reservoirs of ices on and just beneath the nucleus' surface.

(3) At heliocentric distances smaller than about 2 AU, the available water production curve and the light curve correlated in a qualitative sense, the correlation being especially high in November; the peaks on the two curves either coincided or the light curve trailed Combi et al.'s curve of daily averages of the water production rate.

(4) Extrapolation of the daily averages of the water production rate and the $Af\rho$ data on dust production suggests that between 2013 October 1 and November 25 the comet's loss of mass amounted to nearly 6×10^{13} grams, equivalent to a sphere 0.65 km in diameter at an assumed bulk density of 0.4 g cm^{-3}. Given that the nucleus disintegrated completely before reaching perihelion, this was its diameter at the time of close approach to Mars on 2013 October 1; it is consistent with the result based on the HiRISE photometric measurements, according to which the nucleus was not more than 1 km across.

(5) Examination of the contamination of the HiRISE photometry of the nucleus by dust ejecta leads to a conclusion that the cross-sectional area of the nucleus accounted for less than 50 percent of the signal in the brightest pixel of the comet's image.

(6) The cycle E terminated 16 days before perihelion, at the onset of a precursor to the first major outburst called Event 1. A drop in the intrinsic brightness, which followed, stabilized after a few days, and a little more than 9 days before perihelion a new flare-up occurred, a precursor to Event 2. Although not exceeding Event 1 in peak intrinsic brightness, Event 2 displayed multiple maxima, lasted for at least 3 days, and followed an enormous temporary increase in the production of water.

(7) During Events 1 and 2, the sublimating area needed to explain the water production rate exceeded — in the case of Event 2 steadily over a period of several days — the surface area of the nucleus' sunlit hemisphere by a factor of, respectively, ∼20 and ∼40. Both the persistence of, and erratic changes in, the greatly elevated water production rule out an effect of icy grains as a source and, instead, imply fragmentation of the nucleus — due probably to rapidly increasing thermal stress in its interior.

(8) Events 1 and 2 differ from each other in that most of the comet's water ice supplies were retained, presumably in the largest fragments comparable in size to the initial nucleus, in Event 1, whereas the ice retention was close to nil in Event 2, indicating that the nucleus was then shattered into much smaller fragments than before. The activity of all fragments ceased before perihelion.

(9) A preliminary report of a major drop in gas emission (by a factor of 20 or more) 3 days before perihelion confirms that by then the supplies of ice in what remained of the comet's nucleus were practically exhausted.

(10) As a result of continuing cascading fragmentation, all boulders dated from Events 1 and 2 grew progressively smaller with time, and extensive crumbling of particulates may in part account for a steep intrinsic brightening in the course of Event 3, which began some 2.4 days before perihelion, about 40 $R_\odot$ from the Sun, and peaked ∼16 hours before perihelion. The other, probably dominant, contribution to the brightness was due to sublimation of sodium from the fragmented comet, which, as it was approaching the Sun, increasingly resembled a cloud of dust, much of it microscopic.

(11) At the time of maximum light, some 16 hours before perihelion, the comet's apparent visual magnitude

of −2 was first thought to be the onset of the long-anticipated high level of activity. The misleading nature of this development is illustrated on an elementary case that the same brightness is achieved, without any contribution from sublimating sodium, by a cloud of less than 10^{12} g of dust particles, each 0.5 micron in diameter and of moderate bulk density.

(12) A major part of our investigation was devoted to a study of the comet's evolution over a period of 33 hours, based on eight preperihelion and post-perihelion images taken with the coronagraphs on board the SOHO and STEREO-A and B spacecraft; our objectives were to fully exploit the powerful stereoscopic capability provided by the spatial configuration of the spacecraft for examining the comet's principal morphological features.

(13) Modeling of the preperihelion images showed that the dominant contributor to a prominent, slightly curved tail, seen in the SOHO and STEREO images alike, was the microscopic dust that was released during Event 2, centered on 6 days before perihelion; an unresolved contribution from Event 1 was probably detected in one of the three studied preperihelion images.

(14) In the last modeled preperihelion image, the tail made of the Event 2 dust ejecta displayed a deformation emanating from the head in the form of a short "beard." Its leading boundary fitted the release of microscopic dust some 15 hours before perihelion, closely correlating with the sharp peak on the intrinsic-brightness curve.

(15) The disappearance of the comet's head over a period of 4 hours, from about 5 hours before perihelion on, has been recorded in real time in images taken with the C2 coronagraph on board SOHO. The images show a pointed extension protruding from an originally rounded head in the direction of motion, and a truncated leading boundary of the tail. The forward tip of the extension was the site of the most massive fragments of the disintegrating nucleus. The tail's truncated boundary was another sign of the termination of Event 3 and was related to the "beard" detected in a set of images taken shortly before perihelion from on board STEREO-A.

(16) The post-perihelion appearance of C/2012 S1 differed from that before perihelion and resembled a winged object. A narrow tail, trailing far behind, was also visible in most images, representing an essentially detached feature on the other side of the Sun from the location of the wings. The tail was again dominated by the dust ejecta from Event 2, as was one of the wings, which could also be described as a trailing boundary of a dust emission fan. Although some post-perihelion images, especially those taken with the C3 coronagraph, displayed a pseudo-condensation at the point where the wings joined together, none of these images showed a true *nuclear* condensation. The object remained headless and the local brightening was a result of forward scattering of sunlight by porous dust at phase angles of almost 130°.

(17) The leading boundary of the dust emission fan in several images taken with the coronagraphs on board all three spacecraft after perihelion was positively identified by modeling as containing the final dust ejecta ever released from the comet and led to the conclusions that 3.5 ± 0.3 hours before perihelion, at 5.2 $R_\odot$ from the Sun, (i) all activity terminated, never again to be resuscitated; (ii) the nucleus' disintegration was completed; and, as a result, (iii) C/2012 S1 ceased to exist.

(18) Our modeling of Combi et al.'s daily averages of the water production rate suggests that, before fragmentation, the nucleus was in fact very active given its small size, and that some water ice was apparently sublimating from icy-dust grains in the comet's atmosphere. We further find that the conclusions based on our examination of the comet's morphology are consistent with the water production history

(19) Submicron-sized dust particles were present in the Event 2 tail and were detected in preperihelion as well as post-perihelion images. These particles moved in strongly hyperbolic orbits very different from the orbit of the comet (and its sizable fragments), some with much larger perihelion distances and passing perihelion only weeks after the largest debris. Many particles survived, as their orbits shielded them from the most hostile environment near the Sun.

(20) By contrast, we find no submicron-sized grains along the leading boundary of the emission fan, which is interpreted to mean that they were absent from the final dust release around 3.5 hours before perihelion.

(21) A separate category is solid material that populated the comet's streamer, clearly apparent in many preperihelion C2 and C3 images and in several post-perihelion C2 images; these include two of the modeled images. The streamer followed closely the projected orbit behind the comet, consisted of very large pieces of dust released from the nucleus at considerable heliocentric distances, and was of a similar nature as dust trails of periodic comets. From the streamer's orientation and the curvature the actual time (or distance) of release cannot be determined.

(22) An important property of the streamer was its disconnection from the head, suggesting dust sublimation at a nearly constant distance from the Sun, but different in images taken before and after perihelion. Accounting for this effect in terms of a self-consistent model shows that if the sublimation heat of the streamer's material was constant, pebble-sized gravel should have been released at heliocentric distances up to ∼100 AU, presumably by the annealing of amorphous water ice (at temperatures as low as 37 K) and millimeter-sized grains should have been released in large quantities at about 10 AU from the Sun during the heights of the crystallization of amorphous ice into cubic ice (at temperatures close to 130 K), with the heat of sublimation near 90 000 cal mol^{-1}. No part of the streamer survived perihelion passage.

(23) The brightness of the dissipating cloud of solid debris was rapidly diminishing with time after perihelion. A total cross-sectional area of dust in the fan-shaped cloud amounted to not more than 50 000 km^2 in a 27-arcmin aperture, used by Nakano to derive the magnitude from a C3 image taken on November 29.38 UT, 0.6 day post-perihelion. From a model that employs this cross-sectional area and includes assumptions about a size-distribution law of the debris, we estimate that the largest surviving *inert* fragments of the nucleus were almost certainly smaller than ∼0.25 meter and may even have been sub-centimeter in diameter. It follows from conclusion (8) that no *active* fragments survived.

(24) Comprehensive orbital analysis of the comet shows that its motion could successfully be fitted by a gravitational solution only at heliocentric distances greater than 4.9 AU. The solution confirms that the object originated

in the Oort Cloud and began its journey to perihelion at some 50 000 to 60 000 AU from the Sun.

(25) Between 4.9 AU and 1 AU from the Sun, the comet's orbital motion was affected by a nongravitational acceleration driven by the momentum transferred from the sublimating species, primarily but probably not exclusively water ice. A satisfactory match to astrometric observations in this range of heliocentric distances was achieved with a nongravitational law similar to the standard law used in the Style II formalism of Marsden et al. (1973), but with a somewhat smaller scaling distance.

(26) At distances from the Sun smaller than 1 AU, the motion of the comet was subjected to major nongravitational forces, whose variations with time could not be fitted by the standard law of water production; one of three nongravitational laws that did match the observed perturbations was based on the sublimation of sodium. The nongravitational accelerations near the Sun were as high as 10^{-2} the Sun's gravitational acceleration and could represent an effect due to sodium sublimation from the nucleus' debris in a centimeter to submeter size range; a minor contribution from the Sun's radiation pressure could not be ruled out.

(27) The radial component, which dominated the nongravitational acceleration, was always directed away from the Sun, indicating that the comet's orbital motion was systematically decelerated, obviously because of the prevailing sunward direction of the flow of sublimating material from the disintegrating nucleus.

(28) Comparison of C/2012 S1 with the recent bright Kreutz sungrazer C/2011 W3 revealed major differences between the two objects; the nucleus of the latter held together much more strongly.

(29) We found no contribution from the Sun's tidal forces to the disintegration of C/2012 S1 and detected no evidence for sublimation of silicates from the nucleus, apparently because even the last astrometric observation was still made much too far from perihelion.

We thank M.-T. Hui, Guangzhou, China, for sending us an extended version of the curve of apparent-brightness variations of comet C/2012 S1 he derived from HI1-A images. We also thank A. Vitagliano, Universitá di Napoli 'Federico II', for his positive response to our request for modifications of his orbit determination code. This research was carried out in part at the Jet Propulsion Laboratory, California Institute of Technology, under contract with the National Aeronautics and Space Administration.

REFERENCES

Agúndez, M., Biver, N., Santos-Sanz, P., et al. 2014, A&A, 564, L2
A'Hearn, M. F., Millis, R. L., Schleicher, D. G., et al. 1995, Icarus, 118, 223
Ayotte, P., Smith, R. S., Stevenson, K. P., et al. 2001, JGR, 106, 33387
Bar-Nun, A., Herman, G., Laufer, D., & Rappaport, M. L. 1985, Icarus, 63, 317
Bar-Nun, A., Dror, J., Kochavi, E., & Laufer, D. 1987, Phys. Rev. B, 35, 2427
Biver, N., Agundez, M., Santos-Sanz, P., et al. 2013, CBET 3711
Bodewits, D., Farnham, T., & A'Hearn, M. F. 2013, CBET 3718
Boehnhardt, H. 2004, in Comets II, ed. M. C. Festou, H. U. Keller, & H. A. Weaver (Tucson, AZ: Univ. Arizona Press), 301
Boehnhardt, H., Tubiana, C., Oklay, N., et al. 2013, CBET 3715
Boehnhardt, H., Vincent, J. B., Chifu, C., et al. 2013, CBET 3731
Bonev, B. P., DiSanti, M. A., Gibb, E. L., et al. 2013, CBET 3720
Brueckner, G. E., Howard, R. A., Koomen, M. J., et al. 1995, Sol. Phys., 162, 357
Chamberlain, J. W. 1960, ApJ, 131, 47
Chamberlain, J. W. 1961, ApJ, 133, 675
Combi, M. R., Bertaux, J.-L., Quemerais, E., et al. 2013, IAUC 9266
Combi, M. R., Fougere, N., Mäkinen, J. T. T., et al. 2014, ApJ, 788, L7 (5pp)
Coulson, I. M., Milam, S. N., Villanueva, G. L., et al. 2013, CBET 3693
Crovisier, J., Colom, P., Biver, N., & Bockelée-Morvan, D. 2013, CBET 3711
Curdt, W., Boehnhardt, H., Vincent, J.-B., et al. 2014, A&A, 567, L1
Delamere, W. A., McEwen, A. S., Mattson, S., et al. 2013, CBET 3720
Dello Ruso, N., Vervack, Jr., R. J., Kawakita, H., et al. 2013, CBET 3686
Delsemme, A. H., & Miller, D. C. 1971, Planet. Space Sci, 19, 1229
Dohnanyi, J. S. 1969, JGR, 74, 2531
Enzian, A., Cabot, H., & Klinger, J. 1998, Planet. Space Sci., 46, 851
Ferrín, I. 2013, eprint arXiv:1310.0552
Ferrín, I. 2014, Planet. Space Sci., 96, 114
Fitzsimmons, A., Lacerda, P., Lowry, S., et al. 2013, IAUC 9261
Fulle, M. 1999, Adv. Space Res., 24 (9), 1087
Golubev, A. V., Bryukhanov, I. S., Tabolich, A., et al. 2014, Astron. Tsirk. 1611
González, M., Gutiérrez, P. J., Lara, L. M., & Rodrigo, R. 2008, A&A, 486, 331
Hashimoto, A. 1990, Nature 347, 53
Herman, G., & Podolak, M. 1985, Icarus, 61, 252
Hines, D. C., Videen, G., Zubko, E., et al. 2013, ApJ, 780L, 32
Howard, R. A., Moses, J. D., Vourlidas, A., et al. 2008, Space Sci. Rev., 136, 67
Huebner, W. F., Keady, J. J., & Lyon, S. P. 1992, Astrophys. Space Sci., 195, 1
Jenniskens, P., & Blake, D. F. 1994, Science, 265, 753
Jenniskens, P., & Blake, D. F. 1996, Planet. Space Sci., 44, 711
Keane, J. V., Meech, K. J., Mumma, M. J., et al. 2013, IAUC 9261
Klinger, J. 1980, Science, 209, 271
Knight, M. M., & Battams, K. 2014, ApJ, 782L, 37
Knight, M. M., & Walsh, K. J. 2013, ApJ, 776, L5
Korsun, P. P., & Chörny, G. F. 2003, A&A, 410, 1029
Laufer, D., Kochavi, E., & Bar-Nun, A. 1987, Phys. Rev. B, 36, 9219
Laufer, D., Pat-El, I., & Bar-Nun, A. 2005, Icarus, 178, 248
Li, J.-Y., Weaver, H. A., Kelley, M. S., et al. 2013, CBET 3496
Li, J.-Y., Kelley, M. S., Knight, M. M., et al. 2014, Am. Astron. Soc., AAS Meeting #223, #218.06
Marcus, J. N. 2007, Int. Comet Quart., 29, 39
Marsden, B. G., & Williams. G. V. 2008, Catalogue of Cometary Orbits 2008 (17th ed.; Cambridge, MA: Smithsonian Astrophysical Observatory), 195 pp
Marsden, B. G., Sekanina, Z., & Yeomans, D. K. 1973, AJ, 78, 211
Marsden, B. G., Sekanina, Z., & Everhart, E. 1978, AJ, 83, 64
McDonnell, J. A. M., Alexander, W. M., Burton, W. M., et al. 1987, in Exploration of Halley's Comet, ESA SP-250, ed. M. Grewing, F. Praderie, & R. Reinhard (Berlin: Springer-Verlag), 719
Meech, K. J., Pittichová, J., Bar-Nun, A., et al. 2009, Icarus, 201, 719
Meech, K., Keane, J., Yang, B., et al. 2013a, CBET 3693
Meech, K. J., Yang, B, Kleyna, J., et al. 2013b, ApJ, 776, 20
Mumma, M. J., DiSanti, M. A., Paganini. L., et al. 2013b, IAUC 9263
Nakano, S. 2013a, CBET 3731
Nakano, S. 2013b, CBET 3767
Nakano, S. 2013c, Nakano Note 2587
Nevski, V., & Novichonok, A. 2012, CBET 3238
Opitom, C., Jehin, E., Manfroid, J., et al. 2013a, CBET 3693
Opitom, C., Jehin, E., Manfroid, J., et al. 2013b, CBET 3711
Opitom, C., Jehin, E., Manfroid, J., & Gillon, M. 2013c, CBET 3719
Paganini, L., Blake, G. A., Villanueva, G. L., et al. 2013, IAUC 9263
Patashnick, H., Rupprecht, G., & Schuerman, D. W. 1974, Nature, 250, 313

Prialnik, D. 1992, ApJ, 388, 196
Prialnik, D. 2006, in Asteroids, Comets, Meteors, Proc. 229th IAU Symp., ed. L. Daniela, M. Sylvio Ferraz, & F. J. Angel (Cambridge, UK: Cambridge Univ. Press), 153
Reach, W. T., Sykes, M. V., Lien, D., & Davies, J. K. 2000, Icarus, 148, 80
Remijan, A. J., Gicquel, A., Milam, S. N., et al. 2013, CBET 3693
Rickman, H., Kamél, L., Froeschlé, C., & Festou, M. C. 1991, AJ, 102, 1446
Schleicher, D. 2013a, IAUC 9260
Schleicher, D. 2013b, IAUC 9254
Schmitt, B., & Klinger, J. 1987, in Diversity and Similarity of Comets, ESA SP-278, ed. E. J. Rolfe & B. Battrick (Noordwijk, Netherlands: ESTEC), 613
Schmitt, B., Espinasse, S., Grim, R. J. A., et al. 1989, in Physics and Mechanics of Cometary Materials, ESA SP-302, ed. J. Hunt & T. D. Guyenne (Noordwijk, Netherlands: ESTEC), 65
Sekanina, Z. 1975, Icarus, 25, 218
Sekanina, Z. 1981, AJ, 86, 1741
Sekanina, Z. 1988, AJ, 95, 911
Sekanina, Z. 1992, in Asteroids, Comets, Meteors 1991, ed. A. W. Harris & E. Bowell (Houston, TX: Lunar Planet. Inst.), 545
Sekanina, Z. 1993, AJ, 105, 702
Sekanina, Z. 2013a, eprint arXiv:1310.1980
Sekanina, Z. 2013b, CBET 3731
Sekanina, Z. 2013c, CBET 3723
Sekanina, Z., & Chodas, P. W. 2012, ApJ, 757, 127
Sekanina, Z., Hanner, M. S., Jessberger, E. K., & Fomenkova, M. N. 2001, in Interplanetary Dust, ed. E. Grün, B. Å. S. Gustafson, S. F. Dermott, & H. Fechtig (Heidelberg: Springer), 95
Sekhar, A., & Asher, D. J. 2014, MNRAS, 437, L71
Sitko, M. L., Russell, R. W., Kim, D. L., et al. 2013, IAUC 9264
Smoluchowski, R. 1981, ApJ, 244, 31
Sykes, M. V., & Walker, R. G. 1992, Icarus, 95, 180
Sykes, M. V., Lebofsky, L. A., Hunten, D. M., & Low, F. 1986, Science, 232, 1115
van de Hulst, H. C. 1957, Light Scattering by Small Particles. (New York: Wiley & Sons, 470pp)
Weaver, H. A., Sekanina, Z., Toth, I., et al. 2001, Science, 292, 1329
Weaver, H., Feldman, P., McCandliss, S., et al. 2013, CBET 3680
Williams, G. V. 2013a, MPEC 2013-W13
Williams, G. V. 2013b, MPEC 2013-W16
Williams, G. V. 2013c, MPC 86228
Williams, G. V. 2014, MPC 87064
Ye, Q., Hui, M.-T., & Gao, X. 2013, CBET 3718
Yeomans, D. K., Chodas, P. W., Sitarski, G., et al. 2004, in Comets II, ed. M. C. Festou, H. U. Keller, & H. A. Weaver (Tucson, AZ: Univ. Arizona Press), 137